Max-Planck-Institut
für Meteorologie

MAX-PLANCK-GESELLSCHAFT

International Max Planck Research School
on Earth System Modelling

Climate and Air Pollution Modelling in South America with Focus on Megacities

Claas Teichmann

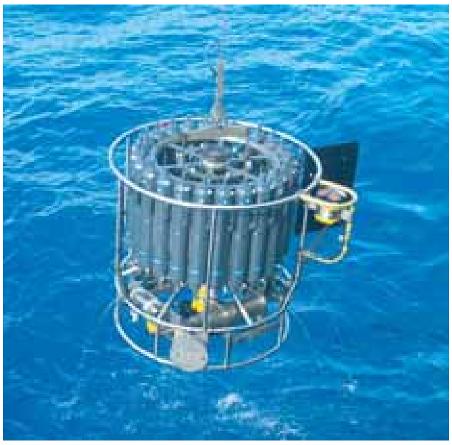

Berichte zur Erdsystemforschung 76/2010

Reports on Earth System Science

Hinweis

Die Berichte zur Erdsystemforschung werden vom Max-Planck-Institut für Meteorologie in Hamburg in unregelmäßiger Abfolge herausgegeben.

Sie enthalten wissenschaftliche und technische Beiträge, inklusive Dissertationen.

Die Beiträge geben nicht notwendigerweise die Auffassung des Instituts wieder.

Die "Berichte zur Erdsystemforschung" führen die vorherigen Reihen "Reports" und "Examensarbeiten" weiter.

Notice

The Reports on Earth System Science are published by the Max Planck Institute for Meteorology in Hamburg. They appear in irregular intervals.

They contain scientific and technical contributions, including Ph. D. theses.

The Reports do not necessarily reflect the opinion of the Institute.

The "Reports on Earth System Science" continue the former "Reports" and "Examensarbeiten" of the Max Planck Institute.

Anschrift / Address

Max-Planck-Institut für Meteorologie
Bundesstrasse 53
20146 Hamburg
Deutschland

Tel.: +49-(0)40-4 11 73-0
Fax: +49-(0)40-4 11 73-298
Web: www.mpimet.mpg.de

Layout:

Bettina Diallo, PR & Grafik

Titelfotos:
vorne:
Christian Klepp - Jochem Marotzke - Christian Klepp
hinten:
Clotilde Dubois - Christian Klepp - Katsumasa Tanaka

Berichte zur Erdsystemforschung 76/2010

Climate and Air Pollution Modelling in South America with Focus on Megacities

Claas Teichmann

aus Wilhelmshaven

Hamburg 2009

Reports on Earth System Science 76/2010

ISSN 1614-1199

Claas Teichmann
Max-Planck-Institut für Meteorologie
Bundesstrasse 53
20146 Hamburg
Germany

Als Dissertation angenommen
vom Department Geowissenschaften der Universität Hamburg

auf Grund der Gutachten von
Prof. Dr. Guy P. Brasseur
und
Prof. Dr. Daniela Jacob

Hamburg, den 1. Dezember 2009
Prof. Dr. Jürgen Oßenbrügge
Leiter des Departments für Geowissenschaften

ISSN 1614-1199

Climate and Air Pollution Modelling in South America with Focus on Megacities

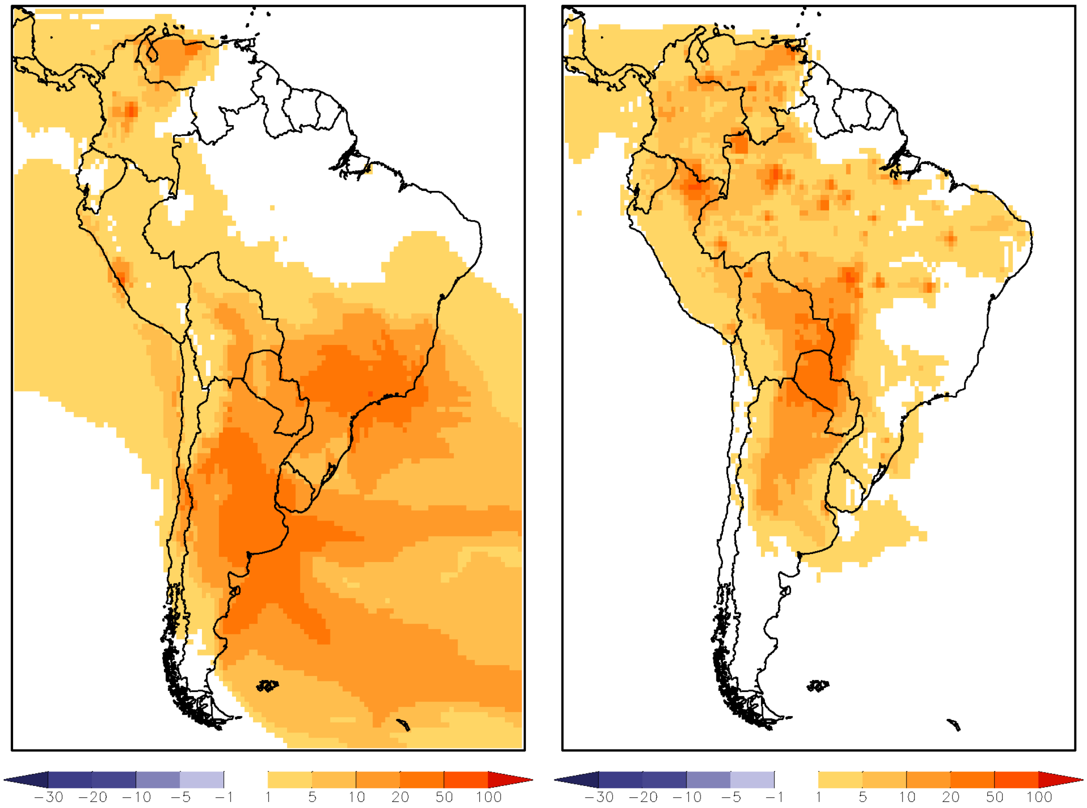

Claas Teichmann

Hamburg 2009

Summary

The two major sources of air pollutants in South America are anthropogenic emissions and biomass burning emissions. Anthropogenic megacity emissions play a special role with respect to air pollution: a relatively large amount of pollutants is released in a small area potentially leading to non-linear chemical processes, which may further aggravate air pollution. Megacities in South America - themselves being highly populated - are mainly located in coastal areas which have a relatively high population density. Wildland fires on the other hand are located in the inner continent, predominantly south of the Amazon basin, in a region with relatively low population density.

In order to compare the impact of these two emission sources in South America on a climatological timescale, a regional climate model is used, which calculates meteorological processes together with chemical processes. The implementation of a chemical mechanism into the latest operational version of the regional climate model REMO (REMO 5.7) is done in the frame of this study. Additionally the vertical convection scheme for trace gases is improved in order to assure realistic trace gas concentrations.

In this study, the chemical state of the atmosphere is simulated for the year 2000. The simulation is embedded in a long term climate run of REMO and includes the main seasons of biomass burning. Simulated tracer concentrations are compared to MOPITT satellite data and to measurements from the INCA field campaign. Modelled spatial patterns of total column CO concentrations agree well with MOPITT data. The model reproduces well vertical profiles of ozone measured during INCA, while it has a slight positive bias in the lower troposphere with respect to CO concentrations, possibly due to an overestimation of emissions in the region.

In the frame of this study, the influence of the two temporally and spatially different emission sources, megacities and biomass burning, on the regional air quality in South America is investigated. While biomass burning exhibits a strong seasonal cycle, megacity emissions are about constant throughout the year. Here, the combined effect of changes in emissions and meteorology are studied for the dry season (biomass burning season) and the wet season. The impact area, i.e., the area in which air pollution levels increase by more than 10 %, stays about constant throughout the year in the case of CO emissions from megacities. For less homogeneously mixed atmospheric trace species like NO_x the impact area shows a peak in southern hemisphere winter. The impact area from biomass burning emissions shows a strong seasonal cycle for ozone, CO and NO_x with peak extent in the biomass burning season. This temporal pattern is predominantly controlled by the emission cycle while changes in the meteorology play a minor role.

In this study the population impact, i.e., the number of people affected by air pollution increases of more than 10 %, due to megacity or biomass burning emissions is investigated. Outside the biomass burning season, the population impact of CO from biomass burning is relatively small (below 10 million inhabitants) compared to the population impact from megacity emissions (about 83 million inhabitants). During the biomass burning season, population impact of CO emissions from biomass burning is about twice as high as population impact of megacity emissions although the latter are 14 times smaller. This can be related to the fact that megacity emissions affect mainly populated coastal areas where biomass burning emission impact is relatively low compared to the inner continent as they are strongly diluted during atmospheric transport.

The population impact of megacity emissions with respect to ozone is relatively small compared to other trace gases. This can be related to the immediate destruction of ozone by NO in the vicinity of the emission sources (the megacities). Ozone is produced again further downwind of the emission source, away from the highly populated areas.

Contents

1 Introduction

1.1 Megacities

Nowadays, more people live in cities than in rural areas (UN, 2008). The ongoing urbanization leads to an increasing number of large population agglomerations. While there existed only two cities with 10 million inhabitants or more in the year 1950 (New York and Tokyo), their number increased to 18 in the year 2000. Projections of the UN show a future increase in the population living in urban areas, which may lead to a further increase in the number of cities with more than 10 million inhabitants. It is estimated that their number will increase to 22 by the year 2015.

In the literature, there exist different thresholds for denoting cities as *megacities*. Common thresholds are five, eight or ten million inhabitants. Within this study, cities with more than five million inhabitants are called megacities. A higher threshold leading to a lower number of considered megacities would also be reasonable, but is not in the frame of this study. The low threshold leads to an upper estimate of megacity impact in South America.

Megacities act as strong pollution sources. Emissions from megacities cause urban air pollution and can also affect air quality in distant areas on a continental scale through long-range transport. A study by Lawrence et al. (2007) indicates that megacities may even have the potential to globally impact air quality. Emissions emanating from megacities are characterized by a high emission density as a large amount of anthropogenic emissions is released in a relatively small area. Because of the non-linear dependency of some chemical processes on the concentrations of the reactants, chemical reactions in areas with high emission density may be very different from those in areas with low emission density.

The controlled growth of a megacity can lead to a rather compact city structure (e.g., London, Paris) whereas an uncontrolled growth causes the city to sprawl (e.g., Los Angeles). The latter type of megacity consumes more energy per inhabitant than the compact megacity. Compact megacities can be typically characterized by high population density, more energy efficiency and a well established public transport.

Additionally, due to their population distribution, inhabitants in compact megacities are less exposed to air pollution than inhabitants of sprawling megacities.

At present, three of the 18 megacities with more than ten million inhabitants mentioned above are located in South America: São Paulo, Buenos Aires and Rio de Janeiro. With the given threshold of five million inhabitants, Lima, Bogotá and Santiago de Chile are also accounted for as megacities. Belo Horizonte and Caracas are also included as megacities in this study – even though their population number is below the threshold. They are included into this work, because they are located at unique locations with respect to air pollution studies: Belo Horizonte is located in the Brazilian highlands away from coastal areas as opposed to nearly all other megacities, which – except for Bogotá – are located near the coast. Caracas is the northernmost megacity of South America located close to the coast in the Caracas valley.

All megacities considered in this study are listed in Table 1.1. Their location can be seen in Figure 1.1. Population data is taken from the Population Division of the Department of Economic and Social Affairs of the United Nations Secretariat[1]. Due to different statistical concepts population data can vary for different sources. The data from the United Nations Secretariat uses the urban agglomeration concept when possible. The concept refers to the population inside a contiguous area inhabited at urban density levels without considering administrative boundaries.

1.2 Climate in South America

Chemical species distributions are closely related to meteorological conditions. Trace species are advected by the atmospheric air flow. Some trace species are wet deposited, which means that elevated precipitation leads to cleaner air via more wet deposition. A reduced precipitation on the other hand leads to less wet deposition which is related to higher trace gas concentrations in the atmosphere. Additionally, the rate of a lot of chemical reactions is temperature dependent. Also cloudiness has an influence on tracer concentrations via the lowering of the solar actinic flux. This decreases the photolysis rates of photochemical reactions. Due to this dependences, the simulation of realistic meteorological conditions is important for the simulation of realistic trace gas concentrations.

---

[1] World Population Prospects: The 2006 Revision and World Urbanization Prospects: The 2007 Revision, http://esa.un.org/unup, Monday, May 05, 2008; 9:43:41 AM.

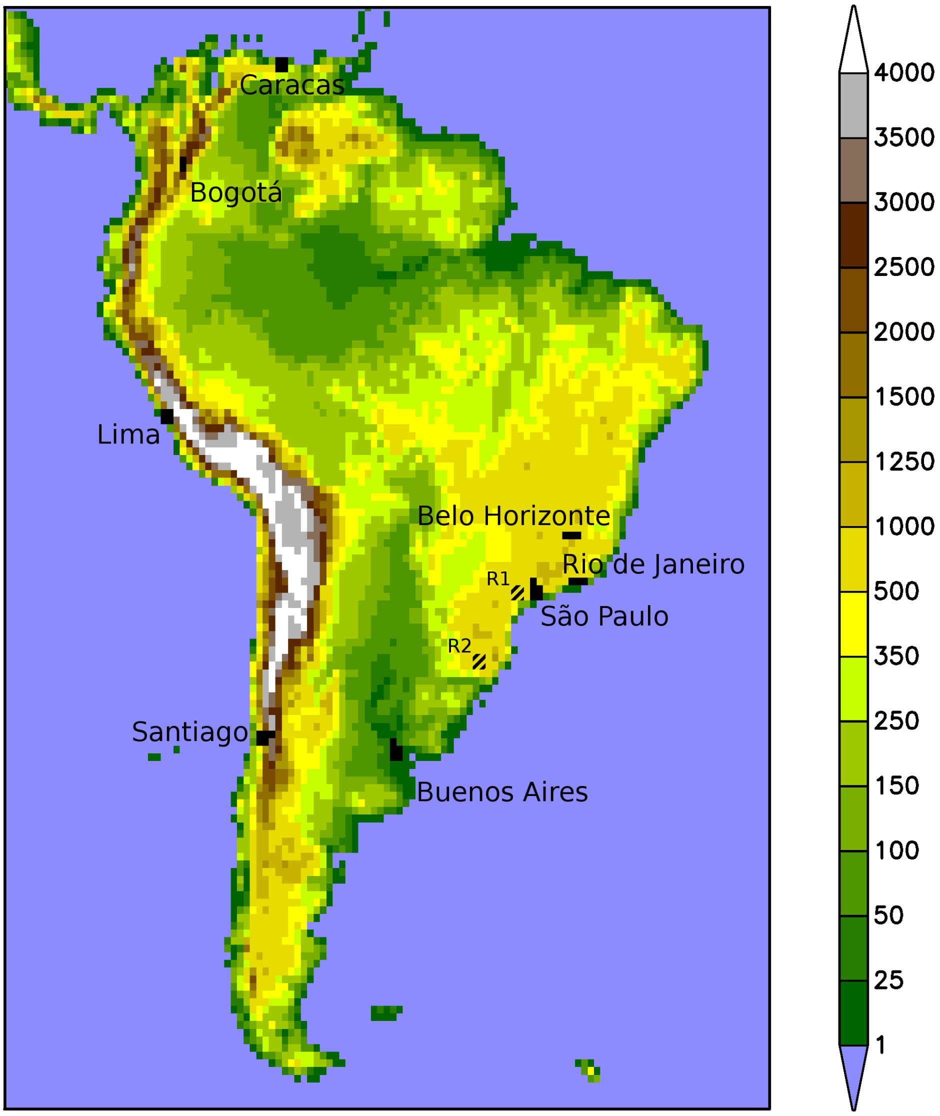

Figure 1.1: Megacities and orography of South America. Megacities listed in Table 1.1 are depicted. The orography of South America as it is represented in this study is shown in [m]. Hatched gridboxes correspond to impact regions, in which the development of tracer concentrations is investigated in detail in Chapter 5. The plot shows the REMO model domain on the rotated grid.

Name	Country	[10^6 inhabitants]	statistical concept	gridboxes
São Paulo	Brazil	17.099	metropolitan area	5
Buenos Aires	Argentina	11.847	urban agglomeration	5
Rio de Janeiro	Brazil	10.803	metropolitan area	3
Lima	Peru	7.116	metropolitan area	4
Bogotá	Colombia	6.356	urban agglomeration	2
Santiago	Chile	5.275	urban agglomeration	5
Belo Horizonte	Brazil	4.659	metropolitan area	3
Caracas	Venezuela	2.864	metropolitan area	4

Table 1.1: Population of megacities in South America. Megacities considered in this study are listed together with their population in the year 2000 and the corresponding statistical concept. The number of gridboxes attributed to each megacity is also shown (cf. Figure 1.1). For details refer to the text.

The two major features in South America influencing the continental climate conditions are the Andes mountain range and the Amazon basin.

The Andes range reach along the western coast from northern Venezuela down to Patagonia in southern Chile (cf. Figure 1.1). With their average height of about 4000 m, which can reach above 6000 m they act as a barrier for low level circulation patterns, which are important for moisture advection and also for the transport of atmospheric pollutants. The Andes mountain range itself can be divided into a relatively wet northern and a southern part with a dry area in the center, extending from central Chile up to northern Peru. This region also includes the Atacama desert, which is the driest desert on earth. Due to their height, yearly mean temperature in the Andes region is relatively low compared to other areas in South America located at the same latitude.

The Amazon basin is located in the northern part of South America, east of the Andes range. Its covers large parts of Brazil, Peru and Bolivia together with Ecuador and Colombia. It is drained by the Amazon river which has most of its sources in the Andes range. The Amazon basin is covered in most parts by the Amazon rainforest. The period between May to November tends to be the dry season in the Amazon region. During this period also the peak in biomass burning emissions in the Amazon can be observed (e.g., Generoso et al., 2003) due to the relatively dry and warm conditions. During a so-called *El Niño* event, the drought in the tropical rain forest of the Amazon can even be intensified. El Niño is associated with a change in the ocean-atmosphere system in the tropical Pacific related to unusual warm ocean surface temperatures.

Temperature and Precipitation Patterns

In general the temperature pattern of South America shows a rather uniform zonal distribution with highest temperatures near the equator and in the tropics and lowest temperatures in the southernmost part of the continent in southern Chile and Patagonia. Especially in the southern part of South America, the zonal structure is present due to the lack of bigger land masses. Nevertheless, some deviations from a perfectly zonal temperature structure exist due to orographic features and ocean currents.

The upwelling cold water related to the Peru current in front of the Peruvian coast cools the atmosphere. Prevailing westerly winds advect the cold air towards the coastal region of Peru and northern Chile leading to a shift of the zonal cold temperature pattern along the coast towards the equator. On the eastern side of the Andes, this shift is not present, as the Andes range hinder a deeper penetration of the cold air into the continent.

On the south-eastern coast of the South American continent, the Brazilian current transports warm water along the coast up to the mouth of the Rio de la Plata, where Buenos Aires is located. Advected air from the ocean towards the coastal areas of Brazil is heated by this warm current leading to a poleward shift of the zonal temperature belts, mainly in southern hemisphere summer. A similar effect is found close to the eastern slopes of the Andes range, where a southward air flow (discussed in more detail in the next section) transports warm air from the Amazon basin towards northern Argentina and the La Plata basin.

Precipitation patterns in South America can be seen as diagonal bands. A broad band of high precipitation stretches from the coast of Colombia in the north-west of the continent towards the southern coast of Brazil, covering the Amazonas basin and the Brazilian highlands. Relatively dry areas are the coast of Venezuela in the northern part of the continent and the north-eastern part of Brazil, the so-called *Nordeste*. An arid belt stretches from the coastal region of Peru and northern and central Chile towards the south-eastern part of Argentina. It is referred to as the *arid diagonal* (e.g., Messerli et al., 1997). Precipitation patterns can be explained by the predominant circulation described in the next section.

Circulation Patterns

Circulation patterns in South America are mainly dominated by the location of the InterTropical Convergence Zone (ITCZ), by the high pressure cells over the south Pacific and the south Atlantic oceans and the prevailing westerlies in the southern part of South America, south of about 40° S (cf. Figure 1.2).

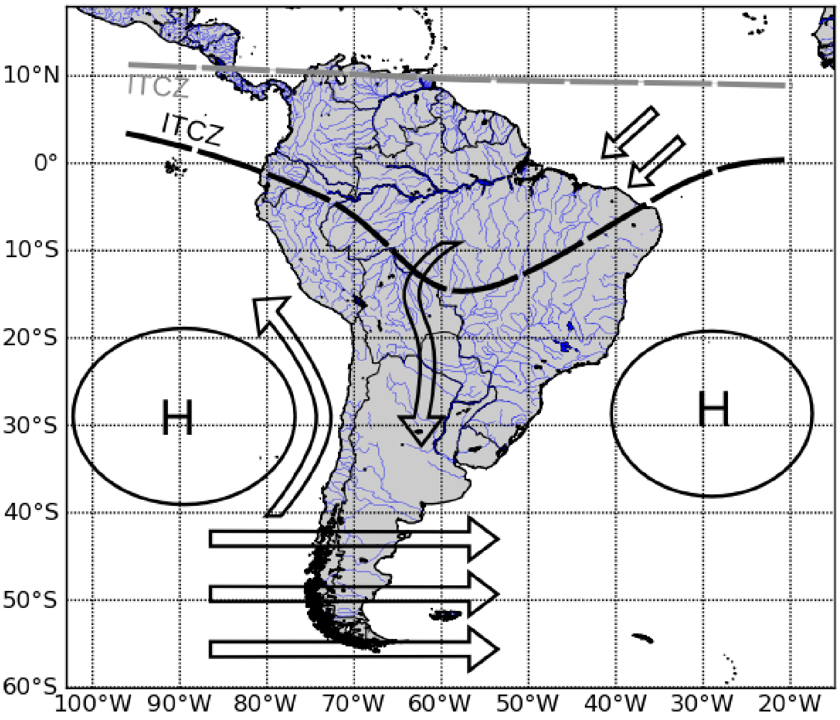

Figure 1.2: Circulation patterns in South America. The main low level circulation patterns in South America are depicted. The location of the ITCZ (black line) corresponds to a typical summer situation, whereas the grey colored ITCZ is typical for a winter episode. For further details refer to the text. (after Hobbs et al., 1998; Vera et al., 2006; Silvestri et al., 2009)

The ITCZ controls the climate in the northern part of the South American continent. It is a convergence band of the trade winds close to the equator. The strong convergence leads to convection, which causes cloudiness and rainfall. As the location of the ITCZ depends on the solar insolation, its movement is related to a distinct annual cycle. The northernmost location of the ITCZ is reached in southern hemisphere winter and corresponds to about the coastline of Venezuela. This location of the ITCZ corresponds to the dry season in the Amazon region. During the southern hemisphere summer - the wet season in the Amazon basin - the ITCZ shifts towards the center of the Amazon basin. During this time period, the Amazon basin receives much of its annual precipitation (cf. Marengo and Hastenrath, 1993).

North of 40° S the zonal westerly flow is disrupted by the Andes range. This contributes to the genesis of the semi-permanent high pressure systems over the south Pacific ocean and over the south Atlantic ocean between about 10° S and 40° S. The south Pacific high pressure system together with the cold Peruvian current, leads to rather low precipitation rates along the west coast of the Andes range between about central Chile and northern Peru. The subsiding air related to the high pressure system prevents formation of rain in these regions.

The high pressure system over the south Atlantic on the other hand leads to transport of air masses (together with moisture) from the Atlantic into the region east of the Andes range. The continuation of the circulation towards the south along the eastern side of the Andes range is called South American low level jet (SALLJ). This low level circulation feature transports air masses together with moisture from the Amazon basin southward towards the La Plata basin located in the center of Argentina (e.g., Virji, 1981; Vera et al., 2006).

South of about 40° S the height of the Andes range decreases mainly to below 1000 m. The fraction of landmasses in the latitudinal band between 40° S and about 60° S is relatively small. This leads to undisturbed prevailing westerlies in the region of Patagonia and southern Chile. They are caused by the temperature gradient between the cold air masses of Antarctica and the relatively warm air masses over the tropical oceans and continents of the southern hemisphere.

1.3 Air Pollution in South America

Atmospheric abundance of many trace gases related to air quality is determined by emissions from the earth's surface. Surface emissions are of anthropogenic or natural origin. Since the industrial revolution around 1850, anthropogenic emissions increased strongly and have an important influence on the concentration of many pollutants and greenhouse gases in the atmosphere (IPCC, 2007). Marcilio and Gouveia (2007), e.g., show that air pollution levels which are currently experienced by the population of some of Brazilian's major urban areas have an important impact on human health. They attributed about 5 % of the annual respiratory mortality of the under five year old children and elderly people to air pollution in these urban areas.

Anthropogenic emissions from fossil fuel combustion and biomass burning from wildland fires are two main sources of pollutants in South America. Schultz et al. (2008b) estimated that the biomass burning in South America accounts for 26.8 % of the direct carbon emitted by biomass burning on a global scale (mean 1960 and 2000). This corresponds to a long-term yearly mean of 548 Tg C/yr. The relatively large difference between estimated minimum (340 Tg C/yr, 1964) and maximum (808 Tg C/yr, 1993) annual carbon emissions in the period 1960 to 2000 shows the high year to year variability of biomass burning emissions in South America. The difficulty in estimating wildland fire emissions can be seen from the large differences of estimated emissions provided in the literature. For the annual mean emissions of carbon monoxide (CO) from open or wildland fires in the year 2000, e.g., the following estimates can be found in the literature for Central and South America: 18 Tg CO/yr (Ito and Penner, 2004), 22 Tg CO/yr (Hoelzemann, 2006), 29 Tg CO/yr (Hoelzemann et al., 2004), 55 Tg CO/yr (Pétron et al., 2004), 70 Tg CO/yr (Schultz et al., 2008b) and 210 Tg CO/yr (Arellano et al., 2004). In this study, the RETRO (REanalysis of the TROpospheric chemical composition over the past 40 years) version 2 database (Schultz et al., 2008a) is used. In the model domain comprising the South American continent (cf. Figure 1.1), about 79.5 Tg CO/yr are emitted by fire emissions in the year 2000.

The other important emission source in South America are anthropogenic emissions. Anthropogenic emissions are, e.g., produced by fossil fuel combustion in industry and road transport. This leads to a total of 25.6 Tg CO/yr emitted by anthropogenic sources. This is about one third of the CO emissions released by wildland fires in the year 2000 in the emission inventory used in this study.

Despite the large difference in the amount of emitted pollutants, the difference in the impact on air quality and human beings is not necessarily greater for biomass burning emissions. Wildland fires are located mainly south of the Amazon region, a long distance away from the main population centers, while most anthropogenic emissions are released close to these locations. Anthropogenic emissions are therefore not subject to dilution in the same magnitude as wildland fire emissions are before affecting air quality in highly populated regions. The location of biomass burning emissions and anthropogenic emissions of CO is shown as an example for the month of October 2000 as they are used in this study in Figure 1.3. A detailed discussion of the emission inventory can be found in Section 4.1. Megacities are clearly distinguishable in the anthropogenic emissions of CO in Figure 1.3 as elevated emission sources compared to the surroundings (cf. also Figure 1.1). Fire emissions are predominantly located in the inner continent south of the Amazon basin and in the Amazonas river delta. In contrast to the location of anthropogenic emissions which is constant, it changes with time in the case of biomass burning.

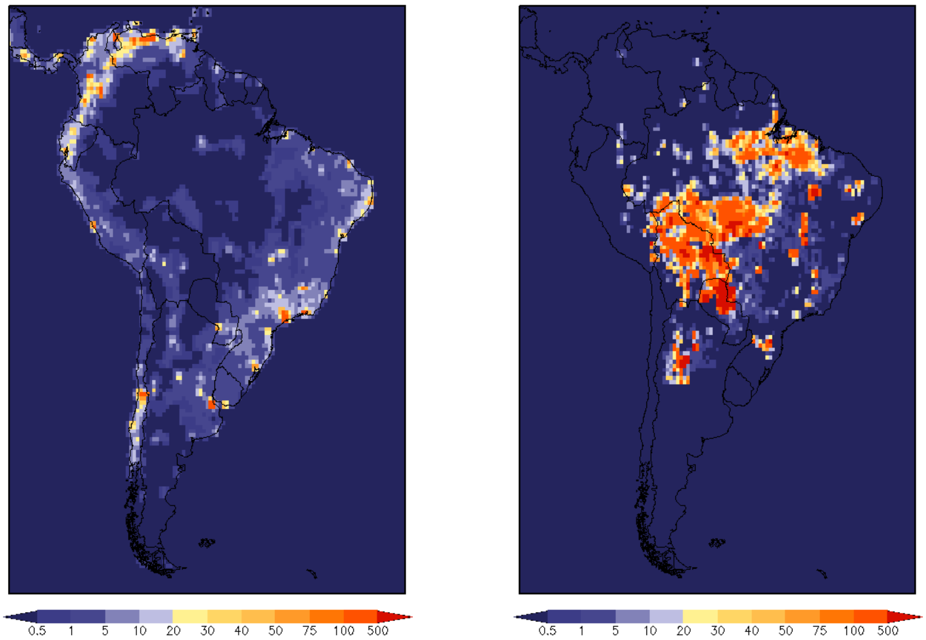

Figure 1.3: Monthly mean CO emissions from anthropogenic sources and from biomass burning for October 2000. The total CO emissions used in this study are plotted in [Gg/(yr · gridbox)] for October 2000 for anthropogenic sources and for biomass burning on the left and on the right hand side, respectively. For details refer to the text and to Section 4.1.

The temporal evolution of the amount of emitted trace gases is different for the two emission sources: Wildland fire emissions are not emitted in constant amounts throughout the year, in contrast to anthropogenic emissions. The latter show a clear seasonal cycle in the amount of emitted trace gases, with high emissions during the dry season in southern hemispheric winter and relatively low emissions in the rest of the year. As an example, the emitted amount of CO for the two different emissions sources is shown in Figure 1.4 for the model domain used in this study. While anthropogenic emissions stay close to the mean emission levels discussed above, emissions from biomass burning show a distinct seasonal cycle: They surpass anthropogenic emissions between June and October 2000 and reach a maximum close to 300 Tg/yr in October while they are distinctively lower than the anthropogenic emissions in the rest of the year. For further details refer to Section 5.1.1.

As an example, CO emissions attributed to megacities in this study are about 4.8 Tg CO/yr. This corresponds to about 19 % of total anthropogenic emissions in South America. Taking into account that they are released in a relatively small area inside the most populated areas in South America, these emissions are supposed to have a considerable impact on air quality and human health. Lawrence et al. (2007) investigate the pollution potential of megacities and large population centers using artificial trace species with different lifetimes. They show a potential for pollution on a regional scale for all South American megacities. They found that long-range and near surface pollutant export of major population centers is generally strongest in middle and high latitudes. The investigation of pollution potentials using a comprehensive chemistry mechanism with realistic tracer concentrations is one of the objectives of this study.

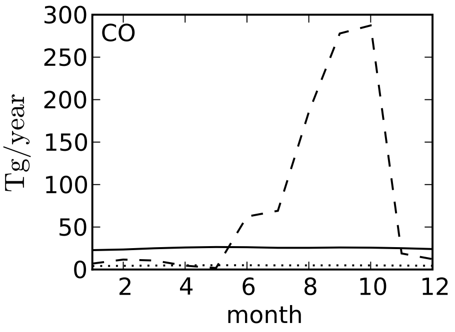

Figure 1.4: Anthropogenic, megacity and biomass burning emissions in South America. The yearly cycle of monthly mean emissions emanating from anthropogenic sources (solid line), megacities (dotted line) and biomass burning (dashed line) are plotted for CO. For details refer to the text.

1.4 Atmospheric tracers

In the description of atmospheric pollution by trace gases, the focus of this study lies on carbon monoxide (CO), ozone (O_3) and nitrogen dioxide (NO_2). The most important chemical processes are shortly summarized in this section. A more detailed description of atmospheric pollutants and chemistry can be found in textbooks, e.g., Brasseur et al. (1999) or Seinfeld and Pandis (2006).

Carbon monoxide

Carbon monoxide is a major air pollutant in the troposphere with direct and indirect sources. When inhaled, it can cause damage to the heart, the nervous system and the brain as it reduces the oxygen-carrying capacity of the blood (e.g., Gorman et al. (2003) and WHO (2000)). In the atmosphere it affects the oxidation capacity by its reaction with the hydroxyl radical (OH). The reaction of OH with methane (CH_4) and CO are the two major sinks of OH (cf. Equation 1.1 and Equation 1.6). In general, OH is an important cleansing-agent in the atmosphere. It serves as the primary atmospheric oxidant and initiates the degradation of many pollutants in the atmosphere. OH concentration has therefore a strong influence on atmospheric air pollution.

As CO affects the atmospheric OH concentration, it indirectly also affects the concentration of other atmospheric trace gases. Via the OH degradation, CO also contributes indirectly to an increase in radiative forcing, as the reaction with OH initiates the degradation process of methane (cf. Equation 1.1), which is an important long-lived greenhouse gas. Additionally, ozone concentrations are enhanced by increased CO concentrations (IPCC, 2007).

One major global source of carbon monoxide is combustion of carbon containing fuels. Ideal (complete) combustion of carbon containing fuels (e.g., coal or oil) would only lead to the production of CO_2 and H_2O. When combustion is incomplete, e.g., when less oxygen is present than it is needed for complete oxidation, carbon monoxide is produced.

According to Schultz et al. (2008a), the most important global emission sources of CO in the decade between 1990 and 1999 are biomass burning (38 %), combustion of fossil fuel (45 %) and, to a lesser extent, biogenic emissions from vegetation (15 %). Emissions from the oceans are of about one order of magnitude smaller than the other emission sources (2 %). Chemical production of CO via methane oxidation and non-methane hydrocarbons (NMHC) oxidation are each of about the same magnitude as the biomass burning source (Brasseur et al., 1999). While methane with its atmospheric residence time of about nine years is uniformly distributed in the atmosphere to a good approximation, concentrations of NMHC strongly depend on the distance from their sources. Accordingly, CO production via NMHC oxidation varies with location.

The chemical production of CO includes a cascade of chemical reactions: After the initial oxidation of methane, which strongly depends on temperature,

$$\mathrm{CH_4 + OH \longrightarrow CH_3 + H_2O} \tag{1.1}$$

the major intermediate in the degradation of methane – formaldehyde ($\mathrm{CH_2O}$) – is produced. Both, photolysis and reaction with OH then lead to the production of CO via:

$$\mathrm{CH_2O} + h\nu \longrightarrow \mathrm{H_2 + CO} \tag{1.2}$$

$$\mathrm{CH_2O} + h\nu \longrightarrow \mathrm{HCO + H} \tag{1.3}$$

$$\mathrm{HCO + O_2 \longrightarrow HO_2 + CO} \tag{1.4}$$

and

$$\mathrm{CH_2O + OH \longrightarrow HCO + H_2O} \tag{1.5}$$

$$\mathrm{HCO + O_2 \longrightarrow HO_2 + CO} \tag{1.4}$$

The most important sink of CO is the chemical loss via reaction with OH:

$$\mathrm{CO + OH \longrightarrow H + CO_2} \tag{1.6}$$

$$\mathrm{H + O_2} + M \longrightarrow \mathrm{HO_2} + M \tag{1.7}$$

Under polluted conditions, $\mathrm{HO_2}$ production via CO can lead to a net ozone production if sufficient ozone precursors like active nitrogen ($\mathrm{NO_x = NO + NO_2}$) are present:

$$\mathrm{HO_2 + NO \longrightarrow OH + NO_2} \tag{1.8}$$

$$\mathrm{NO_2} + h\nu \longrightarrow \mathrm{NO + O} \tag{1.9}$$

$$\mathrm{O + O_2} + M \longrightarrow \mathrm{O_3} + M \tag{1.10}$$

In regions of low NO_x, HO_2 production via CO leads to a net destruction of ozone:

$$O_3 + HO_2 \longrightarrow 2\,O_2 + OH \tag{1.11}$$

Without the influence of any direct anthropogenic emissions, CO concentrations would be largely determined by the chemical equilibrium of production and destruction by the reaction with OH. Mixing ratios of OH and CO would be roughly anticorrelated (Novelli et al., 1998). The minimum of the seasonal cycle of OH concentration would be in winter, when the actinic flux is lowest, accompanied by a maximum in CO concentration.

In reality CO is emitted by various surface sources (e.g., biomass burning or anthropogenic fossil fuel combustion). Global dispersion is favored by its atmospheric residence time of about two months. Novelli et al. (1998) found that while the OH minimum in the southern hemisphere is in June, CO concentrations peak between September and October. They relate this shift of the CO peak to the biomass burning activity in the tropics during the dry season, which therefore dominates the seasonal cycle of CO. The CO mixing ratio peak in South America in the dry season could also be observed by Edwards et al. (2006) using satellite measurements from the MOPITT sensor (see also Section 4.2.2).

Nitrogen Oxides

Nitrogen oxides (NO and NO_2) play an important role in determining air quality. At high concentrations NO_2 is a toxic gas and can have hazardous effects on lung functioning and on the respiratory system. Also relatively low NO_2 concentrations have an adverse effect on the lung and on other organs such as the spleen, liver and blood in combination with long-term exposure (WHO, 2000). Indirectly NO_x leads to the formation of ozone and fine particles, which themselves have adverse effects on humans, animals and plants.

Major anthropogenic sources of NO_x are fossil fuel combustion and biomass burning. Natural sources are soil emissions, lightning, NH_3 oxidation and transport from the stratosphere. In the troposphere, NO_x is mainly emitted as NO, which is then rapidly converted to NO_2. During daytime a steady state between NO and NO_2 is established via the following reactions forming a null cycle for ozone production:

$$NO + O_3 \longrightarrow NO_2 + O_2 \tag{1.12}$$

$$NO_2 + h\nu \longrightarrow NO + O \tag{1.9}$$

$$O + O_2 + M \longrightarrow O_3 + M \tag{1.10}$$

The major mechanism for removal of NO_x from the atmosphere is via the formation of nitric acid (HNO_3) which is then washed out or dry deposited.

During night - when no photolysis of NO_2 takes place - NO_3 is produced via

$$NO_2 + O_3 \longrightarrow NO_3 + O_2 \tag{1.13}$$

As OH concentrations are low during night, NO_3 becomes the major oxidant. Together with NO_2 it reacts to form dinitrogen pentoxide (N_2O_5) which is hydrolysed on aerosols to form nitric acid. At day, NO_3 is rapidly photolysed to NO and NO_2.

In order to track the emitted plumes of distinct emission sources such as megacities or wildland fires, the artificial tracer *total reactive nitrogen* ($NO_y = NO + NO_2 + NO_3 + PAN + HNO_3 +$ other nitrogen containing species) is used in this study. It consists of the sum of all reactive nitrogen species. In the atmosphere, it only undergoes emission, transport and deposition and has therefore the characteristics of a passive tracer. Additionally, it is more easily measured than its single components. NO_y volume mixing ratio in the atmosphere can decrease with mixing of air masses and dry and wet deposition of its constituents.

Ozone

Stratospheric ozone protects life on earth from hazardous shortwave radiation. It absorbs ultraviolet radiation at wavelengths between 240 and 320 nm and hinders its propagation to the ground. In the troposphere, ozone is harmful to plants and humans. At high concentrations it causes respiratory problems and can finally lead to increased death rates during smog events and at constant rather high concentrations throughout the year.

As a secondary pollutant, ozone is not emitted but chemically produced in the atmosphere. Chemical production of ozone in the troposphere typically involves the ozone precursors NO_x and nonmethane hydrocarbons (NMHC). In a reaction chain, NMHC is consumed while NO_x acts as a catalyst. If NMHC concentrations are relatively small (this is the case, e.g., for the remote areas away from emission sources and for the free troposphere), CO and NH_3 are oxidized instead of NMHC. The reaction chain involving CO oxidation consists of Equations 1.6 - 1.10.

Close to large NO emission sources (e.g., power plants) and at night, ozone concentrations are reduced by Equation 1.12. Due to the high local NO concentration or the missing solar radiation at night, Equation 1.12 is not immediately counterbalanced by Equations 1.9 - 1.10. This process is referred to as *NO_x titration*. Further downwind of the emission sources, NO_2 is converted back to ozone, leading to elevated ozone concentrations in a larger distance (e.g., Gillani and Pleim, 1996).

Depending on the ambient concentration of NO_x and volatile organic compounds (VOCs) as well as on the solar insolation, ozone production occurs. Two different ozone production regimes can be distinguished for the highly nonlinear chemistry of tropospheric ozone:

- VOC limited ozone production
- NO_x limited ozone production

In the case of comparatively high VOC concentrations, ozone is likely to be NO_x limited. This means that a decrease in NO_x concentrations would lead to a decrease in ozone production, whereas a comparative change in VOC concentrations would only have a minor effect. In unpolluted rural areas, NO_x limited ozone production is predominant. These areas are located away from anthropogenic emissions sources and are dominated by biogenic emissions.

VOC limited ozone production takes place when a certain percent reduction in VOC would lead to a relatively high decrease in ozone production, whereas a reduction of the same percentage in NO_x would only have minor effects. Between the two cases is a broad transition region. Under some circumstances, a decrease in NO_x can even lead to an increase in ozone production. Further details can be found, e.g., in the article of Sillman (1999).

The two ozone production regimes discussed in the previous section are not only of great scientific importance in understanding ozone production, they are also relevant for policy, when air quality measures are under discussion: A certain limitation of NO_x or VOC emissions has a different impact on ozone concentrations, depending on the predominant ozone production regime. The different ozone production regimes are investigated in Chapter 5 for two study regions.

1.5 Motivation and Objectives

Despite the importance of regional air quality perturbations due to megacity emissions described above, there is no study investigating the importance of emissions emanating from South American megacities onto the regional air quality on a continental scale using a comprehensive chemical mechanism together with a regional climate model. This work tries to close this gap to a certain extent. Using the regional climate model REMO together with a comprehensive chemical mechanism, the following questions are addressed:

- To what extent do emissions from megacities and biomass burning influence the air quality in South America?
- How much is the population affected by the different emission sources?
- What are the dominant ozone production regimes in the outflow of pollutants from the megacities?

The structure of the thesis is the following:

In *Chapter 2* the numerical model REMO$_{\texttt{chem}}$ used in this study is described as well as adaptations which are necessary in order to tackle the main research questions.

Chapter 3 focuses on the ability of REMO$_{\texttt{chem}}$ to reproduce South American climate.

In chapter *Chapter 4*, simulated trace gas concentrations are compared to different measurements in order to evaluate the capability of REMO$_{\texttt{chem}}$ to reproduce present trace gas profiles and horizontal patterns.

In chapter *Chapter 5* the impact on regional air quality of the different emissions sources is investigated using different model runs with modified emission scenarios. Ozone production regimes are analyzed in detail for two periods, inside and outside the biomass burning season.

The overall conclusions and an outlook are given in *Chapter 6*.

2 The Regional Climate Model REMO

Regional climate models (RCMs) are frequently used to simulate climate and to project future climate change signals in different regions all over the world (e.g., Jacob, 2009; Jacob et al., 2007; Déqué et al., 2007; Pal et al., 2007; Giorgi, 2006). They simulate atmospheric processes at high resolution in a restricted area of the globe – the model domain. For many studies – including the analysis of air pollution transport and chemistry – important fine scale dynamical processes influenced, e.g., by orography, can only be resolved at the high resolution of an RCM. The restriction of the RCM to the model domain permits computationally efficient simulations on climate time-scales.

An RCM including chemistry is an appropriate tool to investigate the influence of air pollution emanating from Megacities on a monthly to decadal scale onto a continental region like South America. To assess the impact of pollutants emitted by various sources, offline chemistry transport models (CTMs) are used as well as RCMs with online coupled chemistry. CTMs are widely used to assess the impact of climate change and emissions on tracer concentrations and air quality (Giorgi and Meleux, 2007). Recently RCMs including online-chemistry are used to investigate the impact of future global climate change on the regional distribution of photooxidants, e.g., Forkel and Knoche (2006), as well as for impact and sensitivity studies (e.g., Marmer and Langmann, 2005; Langmann and Bauer, 2002).

CTMs use meteorological fields as input to compute transport and chemical processes of tracers. An advantage of CTMs is the relatively low computational cost compared to online-chemistry modelling. A disadvantage is the low temporal resolution of meteorological information which is available for the chemical mechanism and transport processes. Also, important meteorological information might be missing to the CTM as, e.g., the convective mass flux is normally not stored by meteorological models. The main advantage of online-chemistry modelling is the availability of all meteorological information at every model timestep. Additionally an RCM including online-chemistry can take into account feedback processes of the chemistry onto meteorological processes, e.g., the different aerosol-cloud feedback mechanisms.

In this study the regional climate model REMO (*REgional MOdel*) is used to investigate regional climate and air pollution in South America. The model has been improved in the frame of this study to fit the needs of studying air pollution and climate.

In this chapter the REMO model used in this study is described. Meteorological mechanisms are shortly summarized in Section 2.1, but the focus lies on the chemical mechanism described in Section 2.2. Modifications made in the model chemistry are also discussed.

2.1 Meteorology

REMO is a three-dimensional hydrostatic regional atmospheric circulation model. It is based on a weather forecast model: The dynamical core is adapted from the former weather prediction model (Europamodell) of the German weather service (DWD) (Majewski, 1991). In the dynamical core, the discretized primitive equations of the atmospheric motions are solved (e.g., Holton, 2004). The physical parametrizations follow those of the general circulation model (GCM) ECHAM4 (Roeckner et al., 1996).

The prognostic variables are surface pressure, temperature, specific humidity, cloud water and the horizontal wind components. They are calculated for each model timestep using the leap-frog scheme with semi-implicit corrections and Asselin filter (Asselin, 1972). In the horizontal direction the prognostic variables are defined on an Arakawa-C grid (see Figure 2.1 and Arakawa and Lamb (1977)): Scalar variables are located in the center of each grid box (φ in Figure 2.1) whereas the two wind vectors are located on the intersections between the grid boxes (u and v in Figure 2.1 for the zonal and meridional wind component, respectively). The advantage of the Arakawa-C grid is that it better represents the phase speed and the group velocity of the shortest waves than an unstaggered grid, where the speed of the shortest resolvable wave is zero. The Arakawa-C grid is widely used in atmospheric models, because it has the best dispersion properties of all Arakawa grids. Grid centers are located on a rotated latitude-longitude grid.

The vertical direction is discretized using a hybrid sigma-pressure coordinate system (Figure 2.2): The lowest levels near the surface are mainly terrain-following. With increasing height, the influence of the orography on the level-shape decreases until

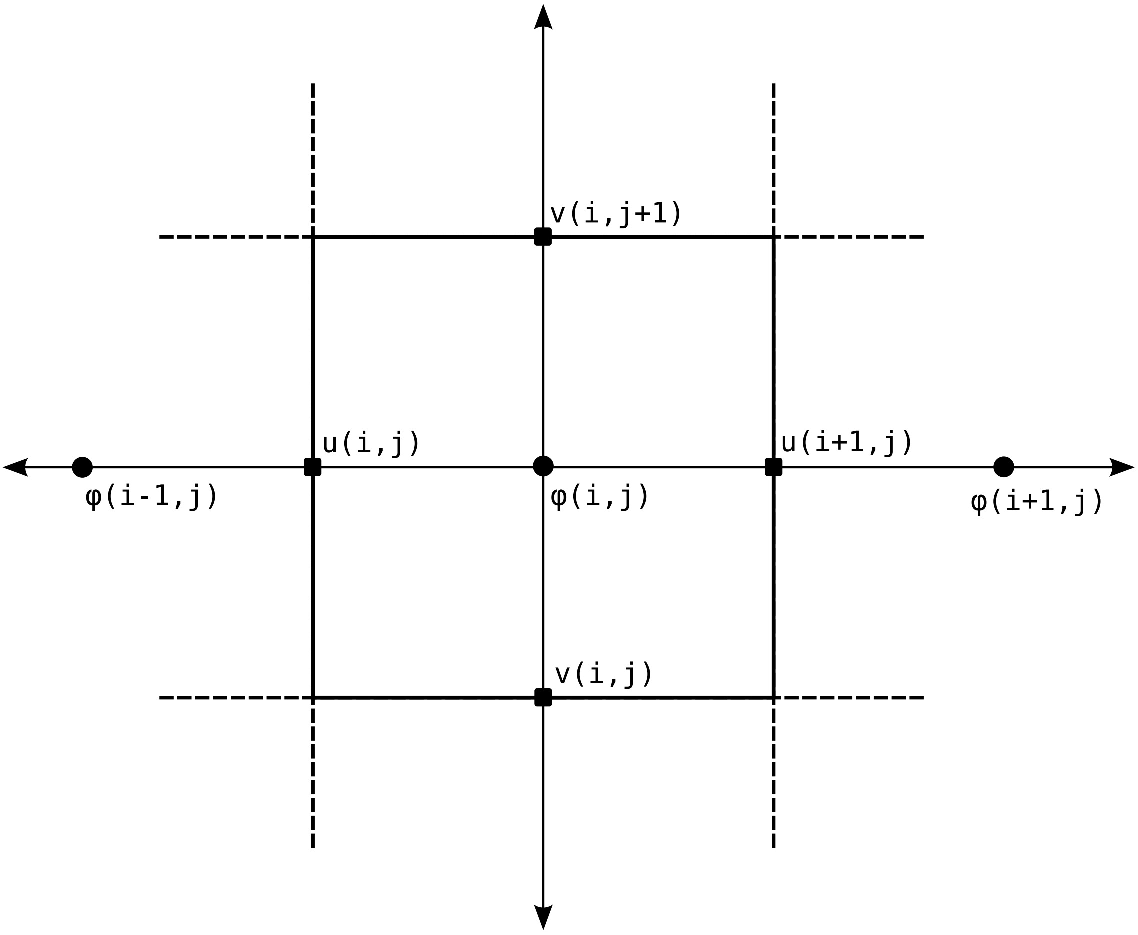

Figure 2.1: Arakawa-C grid. A grid box of an Arakawa-C grid is shown. Scalar values (φ) are defined in the center of the grid boxes, while wind-vector components (u, v) are located at the border of the grid box

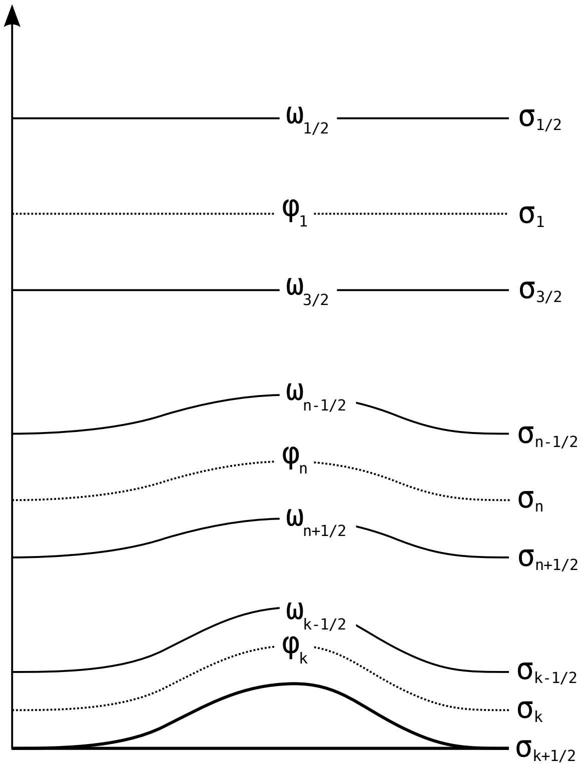

Figure 2.2: σ-coordinate system. The vertical grid consisting of a σ-coordinate system is shown. Scalar values (φ) are defined in the center of the layers (at full-levels), while vertical velocities (w) are located at the layer boundaries (at half-levels)

the uppermost levels are equal to pure pressure levels. The vertical levels extend up to 10 hPa. Prognostic variables are stored on full-levels in the center of each layer (φ in Figure 2.2). Vertical velocities are defined on half-levels at the layer boundaries (ω in Figure 2.2). Throughout this study a vertical grid consisting of $k = 31$ layers is used.

The horizontal standard resolutions of REMO are $^1/_2\,^\circ$ (ca. 55 km), $^1/_6\,^\circ$ (ca. 18 km) and 0.088 ° (ca. 10 km) with a timestep of 240 s, 100 s and 30 s, respectively. The vertical standard resolution consists of 20 or 31 sigma-levels. In this study the horizontal resolution of $^1/_2\,^\circ$ is used with a timestep of 240 s and a vertical resolution of 31 sigma-levels.

An RCM simulates meteorological processes on a part of the globe – the model domain. Processes outside the domain – although potentially important – are not calculated by the regional model itself. They are taken into account using model output from a global model, which is usually performed on a much coarser horizontal resolution than the regional model.

At the lateral boundary the prognostic variables surface pressure, temperature, the two horizontal wind components and specific humidity are prescribed by global meteorological fields. They are adjusted in a lateral boundary zone of eight grid boxes according to Davies (1976): The influence of the large-scale driving fields decrease exponentially going from the lateral border of the domain towards the center. At the lower boundary the model is forced by the sea surface temperature (SST) and by the sea ice distribution over sea. The SST and the sea ice distribution can be taken from a GCM, re-analysis or observation data. It is also possible to couple REMO with a regional ocean model where the SST and the sea ice extend are calculated online. The sea ice distribution can also be diagnosed from the SST. Over land, surface characteristics such as surface roughness length, surface albedo, vegetation ratio and leaf area index determine the lower boundary condition for the atmosphere together with surface temperature and moisture. The surface characteristics are prescribed during the simulation. While the roughness length is constant with time, surface albedo, vegetation ratio and leaf area index are prescribed on an annual cycle (for details refer to Rechid and Jacob, 2006). Surface temperature and moisture are initialized at the beginning of the simulation. During the simulation they are calculated by the soil scheme of REMO without further external forcing. There is no forcing for the meteorological prognostic species at the upper boundary.

As global meteorological driving fields re-analysis data, e.g., from the National Center for Atmospheric Research (NCAR) or the European Center for Medium-Range Weather Forecasts (ECMWF) can be used as well as boundary data from GCMs like ECHAM5. Throughout this study the ERA-40 re-analysis data (Uppala et al., 2005) from the ECMWF is used as lateral boundary forcing for the meteorological prognostic variables. The sea surface temperature as well as the initial meteorological fields are also taken from the ERA-40 re-analysis data.

Subgrid scale physical processes that are not resolved by the model can still be important for the quality of the model results. Those processes have to be parametrized using the prognostic variables calculated by the model. As mentioned above, the physical parametrization included in REMO follow those of the GCM ECHAM4 with several modifications (for details refer to Jacob et al. (2001, 2007)). Additionally a fractional surface cover was introduced by Semmler (2002) which takes into account the different subgrid scale surface processes on land water and sea ice. The monthly variation of the vegetation parameters background albedo, leaf area index and vegetation ratio were included in REMO by Rechid and Jacob (2006). The cumulus convection mass flux scheme is parametrized after Tiedtke (1989) with modifications after Nordeng (1994). It has been modified for chemical tracers in the frame of this study. This is described in Section 2.2.3.

2.2 Chemistry

To investigate the dissemination of tracers and pollutants emanating from natural as well as anthropogenic emission sources, several processes determining the tracer concentrations need to be included in the model. Tracer concentrations are influenced by horizontal and vertical transport processes like advection or convective up- and downdrafts. They are subject to deposition processes and processes on a subgrid scale, which are parameterized as diffusion in the model. Chemical reactions lead to production and loss of chemical species, depending on the actual conditions at a certain location.

Finally, natural as well as anthropogenic emissions have an influence on tracer concentrations and are released near the surface at the lower boundary. At the lateral boundaries as well as at the upper boundary tracers are transported into the model domain.

In the frame of this study online-chemistry and transport processes are implemented in the newest operational model version of REMO (REMO 5.7). They are partly adopted from the implementation of online-chemistry into an older REMO version (REMO 5.0) as described in Langmann (2000). The latter implementation is originally based on Hass (1991). Meteorological processes are influencing the chemical processes at every model timestep as described above. The reverse influence of the chemical processes and tracers onto the meteorology is not implemented in the frame of this study. An example of a feedback process is the influence of tropospheric ozone on the radiation balance of the earth, where tropospheric ozone acts as a greenhouse gas (e.g., IPCC, 2007). It has the disadvantage of missing feedbacks from the chemistry onto the meteorology and thus being less realistic. An advantage is the ability of being able to investigate the chemical mechanism independently from the meteorology. Different case studies, e.g., with modified emission inventories, are subject to exactly the same meteorological conditions. Thus, differences in resulting trace gas concentrations can be attributed to the chemical mechanism and to the modifications made, e.g., to the emission inventory.

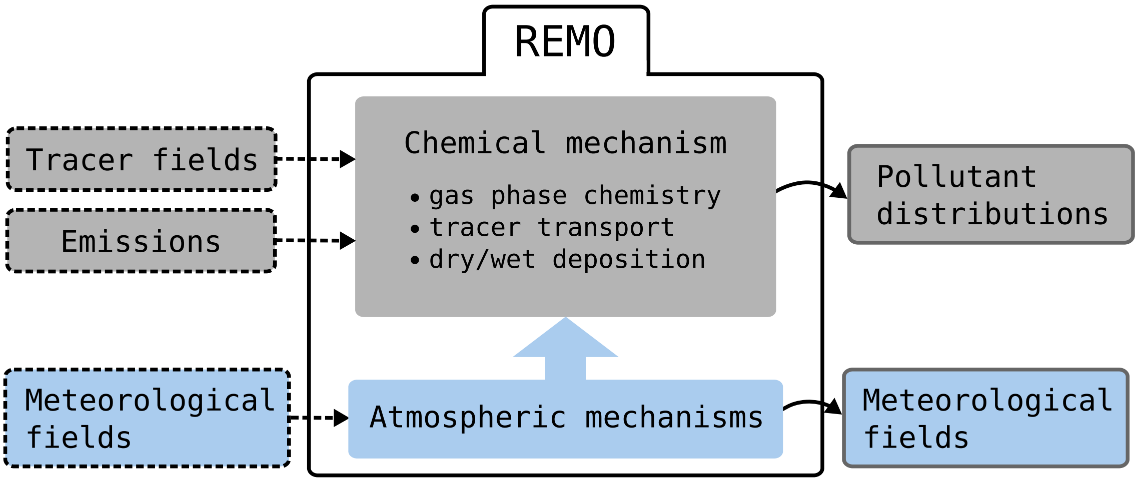

Figure 2.3: The REgional MOdel. Organigram showing REMO with chemistry and tracer transport included. For details refer to the text.

In Figure 2.3 REMO including chemistry is depicted. Emissions are released at the lower boundary, while tracer fields serve as lateral and upper boundary conditions for the chemical mechanism. Meteorological fields containing the prognostic variables of the large-scale forcing are used to drive the atmospheric mechanisms. The latter are influencing the chemical mechanism during a model simulation, i.e., gas phase chemistry, tracer transport, dry and wet deposition are computed using the meteorological conditions. The model output are the pollutant distributions and the meteorological fields on the high resolution grid in the model domain of REMO.

In the following sections, processes influencing tracer concentrations are described in more detail. The boundary treatment is discussed as well as modifications in the convection scheme, which avoid erroneous oscillations leading to negative tracer concentrations.

2.2.1 Chemical Species Transformation

To be able to calculate the concentration of chemical tracers, all main processes that influence the concentration have to be taken into account by the model. The change of mixing ratio C_i of a chemical species i is determined by

$$\begin{aligned}\frac{\partial C_\mathrm{i}}{\partial t} &= -\nabla(\mathbf{v}C_\mathrm{i}) + \frac{\partial}{\partial z}(k_\mathrm{z}\frac{\partial}{\partial z}C_\mathrm{i}) + \left(\frac{\partial C_\mathrm{i}}{\partial t}\right)_\mathrm{drydep} + \left(\frac{\partial C_\mathrm{i}}{\partial t}\right)_\mathrm{wetdep} + \left(\frac{\partial C_\mathrm{i}}{\partial t}\right)_\mathrm{conv} \\ &\quad + P_\mathrm{i} - L_\mathrm{i} + E_\mathrm{i}, \end{aligned} \tag{2.1}$$

where t is the time, $\mathbf{v}$ the velocity vector, z the vertical coordinate and k_z the vertical eddy diffusion coefficient. The first term on the right hand side is the change in concentration due horizontal and vertical advection. The second term describes the vertical diffusion (it is not necessary to take into account horizontal diffusion, which is much smaller than horizontal advection). The third and fourth term of Equation 2.1 take into account the dry and wet deposition processes of chemical species, respectively. The fifth term describes the change in tracer concentration due to convective up- and downdrafts. The last three terms describe production (P_i) and loss (L_i) of chemical species due to chemical reactions and the concentration change due to emission processes (E_i).

In the following the different processes represented in Equation 2.1 and their implementation in the model are described.

Transport Processes

Transport processes like vertical diffusion for chemical tracers are similar to the corresponding processes in the meteorological mechanism for prognostic species like, e.g., specific humidity. Horizontal and vertical advection are treated differently for the meteorological and chemical prognostic variables: Advection of meteorological prognostic variables is calculated using second order centered differences for horizontal advection, while vertical advection follow Simmons and Burridge (1981). Chemical prognostic variables are advected using the scheme by Smolarkiewicz (1983) discussed below. Other transport processes like dry deposition are chemistry specific. Transport due to convection and wet deposition will be discussed below this section.

In the chemical mechanism of REMO the horizontal grid used is an Arakawa-C grid (see Section 2.1). The horizontal discretization of the tracer field and the wind field is done in analogy to the meteorological part of the model: The prognostic scalar variables of the chemical mechanism are the tracer concentrations. They are defined in the center of each grid box (φ in Figure 2.1). Also the wind vector components are the same as in the meteorological mechanism.

For the vertical discretization of the atmosphere a terrain-following σ-coordinate system is used as described in Section 2.1. Mean tracer concentrations as well as the meteorological prognostic variables are stored on full-levels in the center of each layer (φ in Figure 2.2).

The advection scheme used for horizontal and vertical advection for chemical tracers uses the two step approach of Smolarkiewicz (1983, 1984) to avoid numerical diffusion. The Smolarkiewicz scheme consists of the upstream method, but additionally includes a diffusion correction as a second step. The scheme is mass conserving, positive definite and computational efficient. Monotonicity can be achieved using higher order flux corrections. The numerical diffusion is reversed using an "antidiffusion velocity". This step can be repeated to increase accuracy. In this study the Smolarkiewicz scheme is used including two corrective steps.

Vertical turbulent diffusion fluxes are calculated according to Louis (1979) for the lowest model layer. Above – in the planetary boundary layer – vertical turbulent transport is calculated according to Mellor and Yamada (1974) using a hierarchy level 2 scheme.

Dry deposition in the lowest model layer is calculated after Wesely (1989). Using the resistance approach, the deposition velocity v_d is calculated as

$$v_\mathrm{d} = \frac{1}{r_\mathrm{aero} + r_\mathrm{lam} + r_\mathrm{surf}}. \tag{2.2}$$

Aerodynamic resistance due to turbulence in the surface layer is represented by r_aero. Resistance of the quasilaminar sublayer is denoted as r_lam, while the bulk surface resistance is represented by r_{surf}. The latter depends among others on surface type, solar irradiance, temperature, species reactivity and solubility and the ratio of molecular diffusivity of the species to that of water vapor. The only gas property that influences r_{lam} is its molecular diffusivity in air, while r_{aero} is the same for all trace gases.

Using the dry deposition velocity from Equation 2.2, the concentration change of chemical tracers due to dry deposition in Equation 2.1 is calculated as

$$\left(\frac{\partial C_{\mathrm{i}}}{\partial t}\right)_{\mathrm{drydep}} = -\frac{v_{\mathrm{d}} C_{\mathrm{i}}}{\Delta\sigma}, \tag{2.3}$$

where $\Delta\sigma$ is the thickness of the lowest model layer (see Figure 2.2).

Cloud Processes

Processes changing the tracer concentrations in clouds are wet deposition, convection and aqueous chemistry.

Wet deposition as well as aqueous phase chemistry are implemented after Walcek and Taylor (1986). They are calculated for the cloudy fraction of a grid box from the lowest model layer to the cloud top for precipitating clouds and from cloud bottom to cloud top for non-precipitating clouds.

Convection of chemical tracers is implemented after Tiedtke (1989) similar to the convection of liquid water in the meteorological mechanism. The convection scheme for tracers has to assure positive definite tracer concentrations. Unfortunately the scheme of Tiedtke (1989) cannot assure positive tracer concentrations for all possible meteorological situations. In the frame of this study, the convection scheme for the tracers was modified according to Brinkop and Sausen (1997). Details of the modified convection scheme are described in Section 2.2.3.

Gas Phase Transformation

The gas phase reactions are implemented after the mechanism of the second generation Regional Acid Deposition Model (RADM2) (Stockwell et al., 1990). It is of medium complexity including all significant reactions for predicting the major pollutants of the troposphere like ozone, NO_x or CO. On the other hand it is relatively simple compared to the real atmosphere, which is necessary due to limited computing time. Highly detailed chemical mechanisms like, e.g., the Master Chemical

Mechanism (Derwent et al., 1998), which contains more than 2000 chemical species and more than 7100 chemical reactions for the most important 120 organic compounds, are not practical to use in climate models at present: The computational demand of processor time and memory is too great. Therefore the full complexity of the organic chemistry of the troposphere is not treated explicitly. To save computing time, a reactivity lumped approach is used instead of treating all species explicitly. Volatile organic compounds (VOCs) are lumped into surrogate species based on their similarity of reactivity with OH and based on their similarity of emissions (Middleton et al., 1990).

Altogether the implemented chemistry mechanism consists of 63 species, of which 39 species are prognosed and 19 species are diagnosed. Concentrations of water are taken from the meteorological mechanism and the remaining 3 species, molecular oxygen, molecular nitrogen and methane are kept constant due to their high abundance in the atmosphere. Chemical species are listed in Appendix A.

Trace species are subject to production and loss (P_i and L_i in Equation 2.1, respectively) in 136 thermal chemical reactions, 21 photolysis reactions and 17 aqueous equilibrium reactions. The chemical reactions can be found in Appendix B.

The RADM2 mechanism contains 21 inorganic species, which are represented by 14 moderately reacting species, 4 highly reactive intermediates and three abundant species (oxygen, nitrogen and water). A standard scheme for the inorganic tropospheric chemistry is incorporated in the RADM2 mechanism.

Tropospheric organic chemistry uses a reactivity lumped approach as mentioned above. In RADM2, it contains 16 highly reactive peroxy radicals and 26 moderate-reacting species. VOCs are aggregated into 26 classes of reactive organic species containing lumped and explicitly treated species: *Alkanes* are represented by methane, ethane and three higher lumped groups. They react slowly in the atmosphere and their only important loss process is the reaction with OH. Therefore they can be transported over large distances. The *alkenes* in the RADM2 mechanism are ethene and isoprene and the two lumped species terminal and internal alkenes. They are most reactive with respect to OH and have a large influence on the NO to NO_2 conversion. They are emitted by biogenic and anthropogenic sources. Ethene and isoprene are treated explicitly, because of their relatively low and high reactivity, respectively. Degradation of isoprene plays an important role in the formation of ozone, especially in the remote troposphere. The *aromatics* in the RADM2 mechanism are cresol and the two lumped groups toluene and xylene. Under conditions with high anthropogenic pollution, e.g., in urban areas, aromatic chemistry is very important. *Carbonyls* in RADM2 are formaldehyde and the lumped classes acetaldehyde, ketones, glyoxal, methylglyoxal and another class representing other dicarbonyls. In the degradation process of a large number of organic compounds, aldehydes and ketones are formed as intermediate products. They react with OH, HO_2 and NO_3 and are also photolysed in the atmosphere. Three groups represent *organic nitrates* in RADM2: peroxyacetylnitrate (PAN), higher PANs and other organic nitrates. PAN is a secondary pollutant, which is present in photochemical smog. *Organic peroxides* and *organic intermediates* are represented by 16 lumped species in RADM2 (see Appendix A). They are highly reactive and affect strongly photochemical transformations under rural and clean conditions. Two *organic acids* are included in the RADM2 mechanism: formic and acetic acid. They are produced as water soluble products of the oxidation of different organic compounds and are important when considering anthropogenic air pollution, e.g., in urban areas.

The RADM2 mechanism is implemented using a quasi-steady-state approximation (QSSA) method (Hesstvedt et al., 1978). Such QSSA methods are used to solve so called *stiff* differential equation systems, where the characteristic time constants of the single differential equations vary in a relatively large range, leading to time step constraints when conventional methods are applied. In the QSSA method, a steady state is assumed for very reactive species, as they rapidly transform to their equilibrium values:

$$\frac{\partial C_\mathrm{i}}{\partial t} = 0 \tag{2.4}$$

For the other species the integration is done according to

$$\frac{\partial C_\mathrm{i}}{\partial t} = P_\mathrm{i}(C_\mathrm{j}) - \frac{C_\mathrm{i}}{\tau_\mathrm{i}(C_\mathrm{j})} \tag{2.5}$$

with the production rate $P_\mathrm{i}(C_\mathrm{j})$ and the characteristic time for the first order chemical loss $\tau_\mathrm{i}(C_\mathrm{j})$ of a species i. Both depend explicitly on the concentrations of other species C_j and are constant during a timestep of the chemical mechanism Δt_c. This timestep is smaller than the timestep of the meteorological mechanism and is calculated depending on the tracer tendencies, being small for large concentration gradients and vice versa. With $P_\mathrm{i}(C_\mathrm{j})$ and $\tau_\mathrm{i}(C_\mathrm{j})$ being constant during a timestep Δt_c, Equation 2.5 is solved as

$$C_\mathrm{i}(t + \Delta t_\mathrm{c}) = P_\mathrm{i}\tau_\mathrm{i} + (C_\mathrm{i}(t) - P_\mathrm{i}\tau_\mathrm{i})e^{\frac{-\Delta t_\mathrm{c}}{\tau_\mathrm{i}}} \tag{2.6}$$

where $P_\mathrm{i}\tau_\mathrm{i}$ corresponds to the photochemical equilibrium concentration. For further details refer to Hesstvedt et al. (1978).

The reaction rates of photochemical reactions (i.e., the photodissociation rate coefficients denoted as J values) depend on the actinic flux (q), i.e., the solar insolation, and on fundamental properties of the molecules (absorption cross section (σ) and quantum yield for photodissociation (Φ)). While the absorption cross section depends on temperature and the quantum yield on temperature and pressure, the actinic flux depends on altitude and solar zenith angle. All factors are functions of the wavelength of the incident light (λ).

In order to calculate the total photochemical reaction rate (for incident natural solar light) of a certain photolysis reaction (for specie X), it is necessary to calculate the integral over all wavelengths of the product of the actinic flux (q), the molecular absorption cross section (σ_X) and the quantum yield for photodissociation (Φ_X):

$$J_\mathrm{X} = \int_\lambda q(\lambda)\,\sigma_\mathrm{X}(\lambda)\,\Phi_\mathrm{X}(\lambda)\,\mathrm{d}\lambda \tag{2.7}$$

An example for a photolysis reaction is the photodissociation of $\mathrm{NO_2}$ which is a main source of ozone in the troposphere together with Reaction 2.9:

$$\mathrm{NO_2} + h\nu \longrightarrow \mathrm{NO} + \mathrm{O(^3P)} \tag{2.8}$$

$$\mathrm{O(^3P)} + \mathrm{O_2} + \mathrm{M} \longrightarrow \mathrm{O_3} + \mathrm{M} \tag{2.9}$$

where h is Planck's constant and ν the frequency of the electromagnetic wave associated with the absorbed photon. Reaction 2.8 takes place for wavelength $250\,\mathrm{nm} < \lambda < 400\,\mathrm{nm}$ with an approximate reaction rate $J_{\mathrm{NO_2}} \approx 8 \times 10^{-3}\,\mathrm{s^{-1}}$ for a solar zenith angle of 40° in June on a summer surface at 40° north latitude. As the required energy of the photon is relatively low, the reaction takes place at all altitudes.

Clear sky photolysis rates are calculated in a preprocessor using the Tropospheric Ultraviolet and Visible (TUV) radiation model (version 4.4) (Madronich and Flocke, 1999). The TUV radiation model calculates clear sky photolysis rates together with the spectral irradiance and the spectral actinic flux using the discrete ordinates method described by Stamnes et al. (1988) as radiative transfer scheme. It is modified to allow pseudo-spherical corrections: Multiple scattering is calculated in a plane-parallel geometry, while the propagation of the direct solar beam is calculated in spherical geometry. Wavelengths between 120 and 735 nm are considered in the computation. Photolysis rates are calculated following Equation 2.7, taking into account temperature dependencies of absorption cross section and quantum yield as well as pressure dependencies of quantum yield for selected photolysis rates. For further details see Madronich and Flocke (1999) and references therein. In this study, photolysis rates are tabulated for each month. They are stored for different latitudes, different times of day and different altitudes.

During a model simulation clear sky photolysis rates are modified taking into account the actual cloud cover in a grid box. This leads to reduced photolysis rates below the cloud, which can approach zero for optically thick clouds. Above the cloud, photolysis rates are enhanced due to reflected sunlight at the cloud top, increasing the actinic flux. Inside the cloud, photolysis rates are either enhanced or decreased by the presence of the cloud depending on the solar zenith angle.

For a cloud with an optical depth greater than 5, photolysis rates are modified in REMO$_{\texttt{chem}}$ according to

$$J_{\mathrm{X}} = J_{\mathrm{X}}^{\mathrm{clear}}(1 + f^{\mathrm{cloud}}(F_{\mathrm{cloud}} - 1)) \tag{2.10}$$

where $J_{\mathrm{X}}^{\mathrm{clear}}$ is the clear-sky photolysis rate (for the photolysis of a specie X), f^{cloud} is the fractional cloud coverage in a grid box and F_{cloud} denotes a correction function. The latter takes into account the differences in the solar actinic flux for below-cloud, in-cloud and above-cloud situations. It depends on the solar zenith angle, cloud optical depth and transmission coefficients. For further details refer to Chang et al. (1987).

Photolysis rates are a major source of uncertainty in the gas phase chemistry mechanism. Many trace species in the atmosphere are degraded via the oxidation by the hydroxyl radical, which is created by photolysis of ozone. Therefore the concentration of many trace species is indirectly influenced by the magnitude of the photolysis rates. The main uncertainty in the determination in the photolysis rates is the determination of the actinic flux, which is modulated by a variety of factors, but has a main uncertainty in cloud cover. The relation between cloud cover and trace gas concentrations in the atmosphere, is investigated, e.g., by Tie et al. (2003). Comparing cloudy conditions with clear-sky conditions in a global model, they found that the presence of clouds lead to a 20 % increase in OH concentrations and therefore to a higher oxidation capacity of the troposphere. Additionally, clouds lead to an increase in ozone in the upper troposphere due to the changes in the photolysis rates: backscattered radiation from clouds lead to an increase in the actinic flux and as a consequence to increased photolysis rates (e.g., Voulgarakis et al., 2009).

2.2.2 Boundary Treatment

Like in the meteorological part of the model the treatment of the regional model domain boundaries is crucial in regional modelling. Chemical tracer enter and leave the regional model domain via the boundaries. In the following sections the treatment of the different boundaries (lateral, upper and lower boundary) is described.

Lateral and Upper Boundary

Long-lived species like CO or ethane can be transported over large distances. Sources of long-lived species can be far away from the region of interest and tracer undergo chemical transformations during the transport into this region. Additionally, chemical processes in the upper levels of the model domain are influenced by transport of species from the stratosphere, e.g., ozone. To take into account sources and chemical processes outside the regional model domain, global chemistry model data (from a chemical driving model) are used as lateral and upper boundary condition. In this study trace gas concentrations from the global chemical transport model MOZART-4 are used as described in Section 4.1.

At the lateral boundaries the treatment of the influence of the driving model data is implemented after Pleim et al. (1991). Horizontally and vertically interpolated (if needed) tracer concentrations from the driving model are prescribed in the outermost lateral grid boxes in distinct time intervals (they usually correspond to the output time intervals of the driving model). In the time intervals between two updates of tracer concentrations, they are interpolated linearly in time. Discontinuities of the advective flux field and the concentration field at the lateral boundaries would lead to upstream reflections near the outflow boundary. In order to minimize the discontinuities, the flux divergence in the grid boxes next to the boundary are set to zero and upstream influences caused by lateral boundary conditions are avoided.

In order to take into account influences of downward species transport, e.g., transport of ozone from the lower stratosphere into the troposphere, also the upper boundary has to be updated by tracer concentrations from the chemical driving model. Species concentrations are prescribed and updated in the upper five model layers in distinct time intervals in the same way as the lateral boundaries are updated.

Unlike the meteorological part, where all prognostic variables are updated in the same time interval at the lateral boundaries, in the chemical part of REMO different types of tracers are distinguished. Long-lived species that can be transported over a large distance have to be updated more frequent than shorter living species. In REMO, two types of species are distinguished: Long-living species are updated three hourly or daily, while short-lived species are kept constant at the lateral and upper boundary.

Lower Boundary - Emissions

One of the most important factors to determine the tracer concentrations in the atmosphere are emissions at the surface – the lower boundary. Surface emissions can be seen as the sum of natural and anthropogenic emissions. Before the industrial revolution (about 1850), the amount of anthropogenic emissions was negligible relative to natural emissions with respect to the influence on tracer concentrations in the atmosphere. Today, in many highly industrialized regions of the world, anthropogenic emissions are the most important factor influencing the regional air quality.

In REMO, monthly mean emission values are used to modify the tracer concentrations in the lowest model layer. The production rate due to emissions is simply added to the production rate of the chemical processes in the lower model grid cells, in which trace gases are emitted. In the future, it is planned to take into account the different injection heights for different emission sources and therefore extend the increase of species concentration due to emissions to higher layers in the model atmosphere. This is necessary, because vegetation fire emissions in the Amazon region, e.g., can reach an effective injection height of several kilometers due to strong initial buoyancy related to the heat release of the fires (Freitas et al., 2006). Neglecting this process in the present model leads to an underestimation of pollutant concentration in the vicinity of the fire emission sources and to an underestimation of their long range transport. As anthropogenic emissions, e.g., emanating from megacities don't have a comparably high buoyancy with respect to fire emissions, their release in the lowest model layer is a rather good approximation. Nevertheless, one has to keep in mind that the vegetation fire plume can also influence air quality and chemistry in the vicinity of megacities.

2.2.3 Modified Convection Scheme

Tracer transport due to cumulus convection is one of the most important transport processes in the troposphere. Tracers are convected from the lower layers of the atmosphere and are redistributed vertically to higher altitudes where they can be transported by strong winds over large distances. Convective transport – as well as all other transport processes – has to assure positive tracer concentrations. As already mentioned in Section 2.2.1 the convection scheme of Tiedtke (1989) doesn't assure positive tracer concentrations for all meteorological situations. It therefore had to be modified according to Brinkop and Sausen (1997) in the frame of this thesis. In the following the modifications in the Tiedtke convection are shortly summarized. Different profiles and the different development with time of an artificial tracer are shown for the original and for the new convection scheme.

Implementation of the Modified Convection Scheme

Cumulus convection causes vertical transport of tracer mass and therefore leads to a vertical redistribution of tracer concentrations. As single convective clouds cannot be resolved – even in a regional model with a relatively high resolution – a bulk formula for an ensemble of clouds in a grid box is applied. The different transport processes related to cumulus convection are taken into account: vertical transport inside the cloud, entrainment into the cloud and detrainment out of the cloud. Horizontally the grid box is divided into three areas: an area of cumulus updraft, an area of cumulus downdraft and an area of environmental air, where lifting and sinking of air of the first two areas are compensated (see Figure 2.4).

The term describing the change in tracer concentration due to cumulus convection in Equation 2.1 can be written in terms of vertical flux divergence:

$$\left(\frac{\partial C_\mathrm{i}}{\partial t}\right)_\mathrm{conv} = -\frac{1}{\overline{\rho}}\left(\frac{\partial F_\mathrm{i}^\mathrm{u}}{\partial z} + \frac{\partial F_\mathrm{i}^\mathrm{d}}{\partial z} + \frac{\partial F_\mathrm{i}^\mathrm{e}}{\partial z}\right) \quad (2.11)$$

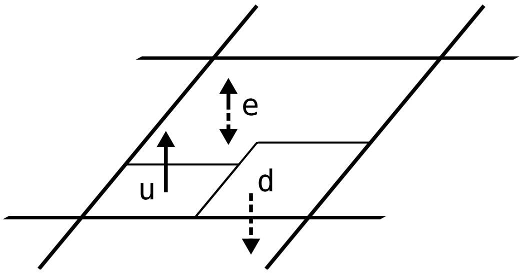

Figure 2.4: A grid box divided into areas of updraft, downdraft and compensating movement of the environment

where $\overline{\rho}$ denotes the mean density of air in the grid box. F_i^u, F_i^d and F_i^e denote the tracer mass flux in the updraft area of the grid box, in the downdraft area and in the area of environmental compensating movement, respectively. The vertical tracer flux in the updraft area is defined as

$$F_\mathrm{i}^\mathrm{u} = M^\mathrm{u} C_\mathrm{i}^\mathrm{u} \quad (2.12)$$

with the mass flux for air M^u (defined as positive for upward transport). The tracer mass fluxes for the downdraft area and for the environment are defined accordingly. The mass flux M^u in the updraft region is prescribed according to the convective cloud type. Three different convection types are distinguished: shallow convection, mid-level convection and deep convection (for details on the prescription of the mass fluxes see Tiedtke (1989)). The mass flux M^d in the downdraft region is calculated as a function of the mass flux in the updraft region M^u. Finally, the compensating mass flux in the environment M^e is defined as

$$M^\mathrm{e} = -(M^\mathrm{u} + M^\mathrm{d}) \quad (2.13)$$

assuring mass conservation.

During the convection process, entrainment and detrainment out of or into the area of vertical transport takes place. This can be caused by turbulent exchange of mass and organized inflow related to large scale convergence for updraft areas. For the downdraft area only organized outflow is assumed. The dominating process depends on the cloud type (for details refer to Tiedtke (1989)). Entrainment (E) and detrainment (D) lead to changes in the vertical tracer mass fluxes (except for the area of compensating vertical motion where no convective clouds are present):

$$\frac{\partial F_{\mathrm{i}}^{\mathrm{u}}}{\partial z} = E_{\mathrm{i}}^{\mathrm{u}} C_{\mathrm{i}}^{\mathrm{e}} - D_{\mathrm{i}}^{\mathrm{u}} C_{\mathrm{i}}^{\mathrm{u}} \tag{2.14}$$

$$\frac{\partial F_{\mathrm{i}}^{\mathrm{d}}}{\partial z} = E_{\mathrm{i}}^{\mathrm{d}} C_{\mathrm{i}}^{\mathrm{e}} - D_{\mathrm{i}}^{\mathrm{d}} C_{\mathrm{i}}^{\mathrm{d}} \tag{2.15}$$

$$\frac{\partial F_{\mathrm{i}}^{\mathrm{e}}}{\partial z} = \frac{\Delta \left(M^{\mathrm{e}} C_{\mathrm{i}}^{\mathrm{e}}\right)}{\Delta z} \tag{2.16}$$

The tracer mass fluxes are then used to calculate the tracer concentration tendency using a leap-frog scheme.

Brinkop and Sausen (1997) identified two main causes for possible negative tracer concentrations in the Tiedtke-scheme:

- the interpolation of tracer concentrations from full levels to half levels
- the calculation of tracer mass flux below the cloud base

Tracer concentrations – like the meteorological prognostic variables – are defined on full-levels, whereas the tracer mass fluxes are defined on half-levels, like the vertical velocities. (see Figure 2.2). In order to solve Equation 2.11 the flux divergences have to be computed. This is done iteratively starting at cloud base for the updraft area, then starting at the level of free sinking for the downdraft area, using a centered differences approximation. Finally the flux divergences in the environment are computed. Equations 2.14 - 2.16 are discretized as follows for a specific tracer (in the following, the lower index denotes the level on which the variable is defined):

$$\frac{\partial F^{\mathrm{u}}}{\partial z} = \frac{F_{\mathrm{k}-\frac{1}{2}}^{\mathrm{u}} - F_{\mathrm{k}+\frac{1}{2}}^{\mathrm{u}}}{\Delta z} = E_{\mathrm{k}+\frac{1}{2}}^{\mathrm{u}} C_{\mathrm{k}+\frac{1}{2}}^{\mathrm{e}} - D_{\mathrm{k}+\frac{1}{2}}^{\mathrm{u}} C_{\mathrm{k}+\frac{1}{2}}^{\mathrm{u}} \tag{2.17}$$

$$\frac{\partial F^{\mathrm{d}}}{\partial z} = \frac{F_{\mathrm{k}-\frac{1}{2}}^{\mathrm{d}} - F_{\mathrm{k}+\frac{1}{2}}^{\mathrm{d}}}{\Delta z} = E_{\mathrm{k}-\frac{1}{2}}^{\mathrm{d}} C_{\mathrm{k}-\frac{1}{2}}^{\mathrm{e}} - D_{\mathrm{k}-\frac{1}{2}}^{\mathrm{d}} C_{\mathrm{k}-\frac{1}{2}}^{\mathrm{d}} \tag{2.18}$$

$$\frac{\partial F^{\mathrm{e}}}{\partial z} = \frac{F_{\mathrm{k}-\frac{1}{2}}^{\mathrm{e}} - F_{\mathrm{k}+\frac{1}{2}}^{\mathrm{e}}}{\Delta z} = \frac{M_{\mathrm{k}-\frac{1}{2}}^{\mathrm{e}} C_{\mathrm{k}-\frac{1}{2}}^{\mathrm{e}} - M_{\mathrm{k}+\frac{1}{2}}^{\mathrm{e}} C_{\mathrm{k}+\frac{1}{2}}^{\mathrm{e}}}{\Delta z}. \tag{2.19}$$

From the flux divergence in the environment (Equation 2.19) it is easy to show how negative tracer concentrations can be produced by the centered differences-scheme: Assuming a non-zero downward mass flux in the environment ($M_{\mathrm{k}}^{\mathrm{e}} < 0 \ \forall \ k \in (k_{\mathrm{max}}, ..., 1)$), the tracer mass flux at level $k + \frac{1}{2}$ is given as:

$$F_{\mathrm{k}+\frac{1}{2}}^{\mathrm{e}} = M_{\mathrm{k}+\frac{1}{2}}^{\mathrm{e}} C_{\mathrm{k}+\frac{1}{2}}^{\mathrm{e}} = \frac{1}{2} M_{\mathrm{k}+\frac{1}{2}}^{\mathrm{e}} \left(\overline{C_{\mathrm{k}}} + \overline{C_{\mathrm{k}+1}}\right) \tag{2.20}$$

This tracer mass flux from layer k into layer $k+1$ depends partly on the tracer mass of layer $k+1$ where the flux is directed to. In Figure 2.5 a, the vertical flux discretization is depicted for this case: The tracer mass in the gray shaded area is transported downward by the tracer mass flux $F^{\mathrm{e}}_{\mathrm{k}+\frac{1}{2}}$. Negative tracer concentrations

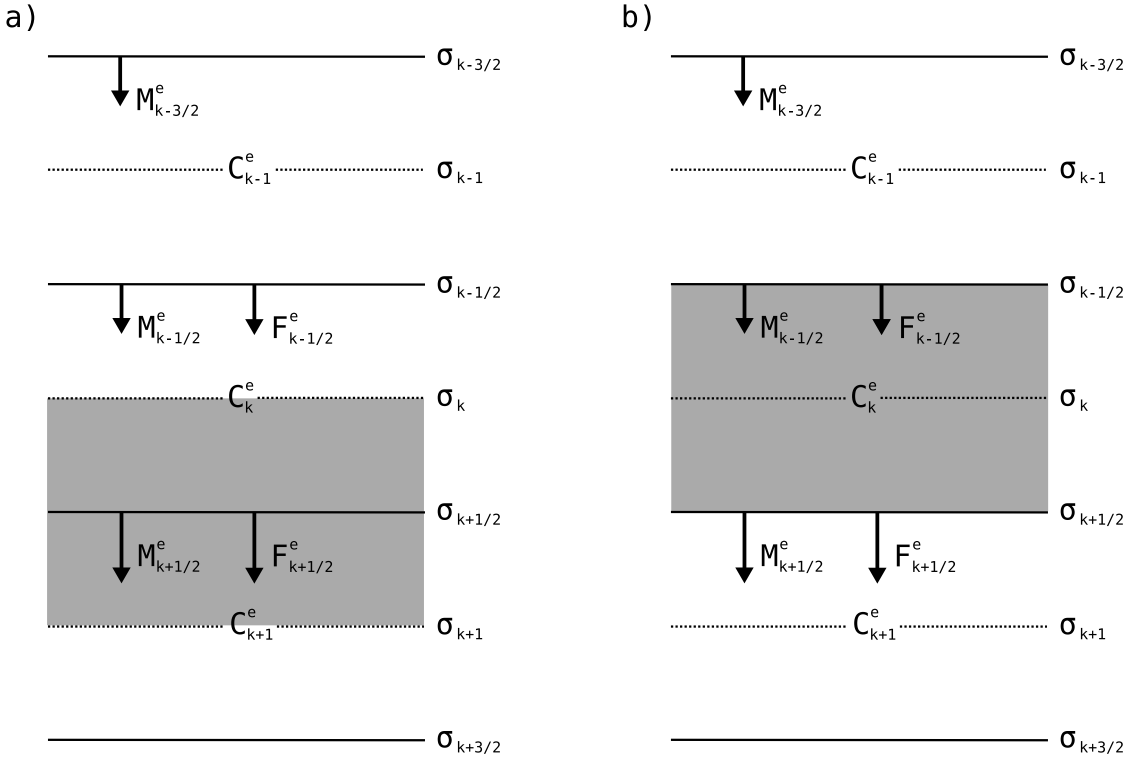

Figure 2.5: Vertical flux discretization. The vertical flux discretization in the environment (downward flux) is depicted for the standard convection scheme on the left hand side (a) and for the modified convection scheme on the right hand side (b). For details refer to the text.

follow from a situation where the tracer concentrations are zero in layer k and above ($k' \in (k, k-1, ..., 1)$). This leads to the tracer mass fluxes:

$$\begin{aligned} F^{\mathrm{e}}_{\mathrm{k}+\frac{1}{2}} &= \frac{1}{2} M^{\mathrm{e}}_{\mathrm{k}+\frac{1}{2}} \overline{C_{\mathrm{k}+1}} \\ F^{\mathrm{e}}_{\mathrm{k}-\frac{1}{2}} &= 0 \end{aligned} \tag{2.21}$$

Together with Equation 2.19 the divergence of the tracer mass flux in layer k is calculated as

$$\left(\frac{\partial F^{\mathrm{e}}}{\partial z}\right)_{\mathrm{k}} = -\frac{M^{\mathrm{e}}_{\mathrm{k}+\frac{1}{2}}\overline{C_{\mathrm{k}+1}}}{2\Delta z} > 0. \tag{2.22}$$

The positive tracer mass flux divergence (tracer mass flux out of the layer) from a layer with zero tracer mass leads to negative tracer concentrations in this layer.

To avoid this problem, Brinkop and Sausen (1997) proposed to use an upstream-scheme for convective tracer transport, where tracer concentrations are not interpolated to half-levels, but stay on the full-levels. Then Equation 2.20 becomes

$$F^{\mathrm{e}}_{\mathrm{k}+\frac{1}{2}} = M^{\mathrm{e}}_{\mathrm{k}+\frac{1}{2}}\overline{C_{\mathrm{k}}} \text{ for } M^{\mathrm{e}}_{\mathrm{k}+\frac{1}{2}} \leq 0 \tag{2.23}$$

$$F^{\mathrm{e}}_{\mathrm{k}+\frac{1}{2}} = M^{\mathrm{e}}_{\mathrm{k}+\frac{1}{2}}\overline{C_{\mathrm{k}+1}} \text{ for } M^{\mathrm{e}}_{\mathrm{k}+\frac{1}{2}} > 0 \tag{2.24}$$

where upward and downward mass fluxes in the environment have to be distinguished. Now the downward tracer mass flux in the environment depends only on the tracer concentrations in the layer above the sigma-level where the flux is defined on. This is the gray shaded area in Figure 2.5 b for the downward mass flux $F^{\mathrm{e}}_{\mathrm{k}+\frac{1}{2}}$, which corresponds to Equation 2.23. Using the new scheme, negative tracer concentrations in the example shown above are avoided as the flux divergence in layer k becomes zero:

$$\left(\frac{\partial F^{\mathrm{e}}}{\partial z}\right)_{\mathrm{k}} = \frac{M^{\mathrm{e}}_{\mathrm{k}-\frac{1}{2}}\overline{C_{\mathrm{k}-1}} - M^{\mathrm{e}}_{\mathrm{k}+\frac{1}{2}}\overline{C_{\mathrm{k}}}}{\Delta z} = 0. \tag{2.25}$$

The case for upward mass flux is treated similarly.

The second source of potential negative tracer concentrations is the calculation of the tracer mass flux below the cloud. In the convection scheme of Tiedtke the tracer mass flux below cloud base is independent of the actual tracer concentration. The tracer mass flux at cloud base F_{cb} decreases linearly to zero at the surface. This results in positive tracer mass flux divergences below the cloud for the case of a non-zero updraft tracer mass flux at cloud base $F^{\mathrm{u}}_{\mathrm{cb}} > 0$. For low tracer concentrations, this could potentially result in negative tracer values.

In the modified scheme, mass fluxes M instead of tracer mass fluxes F decrease linearly with height starting at the cloud base to zero mass flux at the surface. Now at low tracer concentrations also the tracer mass flux is decreased accordingly.

In spite of the modifications, negative tracer concentrations can occur due to a too large timestep. As a solution for these cases, a security check is proposed in which the total tracer mass flux is artificially reduced in the column by a factor γ ($0 \leq \gamma \leq 1$) if negative tracer concentrations occur. For further details about the numerical scheme, refer to Tiedtke (1989) and Brinkop and Sausen (1997).

Comparison Between the Standard and the Modified Convection Scheme

In order to compare the convection scheme of Tiedtke with the modified convection scheme, I performed a REMO simulation using artificial passive tracers in a region where strong convective transport occurs. All transport processes for the passive tracers other than the convection are turned off in order not to overlay the effect of the modifications in the convection scheme on the tracer distribution. The simulation time was 20 hours with a timestep of 240 s. Results for the standard Tiedtke scheme and for the modified convection for one grid box are shown in Figure 2.6.

The simulation starts for both convection schemes with an artificial tracer profile, which decreases with height (solid black line in the lower left panel of Figure 2.6). In both convection schemes, tracer mass is transported from near ground layers to upper layers of the model atmosphere, shown in the upper panels of Figure 2.6. While the passive tracer is vertically uniformly distributed from the ground to the upper layers in the modified convection scheme case after about 200 timesteps, an unrealistic oscillatory pattern starts developing in the standard Tiedtke scheme case after a few timesteps. Looking at the evolution of the tracer concentration with time in two distinct layers 17 and 16 (corresponding to about 450 hPa and 410 hPa, respectively) (lower right panel of Figure 2.6), the oscillation in the standard convection case is clearly visible. Tracer concentrations oscillate about a central value which seem to be the tracer concentrations of the modified convection case. During this relatively short simulation the amplitude of the oscillation increases with time. Tracer concentrations of 0 ppmv are reached and negative tracer concentrations are only avoided by using a mass fixer which shifts negative concentrations to lower model layers. It ultimately creates tracer mass in the lowest model layer by setting negative tracer concentrations to zero. This is avoided using the modified convection scheme. The vertical profiles of the last simulated timestep is shown in the lower left panel of Figure 2.6. Again an oscillation (this time with height) is apparent in the standard convection scheme with the tracer concentration of the modified scheme as central value.

The results show that the modification of the Tiedtke convection scheme after

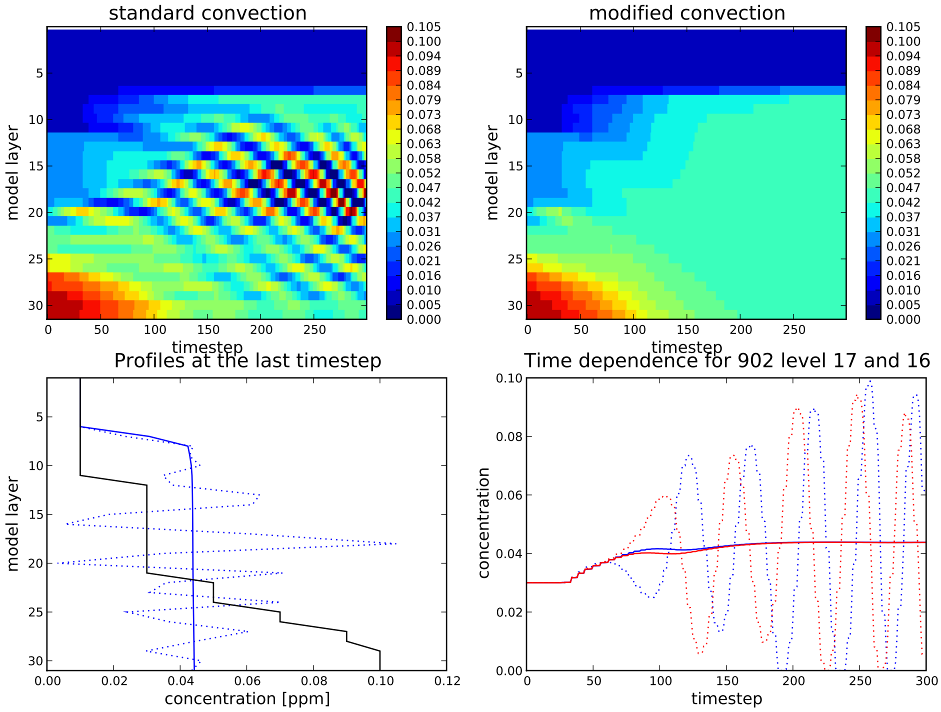

Figure 2.6: Comparison between the Tiedtke and the modified convection scheme. The upper left panel shows the time evolution of a passive tracer with time. The upper right panel shows the time evolution of a passive tracer using the modified convection scheme. The lower left panel shows the initial profile of the passive tracer (solid black line) and the two profiles of the last timestep of the simulation: the profile of the standard convection scheme (dotted blue line) and the profile of the modified convection scheme (solid blue line). In the lower right panel, the time evolution is depicted for the model levels 17 (blue lines) and 16 (red lines). The dotted lines correspond to the standard convection, whereas the solid lines correspond to the modified convection scheme.

Brinkop and Sausen (1997) lead to more realistic tracer profiles and to a more realistic evolution of the tracer concentration with time. Oscillation in tracer concentration together with negative tracer concentration values are avoided. Although in a normal model simulation including all processes, the oscillation of tracer concentration can be overlain by other processes (e.g., advection, chemical reactions, deposition), in some grid boxes with strong convection the oscillation can lead to an artificial creation of tracer mass. For specific humidity, which is convected using the standard Tiedtke convection scheme, a similar effect is not apparent. This might be due to the greater abundance of specific humidity in the atmosphere and condensation processes which can compensate low specific humidity values. For future studies, I recommend to implement the modified convection scheme also for specific humidity. Throughout this study the modified convection scheme is used to convect tracer mass.

3 Modelling Climate in South America

As described in Chapter 1, meteorological conditions are crucial for many chemical processes. A prerequisite for the correct simulation of trace gas concentrations is the realistic representation of the meteorological conditions in the region of interest. In this chapter, the ability of REMO to simulate South American climate is investigated. In order to realistically simulate the climate in South America in the period between 1958 and 2000, ERA-40 (Uppala et al., 2005) reanalysis data is used as boundary conditions. The simulation over a time period in the past is called *hindcast*. Simulated temperature and precipitation are compared with measurements for the reference period of 1961-1990. The simulation of meteorology together with chemical processes is described in Chapter 4 and in Chapter 5. An overview of the meteorological conditions in South America is given in Section 1.2.

3.1 Simulation Setup

In order to perform the hindcast of the ERA-40 period the regional climate model REMO 5.7 is used in its standard version which does not include chemistry and tracer transport. The model is initialized on the 1st of January 1958 at 0h. Prognostic atmospheric fields such as temperature, humidity, horizontal wind components and surface pressure are interpolated from the ERA-40 large-scale forcing onto the REMO model domain. The model is run in the so-called *climate mode*: After the initialization of the model in the first timestep, meteorological conditions of the driving data are only interpolated to the REMO model domain in the lateral boundary zone of about eight gridboxes. In this so-called *sponge zone*, meteorological information of the driving model decreases exponentially towards the model domain center. Using this method the large scale flow outside the model domain is taken into account in the interior of the model domain as described in Chapter 2. The model simulation ends on the 31st of December 2000.

The model domain comprising the whole South American continent and parts of the south Atlantic and south Pacific is shown in Figure 1.1 on the rotated spherical grid as it is used in the model simulations. It consists of 121 × 145 gridboxes and has a horizontal resolution of $^1/_2{}^\circ$ (ca. 55 km). The model domain interpolated on a global regular grid is depicted in Figure 3.1. Note that the corners of the model domain are cut of slightly.

Major orographic features like the Andes range, the Amazon basin and the Brazilian highlands, which are influencing meteorological conditions in South America are represented in the model domain (cf. Figure 3.1). The highest peak of the Andes mountain range is the Cerro Aconcagua with a hight of 6962 m, which is located in Argentina. The highest elevation in the Andes range in the model domain is 4952 m for a $50 \times 50\,\mathrm{km}^2$ gridbox. The impact of the Andes mountain range and the Amazon basin on circulation and precipitation and temperature patterns is described in Section 1.2.

3.2 Results and Evaluation

In order to assess the ability of REMO to reproduce South American climate conditions described in Section 1.2, temperature and precipitation patterns are compared with observation data. Global gridded precipitation and temperature data from the Climatic Research Unit (CRU) is used. The dataset in version 2.1 is referred to in the following as *CRU TS 2.1* (Mitchell and Jones, 2005). Observation data is interpolated from the original global $^1/_2{}^\circ$ grid onto the rotated $^1/_2{}^\circ$ grid of the REMO model domain used in this study. Temperature values correspond to a certain height in CRU TS 2.1 as well as in REMO. The different orography of the observation data and of REMO would lead to temperature differences due to the non-zero atmospheric temperature lapse rate. To take the differences in the orography into account, CRU TS 2.1 is vertically interpolated using a lapse rate of 6.5 K/ km. CRU TS 2.1 observation data is only available for land gridboxes. For clarity reasons, ocean gridboxes are masked out in the plots of simulated REMO values.

Temperature and Precipitation Patterns in the Time Period 1961 to 1990

In Figure 3.2 the mean temperature pattern in the REMO model domain is depicted for the time period between 1961 and 1990 for observed CRU TS 2.1 data and simulated REMO data.

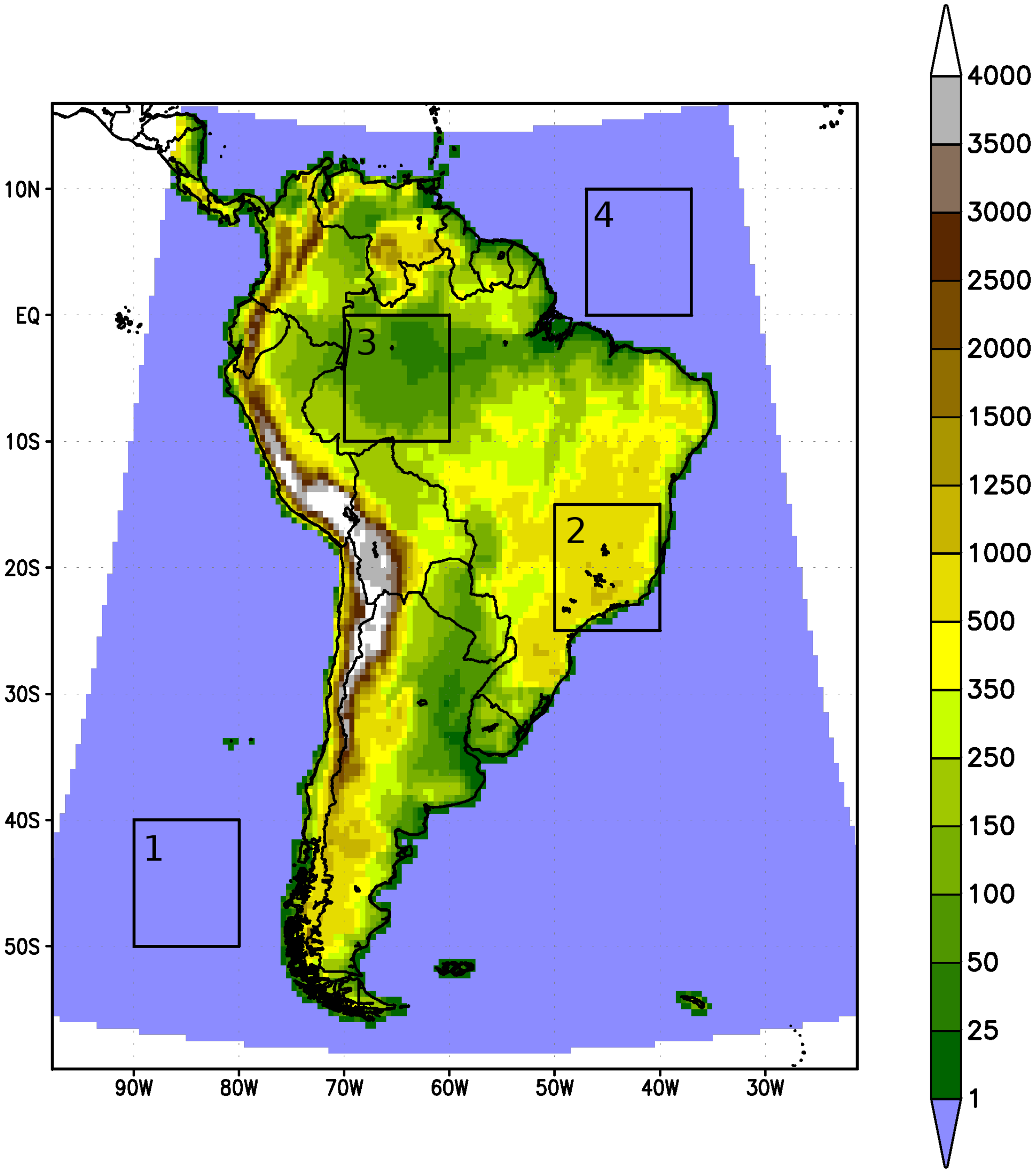

Figure 3.1: Orography of South America. The orography of South America as it is represented in REMO is plotted in [m]. The model domain is interpolated to a regular $1/2\,^\circ$ x $1/2\,^\circ$ grid. Their corners are cut at the edges of the plot. Black rectangles correspond to different regions of interest which are referred to in this chapter and in Chapter 4: 1: *South Pacific*, 2: *Brazilian Highlands*, 3: *Amazon Basin*, 4: *Atlantic (north)*.

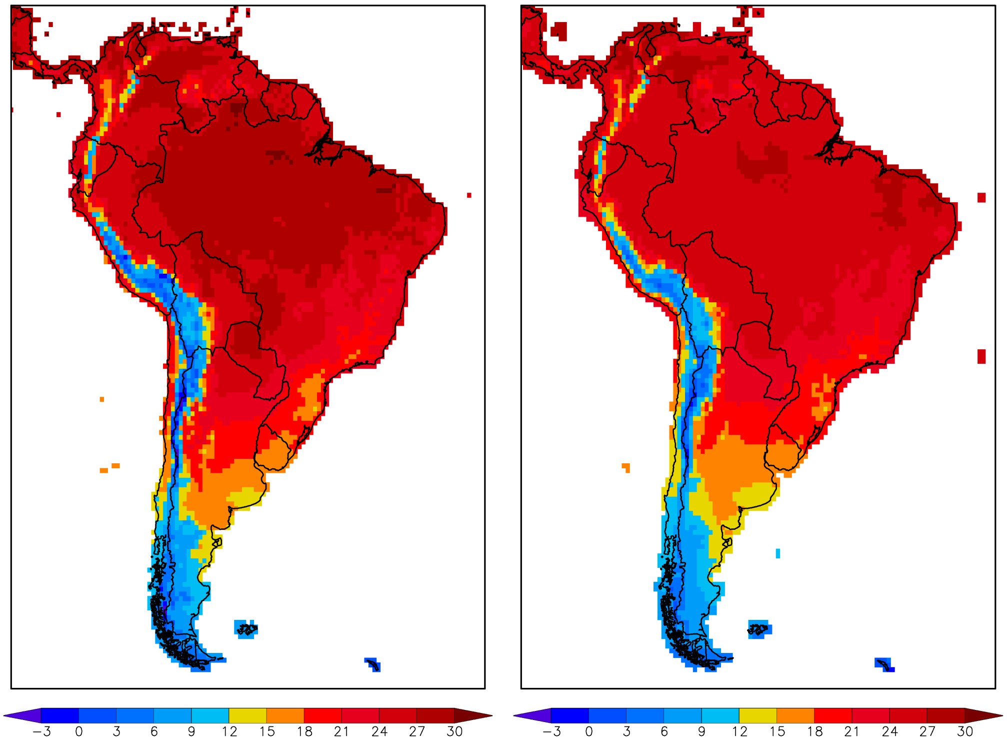

Figure 3.2: Mean 2m-temperature for 1961-1990 in [° C] The mean 2m-temperature is plotted for simulated REMO data and CRU TS 2.1 data on the left and on the right hand side, respectively.

In the northern part of the Andes mountain range in Colombia and Ecuador, 2m-temperature simulated by REMO range mainly between 9° C and 15° C. Further south in the Andes range, temperatures are slightly lower between about 0° C and 9° C. In some gridboxes along the Andes range mean temperatures below 0° C can be found. In great parts of the Amazon basin a mean temperature between 27° C and 30° C is simulated. Along the Brazilian coast, where the megacities São Paulo and Rio de Janeiro are located, temperatures range between 15° C and 21° C. The temperature belt of 15° C to 18° C is located around Buenos Aires and the Rio de la Plata, while in Patagonia the temperatures range mainly between 6° C and 12° C.

Gridded observation data CRU TS 2.1 shows temperatures lying mainly between 0° C and 12° C along the whole Andes range, with temperatures exceeding 12° C in the northern part of the Andes in northern Peru, Ecuador and Colombia. A small part of the Amazon region shows mean temperatures between 27° C and 30° C. In the rest of the Amazon region mean temperatures between 24° C and 27° C can be found. Close to the megacities of São Paulo and Rio de Janeiro along the Brazilian coast, temperatures vary between 15° C and 21° C. In CRU TS 2.1 the temperature belt of 15° C to 18° C covers southern Uruguay and Buenos Aires as well as large parts of central Argentina. In major parts of southern Chile and Patagonia, temperatures range between 6° C and 12° C.

Multi-annual mean precipitation of the time period from 1961 to 1990 is shown in Figure 3.3 for simulated REMO results and CRU TS 2.1.

In the northern part of the Andes range in Colombia and Ecuador, precipitation exceeds 500 mm/month in simulated REMO data. While the precipitation can exceed 400 mm/month in the Andes at upper altitudes in Peru and Bolivia, the coastal region of Peru and Chile shows precipitation rates of less than 25 mm/month. In the southern part of Chile (south of 30° S) higher precipitation rates are simulated. They increase to about 450 mm/month in southern Chile. On the eastern side of the Andes range at the same latitude, in Patagonia, precipitation rates are mainly below 50 mm/month. In the region around Buenos Aires precipitation range between 75 mm/month and 100 mm/month. In the coastal region around São Paulo, precipitation rates of between 100 mm/month and 200 mm/month are simulated. Great parts of the Amazon show precipitation rates between 150 mm/month and 250 mm/month, while in the Nordeste region, precipitation rates are partly between 25 mm/month and 50 mm/month.

The gridded observations CRU TS 2.1 in Figure 3.3 show precipitation rates around

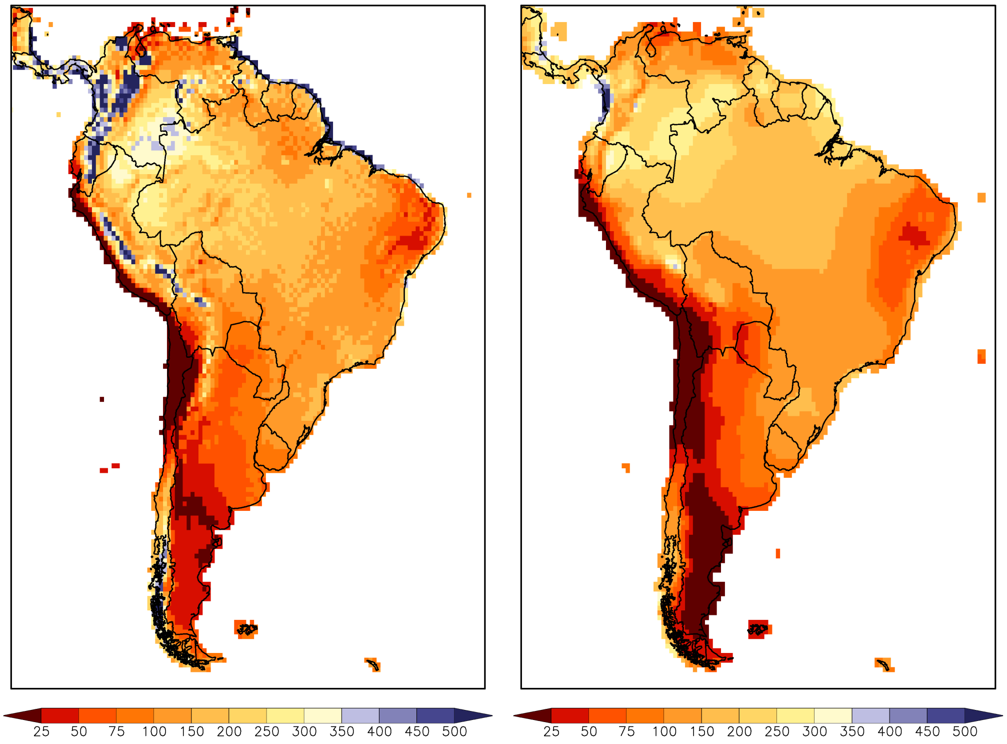

Figure 3.3: Mean precipitation for 1961-1990 in [mm/month] The mean precipitation is plotted for simulated REMO data and CRU TS 2.1 data on the left and on the right hand side, respectively.

100 mm/month. Precipitation rates above 500 mm/month are only observed in this region at the western coast of Colombia. The coastal regions of Peru and northern Chile show precipitation rates of below 25 mm/month, while precipitation rates increase to about 150 mm/month to 200 mm/month further south in southern Chile. In the western part of Patagonia precipitation rates are mainly below 25 mm/month. While precipitation in the La Plata region around Buenos Aires is between 75 mm/month and 100 mm/month, the region around São Paulo is characterized by precipitation between 100 mm/month and 150 mm/month. In great parts of the Amazon, precipitation rates are between 150 mm/month and 250 mm/month. The Nordeste region shows precipitation rates mainly between 25 mm/month and 75 mm/month in CRU TS 2.1.

Comparing the multi-annual mean of 2m-temperature between 1961 and 1990 of simulated REMO values and CRU TS 2.1 (cf. Figure 3.2) a general agreement of the main patterns can be observed. This is also the case for the main pattern in multi-annual mean of precipitation (cf. Figure 3.3) in simulated REMO values and CRU TS 2.1. Nevertheless, also differences between the two datasets can be observed.

Relatively cold temperatures – mainly between -3° C and 12° C – are present in higher altitudes of the Andes mountains in simulated REMO values as well as in CRU TS 2.1 along the whole cordillera. Compared to CRU TS 2.1, REMO temperatures are about 2° C lower in the Andes mountain range. Precipitation exceeds 500 mm/month in REMO data in several regions along the Andes mountain range north of central Bolivia while it stays mainly below 150 mm/month in CRU TS 2.1.

In the coastal region of Peru and Chile, temperature values are partly more than 5° C higher in REMO than in CRU TS 2.1. Mean precipitation values are below 25 mm/month and the difference between REMO values and CRU TS 2.1 is mainly below 10 mm/month. South of about Santiago de Chile, the positive temperature bias between REMO and CRU TS 2.1 decreases to below 2° C. Precipitation is higher in REMO than in CRU TS 2.1, with a relative bias of partly more than 200 % in the southernmost part of South America in the Tierra del Fuego.

In eastern Patagonia multi-annual mean temperature of REMO and CRU TS 2.1 agree mainly within a range of ±0.5° C. Precipitation, being below 50 mm/month in simulated REMO values and below 25 mm/month for CRU TS 2.1, are mainly less than 25 mm/month higher in REMO than in CRU TS 2.1.

North of Patagonia up to southern Brazil, precipitation is slightly higher in CRU TS 2.1 than in REMO with differences of mainly less than 25 %. Temperature bands are slightly shifted to the south in REMO compared to CRU TS 2.1, leading to a positive bias in REMO of up to 2° C.

In the coastal region of southern Brazil and in the Brazilian highlands, REMO and CRU TS 2.1 temperatures agree rather well with higher values in CRU TS 2.1 in some small areas and differences of mainly below 1° C. While the difference in precipitation is mainly below about 10 % in coastal areas of southern Brazil, the Brazilian highlands show a positive bias in REMO compared to CRU TS 2.1 of up to about 50 %.

In the Amazon region and in some parts of the Nordeste, temperatures are up to about 3° C higher in REMO than in CRU TS 2.1 with smaller differences in the Nordeste. Precipitation in the Nordeste is rather low with values of mainly less than 75 mm/month. Absolute values of the differences between REMO and CRU TS 2.1 in this region are mainly below 25 mm/month. Precipitation differences in the Amazon are ambiguous: In the northern part of the Amazon, CRU TS 2.1 exceeds REMO values by up to about 50 %, while in the southern and western part of the Amazon, REMO values are higher than CRU TS 2.1 by about the same amount.

Yearly Cycle of Temperature and Precipitation in the Time Period 1961 to 1990

In order to investigate the annual behavior of temperature and precipitation, the multiannual mean of the yearly cycle for temperature and precipitation between 1961 and 1990 are investigated.

In Figure 3.4 the yearly cycle of temperature is plotted for region 2 (Brazilian Highlands) and region 3 (Amazon Basin) depicted in Figure 3.1. The temperature in the Amazon basin as represented in CRU TS 2.1 ranges between 25.5° C and 27° C with minimum temperature in June. Temperature simulated by REMO ranges below 27.5° C in the first half of the year and also shows a minimum in June with about 25.7° C. In the second half of the year, multi-annual monthly mean temperatures rise up to 31.5° C in September.

In the Brazilian highlands the seasonal cycle shows a maximum for CRU TS 2.1 in February at about 24.5° C and a minimum in July at about 19° C. Simulated temperatures by REMO show a maximum at a temperature of about 23.5° C in

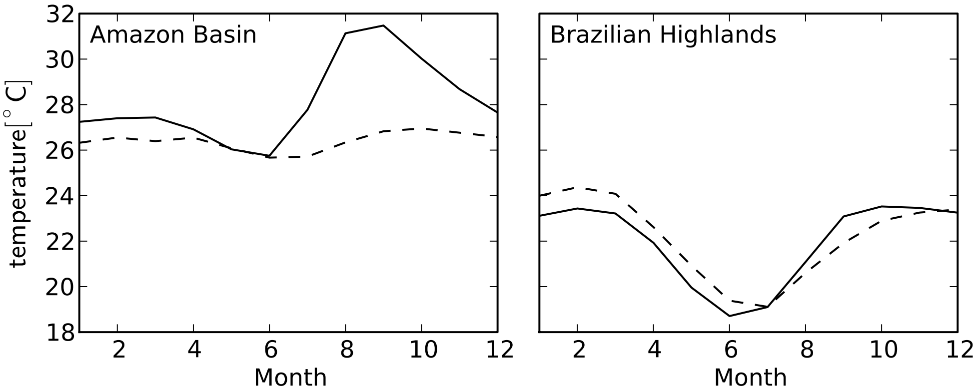

Figure 3.4: Yearly cycle of temperature for 1961-1990 in [° C] The yearly cycle of monthly mean temperature is plotted for simulated REMO data (solid line) and CRU TS 2.1 data (dashed line).

February as well as in October. The simulated yearly minimum is located in June at about 18.7° C.

Multi-annual monthly mean precipitation is depicted in Figure 3.5. The yearly cycle of CRU TS 2.1 shows a maximum of 290 mm/month in March and a minimum of about 100 mm/month in August for the Amazon basin. Simulated REMO precipitation ranges between 375 mm/month in April to about 50 mm/month in July.

In the Brazilian highlands region, maximum precipitation of 240 mm/month can be observed in CRU TS 2.1 in December, while the minimum is located between 24 mm/month and 26 mm/month from June to August. In the latter time period, simulated precipitation by REMO ranges at a minimum between about 17 mm/month and 21 mm/month.

The yearly cycle of the monthly mean temperature in the Brazilian highlands shows a positive bias of CRU TS 2.1 in the first half of the year and a negative bias of CRU TS 2.1 in the second half of the year of less than about 1° C compared to simulated REMO temperatures. This is also the case for the first half of the year in the Amazon basin region. In the second half of the year, a positive bias of REMO in comparison with CRU TS 2.1 of up to around 5° C is observed in late southern hemisphere winter and early spring. A similar bias was observed by Silvestri et al. (2009) when

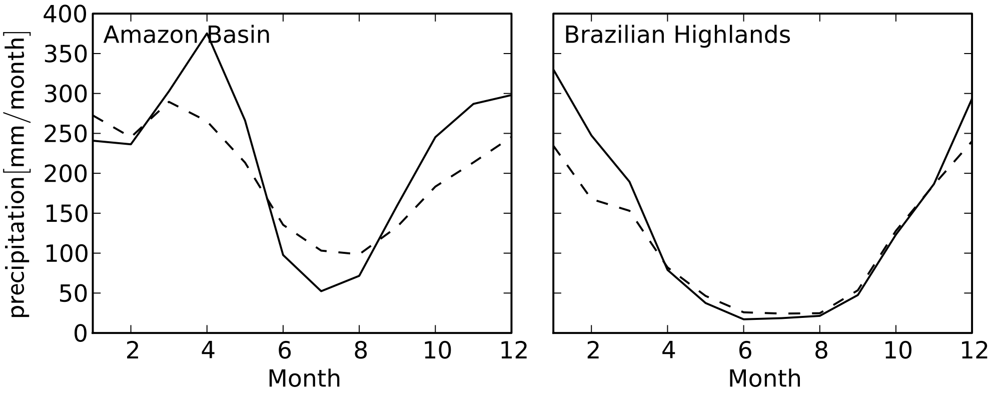

Figure 3.5: Yearly cycle of precipitation for 1961-1990 in [mm/month] The yearly cycle of precipitation is plotted for simulated REMO data and CRU TS 2.1 data solid black line and dashed line, respectively.

comparing simulated REMO temperatures with station data and ERA 40.

The yearly cycle of precipitation is similar in CRU TS 2.1 and in simulated REMO values in the Amazon basin and in the Brazilian highlands. Peak precipitation can be found in southern hemisphere autumn, while the dry season with a minimum in precipitation is located in winter in the Amazon basin. In the Brazilian highlands, peak precipitation is observed in southern hemisphere summer in both datasets, while the dry season is located around winter. Nevertheless, precipitation is overestimated in REMO by about 40 % in autumn compared to CRU TS 2.1, while it is underestimated in winter by up to 50 % in the Amazon basin region. In the Brazilian highlands, REMO overestimates precipitation compared to CRU TS 2.1 in summer, while absolute biases are below 10 mm/month during most of the rest of the year.

3.3 Discussion

A strong dry bias in the northern Amazon region in REMO compared to CRU TS 2.1 is observed in the horizontal patterns as well as in the multi-annual yearly cycle. It can be the result of relatively dry driving data in the Amazon region in the time period considered: Betts et al. (2005) observed a dry bias in the ERA-40 data compared to measurements, e.g., for the time periods 1958-1972 and 1973-1978. The resulting relatively dry soil might lead to a reduced evapotranspiration and in consequence to the relatively high temperatures in REMO in comparison with CRU TS 2.1. They are most pronounced in late summer, begin of autumn in the Amazon basin region. Larger differences in the coastal region of Peru and Chile can probably be related to a deficiency of the REMO model to represent marine stratocumulus clouds as it is observed in other climate models, e.g., by Collins et al. (2006).

The high precipitation values in the northern Andes range might result from orographic precipitation which is represented in REMO, but which is not well represented in CRU TS 2.1. Precipitation in this region is probably underestimated in CRU TS 2.1, due to a relatively low number of station data at higher altitudes in South America. The number of station data in South America is relatively low, compared to other continents (cf. Mitchell and Jones, 2005). Underestimation of orographic precipitation in CRU data is also observed in other studies when comparing with regional climate model data (e.g., Achberger et al., 2003) or when comparing with higher resolution precipitation measurement datasets (e.g., Frei and Schär, 1998; Suprit and Shankar, 2008).

3.4 Conclusions

Altogether both multi-annual mean datasets CRU TS 2.1 and REMO values agree reasonably well. This is especially the case in regions around the megacities of São Paulo and Buenos Aires, where the main focus of this study lies. A more detailed analysis of the REMO hindcast used in this study is done by Silvestri et al. (2009). They analyze the seasonal cycles of precipitation, temperature and surface pressure in different regions of South America including the main circulation patterns. They conclude that the model is able to reproduce the basic structure of the low-level circulation only with some deficiencies in reproducing the South American low-level jet structure. The simulation also enhances the global reanalysis in precipitation and temperature in some regions.

The simulation of realistic meteorological conditions is a prerequisite for simulating realistic trace species concentrations. This chapter shows that REMO is able to realistically simulate South American climate conditions. In the following chapters, REMO is used together with online chemistry and tracer transport to simulate trace gas concentrations in South America.

4 Modelling Air Pollution in South America

Vegetation fires and anthropogenic emissions are the main emission sources with an impact on the regional air quality in South America, as already described in Section 1.3. While the fire emissions show a high seasonality with peak emissions during the southern hemispheric dry season (about August, September, October) (e.g., Generoso et al., 2003), the emissions emanating from megacities are rather constant throughout the year. One of the goals of this study is to quantify the impacts of the different emission sources – megacity emissions and biomass burning emissions – on the regional air quality. For this purpose the regional climate model REMO including chemistry and tracer transport – described in Chapter 2 – is used to simulate South American climate together with tracer concentrations.

In this chapter the so-called *reference run* ($\mathrm{R}_{\mathrm{reference}}$) for trace gases is described. It simulates present day climate and tracer concentrations. In Chapter 5 the tracer concentrations of the reference run are compared to scenario runs with modified emission fields to quantify the impact of the different emission sources.

The year 2000 considered in this study is a year with relatively low fire emissions from South America (e.g., Edwards et al., 2006; Schultz et al., 2008b). The simulation therefore provides an upper estimate of the relative importance of megacity emissions compared to the impact of fire emissions on the regional air quality.

In order to evaluate the quality of the model results, tracer concentrations are compared to in situ measurement data and satellite retrievals in the subsequent section. Tracer profiles from the INCA (*INterhemispheric differences in Cirrus properties from Anthropogenic emissions*) campaign are used as well as CO total column data from the MOPITT (*Measurements Of Pollution In The Troposphere*) sensor on board the TERRA satellite.

4.1 Simulation Setup

The period of the reference model simulation $R_{\text{reference}}$ including chemistry and tracer transport extends from January to November 2000. It is part of the long term climate simulation of the ERA-40 period $R_{\text{ERA 40}}$ described in Chapter 3 which comprises the years 1959 to 2000. Chemistry and tracer transport is calculated over the whole domain shown in Figure 3.1.

The meteorology of $R_{\text{reference}}$ is exactly the same as the meteorology of $R_{\text{ERA 40}}$ in the corresponding time period. This is realized by continuously calculating the meteorological fields, using the output of the last hour of December 1999 of $R_{\text{ERA 40}}$ as input (restart files) for $R_{\text{reference}}$. As shown in Figure 2.3, the chemical mechanisms and the tracer transport do not influence the meteorological fields in this model setup. The main advantage of this model setup is that for different emission scenarios, changes in tracer concentrations can be attributed directly to the emission changes and are not influenced by a different meteorological situation. The disadvantage is that feedback processes of the chemistry onto the meteorology cannot be taken into account. Examples of such feedback processes would be cloud formation due to aerosols or changes in the incoming solar radiation due to changes in stratospheric ozone concentrations. As the focus of this study lies in tropospheric air pollution, it is reasonable to neglect these feedback processes in a first approximation.

To take into account the spin-up time of the chemical mechanisms and the tracer transport, the first 15 days of January 2000 are not considered throughout this study.

Boundary Data

The chemical boundary data is important for taking into account tracer sources outside the model domain. In this study the most important influence on tracer concentrations from outside the model domain originates from Africa and is thus expected to enter the model domain at their northeastern border.

The treatment of the boundary data is described in Section 2.2.2. The data used in this study originates from a global chemical transport model MOZART-4 run at T42 resolution (this corresponds to a $2.8° \times 2.8°$ grid resolution). It is driven by NCEP (National Centers for Environmental Prediction) reanalysis data. Emissions used for calculating the boundary data are based on the POET[1] emission inventory including natural and anthropogenic sources. POET emission data is aggregated on a 1° x 1° grid.

Emission Data

The emission data used in the REMO simulations is aggregated from different emission databases. Anthropogenic emissions and fire emissions are mainly taken from the RETRO[2] (REanalysis of the TROpospheric chemical composition over the past 40 years) version 2 database (Schultz et al., 2008a). The RETRO database uses a 0.5° x 0.5° grid, which is the same resolution used in the simulations throughout this study. The RETRO emissions are provided in a monthly time resolution.

Emitted species not included in RETRO are taken from other emission databases. Anthropogenic and volcanic emissions of SO_2 and SO_4 are taken from the AEROCOM emission database (Dentener et al., 2006), which is aggregated on a 1° x 1° grid using a yearly time resolution. 2.5 % of SO_2 is emitted as primary SO_4.

Biogenic emissions (NO_x, acetaldehyde, formaldehyde, ethene, acetone and isoprene) are taken from the global dynamic vegetation model ORCHIDEE (ORganizing Carbon and Hydrology In Dynamic EcosystEms) (Lathière et al., 2006). They are provided on a 1° x 1° grid. In this study a climatology of monthly mean values is used, which is calculated using emissions of the years 1983 to 1995.

Ammonia (NH_3) emission estimates from agricultural sources like synthetic fertilizers or animal manure are taken from Bouwman et al. (2002). Yearly mean values are provided for the year 1995 with a horizontal resolution of 0.5° x 0.5°.

All emission data is aggregated and interpolated onto the rotated half-degree grid of the model domain used in this study. As an example, total emissions of CO as used in this study are plotted in Figure 4.1 for the month of April and October.

In April, CO emissions in South America are mainly below 20 Gg/(yr · gridbox). At some isolated locations, mainly in coastal areas, emission surpass 100 Gg/(yr · gridbox). In October, large parts of the Amazon, Bolivia and Paraguay are covered by CO emissions of more than 500 Gg/(yr · gridbox). In most coastal areas, similar patterns

---

[1] Granier, C., J.F. Lamarque, A. Mieville, J.F. Muller, J. Olivier, J. Orlando, J. Peters, G. Petron, G. Tyndall, S. Wallens, POET, a database of surface emissions of ozone precursors, available on internet at http://www.aero.jussieu.fr/projet/ACCENT/POET.php , 2005.

[2] http://retro.enes.org

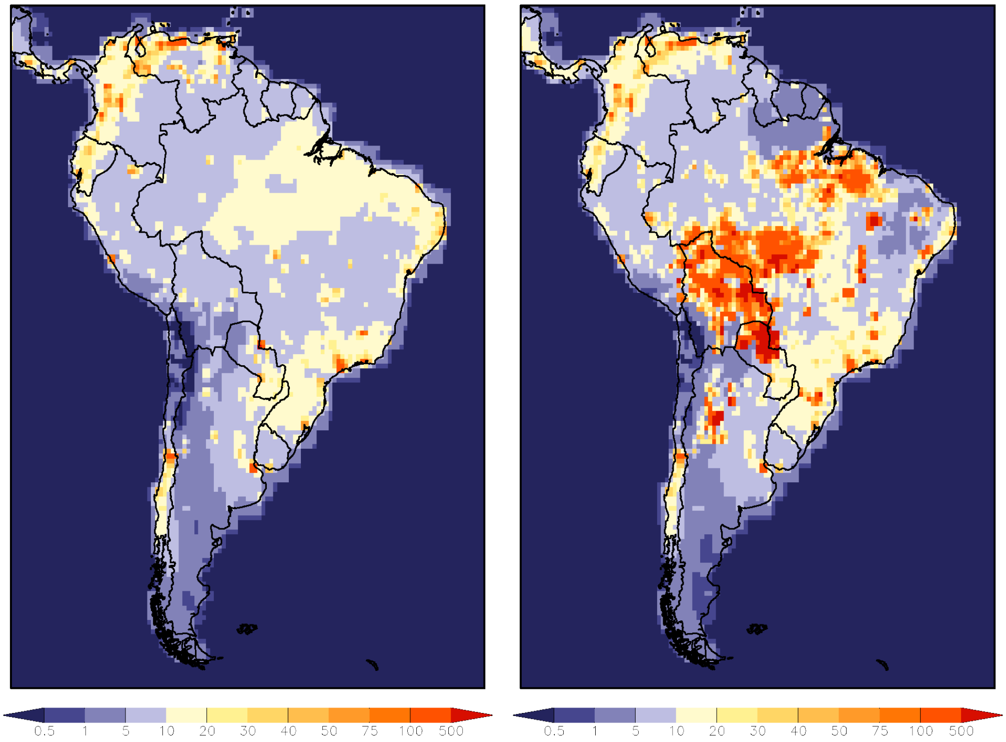

Figure 4.1: Monthly mean CO emissions for April and October 2000. The total CO emissions are plotted in [Gg/(yr · gridbox)] for April and October 2000 on the left and on the right hand side, respectively. For details refer to the text.

as in April can be observed.

While emissions from megacities stand out in the emission plot for April, biomass burning emissions dominate overall emissions in October during the biomass burning season. The latter are mainly confined to the Amazon and extend towards the south-west, covering parts of Bolivia and northern Paraguay. Away from the area of biomass burning, e.g., near Buenos Aires, emission patterns are similar in April and October. This is an indication for anthropogenic emissions related to fossil fuel combustion originating from industry and car traffic. As an example, CO emission are shown seperately for anthropogenic sources and for biomass burning for October 2000 in Figure 1.3.

Photolysis Rates

In the frame of this study, a preprocessor for the photolysis rates is created, based on the TUV Radiation Model (version 4.4) (Madronich and Flocke, 1999) as described in Chapter 2. Photolysis rates are tabulated for the 21 photolysis reactions included in the RADM2 chemical mechanism. They are calculated for five different altitudes ($0, 1, 4, 7$ and $10\,\mathrm{km}$), for eleven hours of deviation from the local noon (therefore for eleven different solar zenith angles) and for each of the eleven months simulated in this study. They are located at latitudes with 10° spacing.

Photolysis rates $J_{\mathrm{NO_2}}$ (Reaction 2.8) are depicted in Figure 4.2 for the 15th of January as an example.

$$\mathrm{NO_2} + h\nu \longrightarrow \mathrm{NO} + \mathrm{O}(^3\mathrm{P}) \tag{2.8}$$

At the surface at 15 h (left panel in Figure 4.2), lowest photolysis rates $J_{\mathrm{NO_2}}$ are $7.7\times10^{-3}\,\mathrm{s^{-1}}$ and $6.1\times10^{-3}\,\mathrm{s^{-1}}$ at -60° and 20° latitude, respectively. Photolysis rates $J_{\mathrm{NO_2}}$ increase with height up to a maximum of $13.9\times10^{-3}\,\mathrm{s^{-1}}$ at about -30° latitude and 10 km altitude. At a fixed latitude of -40° (right panel in Figure 4.2) near surface $J_{\mathrm{NO_2}}$ values range from $10.1\times10^{-3}\,\mathrm{s^{-1}}$ at local noon to $0\,\mathrm{s^{-1}}$ after sunset at about 20 h. At 10 km altitude $J_{\mathrm{NO_2}}$ decrease from $14.5\times10^{-3}\,\mathrm{s^{-1}}$ to $0\,\mathrm{s^{-1}}$ from local noon to sunset.

$J_{\mathrm{NO_2}}$ is increasing with height due to the actinic flux, which is increasing with altitude as less molecules from above absorb the incoming radiation of wavelengths important for $J_{\mathrm{NO_2}}$. This means the optical depth decreases for wavelengths on

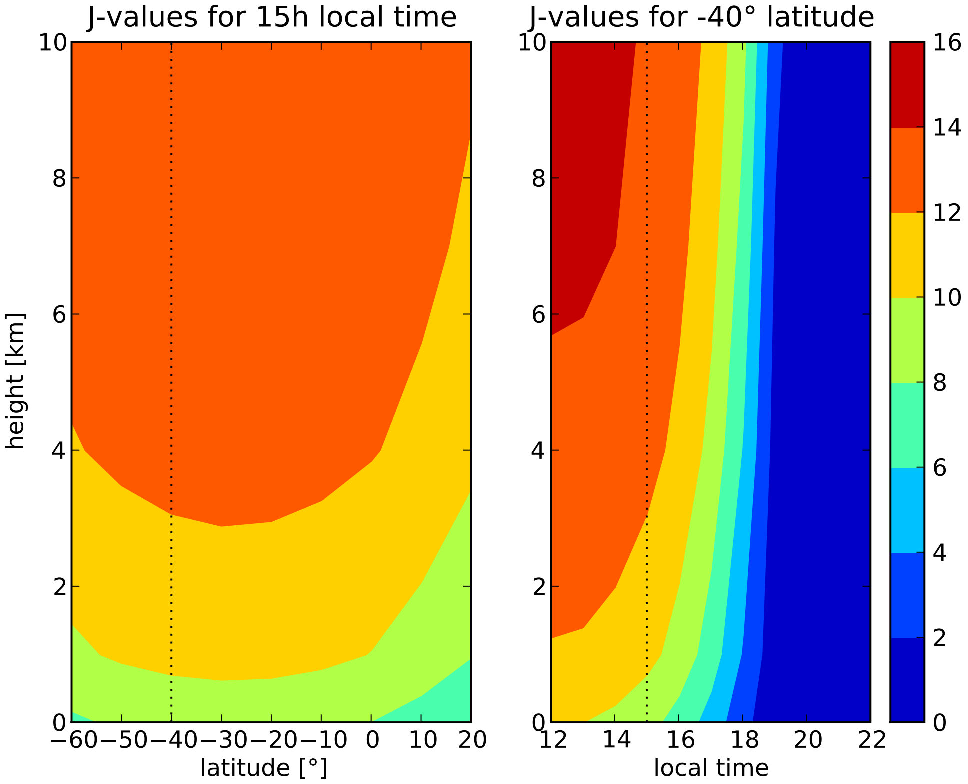

Figure 4.2: Photolysis rates $J_{\mathrm{NO_2}}$ in $[10^{-3}\,\mathrm{s}^{-1}]$ for the 15th of January. The left panel shows the photolysis rates $J_{\mathrm{NO_2}}$ at 15h local time for different latitudes and heights (note the height discretization of five height levels mentioned in the text). The right panel shows the photolysis rates $J_{\mathrm{NO_2}}$ at $-40°$ latitude for different height levels and local times. The dotted lines mark the corresponding intersection between the panels.

which J_{NO_2} depends. With increasing deviation from the local noon (where the actinic flux has a maximum at a given location) the solar zenith angle increases and the incident solar radiation decreases. This can be seen in the right panel of Figure 4.2, where J_{NO_2} decreases with increasing local time. For a certain height, a maximum can be observed for J_{NO_2} near $-30°$ latitude. For a fixed local time of 15h this corresponds to the lowest solar zenith angle which is located at $-26.1°$ latitude. The highest values for J_{NO_2} on the 15$^{\mathrm{th}}$ of January can be observed at local noon located at $-20.0°$ latitude (not shown). During night when sun is set, the photolysis rates are of course zero as the solar actinic flux is zero.

Photolysis rates are very sensitive to the actinic flux (see Equation 2.7). The actinic flux in the troposphere is modified to a great part by cloudiness. The resulting influence of cloudiness on photolysis rates is taken into account by Equation 2.10 as discussed in Section 2.2.1.

4.2 Results and Evaluation

In the following subsections an evaluation of the model results is presented. Tracer concentrations were calculated using the model setup described above with REMO 5.7 including chemistry and tracer transport (in the following denoted as $\mathrm{REMO}_{\mathtt{chem}}$).

As reference data, measured profiles of ozone, CO and total reactive nitrogen ($\mathrm{NO_y}$) from the INCA campaign are used. In addition, model results are compared with total column CO data retrieved from the MOPITT instrument and the corresponding vertical profiles.

4.2.1 Comparison with INCA

The main objective of the INCA campaign is to measure cirrus cloud properties, which are important for climate and ozone in the upper troposphere/lower stratosphere (e.g., Ström, 2002; Ström et al., 2003; Seifert et al., 2004). Additionally, several trace species are measured in order to characterize the degree of pollution of the specific air mass (Baehr et al., 2003). These include ozone, CO, $\mathrm{NO_y}$ and NO. All species are used in the comparison of this study, except for NO, where the uncertainties of the measurements are too high.

The INCA campaign took place in Punta Arenas in Chile in March/April 2000 and in Prestwick in Scotland in September and October 2000. In this study, only the ten measurement flights performed in Punta Arenas are used. These measurements represent rather clean and unpolluted air. They can therefore be used to assess the quality of the simulation of background concentrations in $\text{REMO}_{\texttt{chem}}$. The flights took place between 24th of March and 13th of April. Two flights were performed in the morning and during the night, respectively, while six flights took place in the afternoon and evening hours. The aircraft used is the Falcon of the German Aerospace Center (Deutsches Zentrum für Luft- und Raumfahrt, DLR). For further details of the measurement setup for the trace gases, refer to Baehr et al. (2003).

The aircraft was based in Punta Arenas from where the measurement flights were started. In Figure 4.3 the flight tracks and the base of the plane are depicted. They are located near the southern border of the model domain, which is located at about 58° South near the region of the INCA flights. Measurements performed close to the border of the model domain (within eight gridboxes distance from the border, which corresponds to about 4°) are omitted in the further comparison. They lie within the so called *sponge zone*, where the impact of the meteorological driving model – which decreases exponentially going from the border towards the center of the model domain – is relatively high.

This procedure reduces the amount of available measurements for the comparison, but also focuses them on a smaller region. The number of observations of CO, ozone and NO_y is reduced by 26 %, 42 % and 48 %, respectively. The same procedure is done for temperature and specific humidity to compare the meteorological conditions of the measurements and the simulation.

For the comparison one month of $\text{REMO}_{\texttt{chem}}$ data is used. It is simulated between 19th of March 2000 and 19th of April 2000. This period comprises the ten INCA measurement flights around Punta Arenas. The selected area comprises the region in which the INCA measurements were performed. It is represented by the black solid rectangle in Figure 4.3 and denoted as *INCA-region* in the following.

Comparing Meteorological Profiles

Meteorological conditions of the measurements are compared with the $\text{REMO}_{\texttt{chem}}$ simulation, using vertical profiles of temperature and specific humidity (Figure 4.4). For the comparison, INCA data is aggregated in sizebins of 50 hPa vertical extent, except for the lowest sizebin, which extends from 950 hPa to the ground.

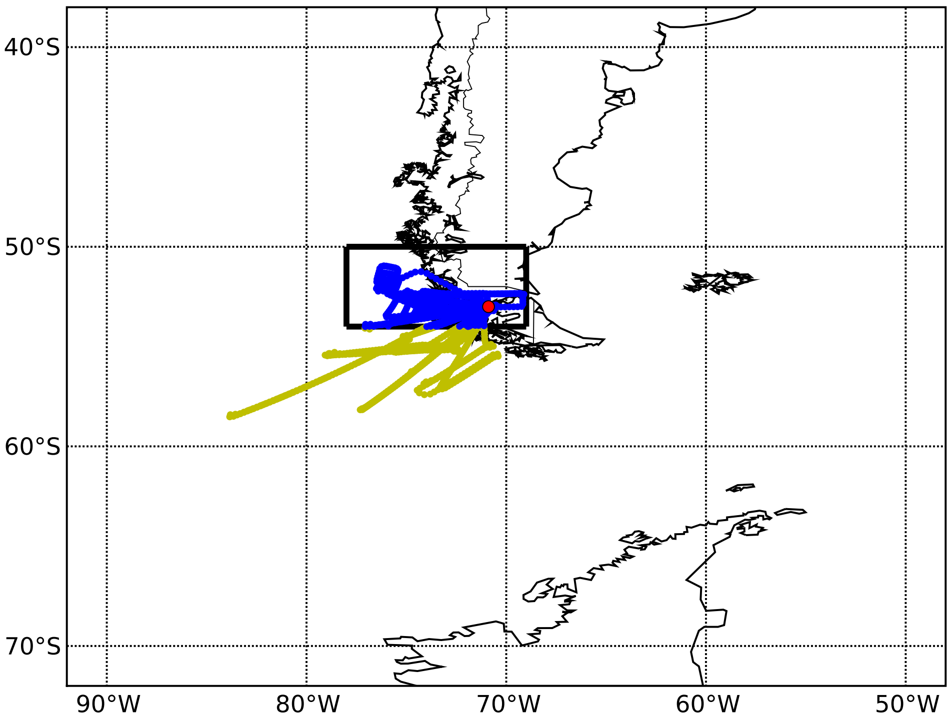

Figure 4.3: INCA mission flight tracks. Flight tracks of the INCA campaign near Punta Arenas (red dot) are depicted. Measurements taken into account are represented by the blue colored tracks, while measurements not taken into account are represented by the yellow flight tracks. The area used to calculate the REMO$_{\texttt{chem}}$ profiles for the comparison is represented by the black solid rectangle.

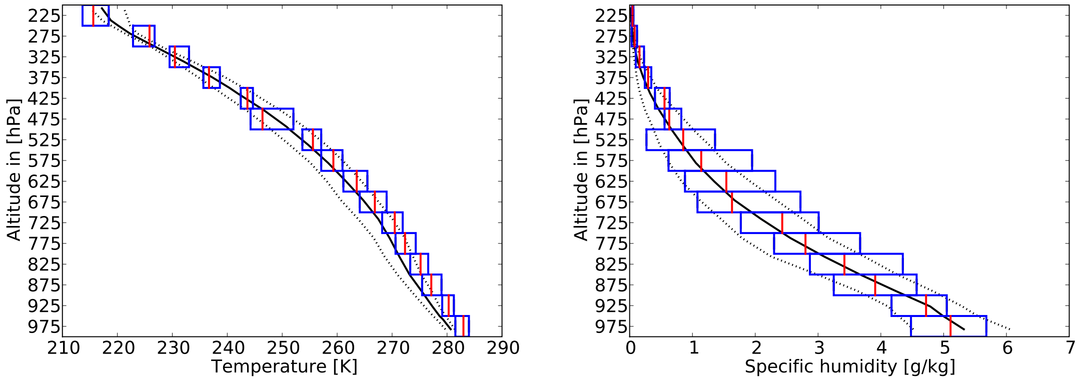

Figure 4.4: Temperature and specific humidity profiles. Median values of temperature and specific humidity measured during the INCA campaign are represented by the vertical red lines for sizebins of 50 hPa. The 25th and 75th percentiles are represented by the blue rectangle. Median values for $\mathrm{REMO}_{\texttt{chem}}$ (for the one month time period comprising the INCA campaign) are represented by the solid black line, while the 25th and 75th percentiles are represented by the dotted black lines. For details refer to the text.

Median temperature measured by INCA (left panel in Figure 4.4) decrease with height from 283 K at the lowest sizebin to about 216 K in the uppermost sizebin. The differences between the 25th and 75th percentiles (the so called *interquartile ranges*) lie between 8 K and less than 2 K. Median temperatures simulated by $\text{REMO}_{\texttt{chem}}$ decrease with height from about 280 K in the lowest level at 970 hPa to about 217 K in the uppermost level at 200 hPa. The interquartile range is less than 2 K in the lowest level. It increases with height to more than 6 K at around 675 hPa before it decreases again to about 2 K at 300 hPa.

Median specific humidity measured by INCA (right panel of Figure 4.4) decreases from 5.1 g/kg in the lowest sizebin to 0.05 g/kg in the uppermost sizebin. The interquartile range varies from 0.02 g/kg – 0.3 g/kg in the upper levels to 1.3 g/kg – 1.7 g/kg below 500 hPa altitude. Median specific humidity simulated by $\text{REMO}_{\texttt{chem}}$ decreases from 5.3 g/kg at the lowest level to 0.01 g/kg at the uppermost level. The maximum interquartile range of about 1.5 g/kg is located at the lowest level near the surface.

In general, $\text{REMO}_{\texttt{chem}}$ vertical profiles of temperature and humidity show a good agreement with the measured profiles. A slight cold bias of the $\text{REMO}_{\texttt{chem}}$ results can be observed below 500 hPa. The variability of the temperature values agrees well between INCA and $\text{REMO}_{\texttt{chem}}$. Also for specific humidity the median values as well as the variability in the model agrees well with the observations. Above about 600 hPa height a decrease in the variability can be observed in both, $\text{REMO}_{\texttt{chem}}$ and observations.

Altogether the meteorological situation can be considered similar in $\text{REMO}_{\texttt{chem}}$ and in the INCA measurements. Considering the fact that INCA measurements are performed mostly during the daytime – and are therefore not distributed equally over the hours of the day – the small negative bias of the $\text{REMO}_{\texttt{chem}}$ results can be explained. The cooling of air during the night is not evenly represented by the measurements, while it is considered equally in the model results.

The slight increase of the temperature gradient in the $\text{REMO}_{\texttt{chem}}$ profile in Figure 4.4 indicates the influence of stratospheric air near the tropopause.

Comparing Tracer Profiles

Similar to the meteorological profiles, tracer profiles are plotted in Figure 4.5. All measurement flights of INCA as well as the $\text{REMO}_{\texttt{chem}}$ data of all hours of the day are used to compute the profiles.

Ozone measured by INCA (upper left plot in Figure 4.5) increases from a median value of 22 ppbv in the lowest sizebin to about 52 ppbv in the uppermost sizebin around 225 hPa. The interquartile range increases with height from 4 ppbv in the lowest sizebin to 9 ppbv around 375 hPa. In the sizebins above this altitude the interquartile range is significantly larger of up to 26 ppbv in the uppermost sizebin. $\mathrm{REMO}_{\texttt{chem}}$ simulated ozone median values increase from 15.5 ppbv in the lowest level to 76 ppbv in the uppermost level. Interquartile ranges increase with height from 3.5 ppbv in the lowest level to 13 ppbv in the uppermost level.

Median values of CO measurements by INCA increase from 45 ppbv in the lowest sizebin to about 57 ppbv in the uppermost sizebin. The interquartile range increases slightly with height from 3 ppbv in the lowest sizebin to around 7 ppbv in the upper sizebins. CO median values simulated by $\mathrm{REMO}_{\texttt{chem}}$ are rather constant with height at values of about 55 ppbv, decreasing only at the uppermost level to 51 ppbv. Interquartile ranges increase with height from 1.5 ppbv in the lowest level to 8 ppbv in the uppermost level.

INCA measurements of $\mathrm{NO_y}$ are only available above an altitude of about 550 hPa. Despite fluctuations of the median value, an increase with height of $\mathrm{NO_y}$ concentrations can be observed: $\mathrm{NO_y}$ median value is lowest at the 575 hPa altitude sizebin with a value of 34 pptv and highest at the uppermost sizebin with a value of 145 pptv. $\mathrm{REMO}_{\texttt{chem}}$ median values decrease with height from the surface to about 700 hPa from 100 pptv to about 50 pptv before they increase up to 400 pptv at 200 hPa altitude.

In the upper left panel of Figure 4.5, we see that the ozone profiles are relatively similar in INCA and in $\mathrm{REMO}_{\texttt{chem}}$. However, $\mathrm{REMO}_{\texttt{chem}}$ seems to slightly underestimate ozone mixing ratios in the lower and middle troposphere compared to INCA, while in the upper troposphere/lower stratosphere mixing ratios are higher in $\mathrm{REMO}_{\texttt{chem}}$. Mixing ratios are increasing in the upper levels in both INCA and $\mathrm{REMO}_{\texttt{chem}}$. While the variability increases with height for the INCA measurements, it is rather constant in the $\mathrm{REMO}_{\texttt{chem}}$ results.

Considering the profiles of CO (the second panel in the upper row of Figure 4.5) we see that the increase in mixing ratio with height is higher for the INCA measurements than in $\mathrm{REMO}_{\texttt{chem}}$, while the order of magnitude is the same with mostly higher mixing ratios in $\mathrm{REMO}_{\texttt{chem}}$. In the uppermost levels a strong decrease in

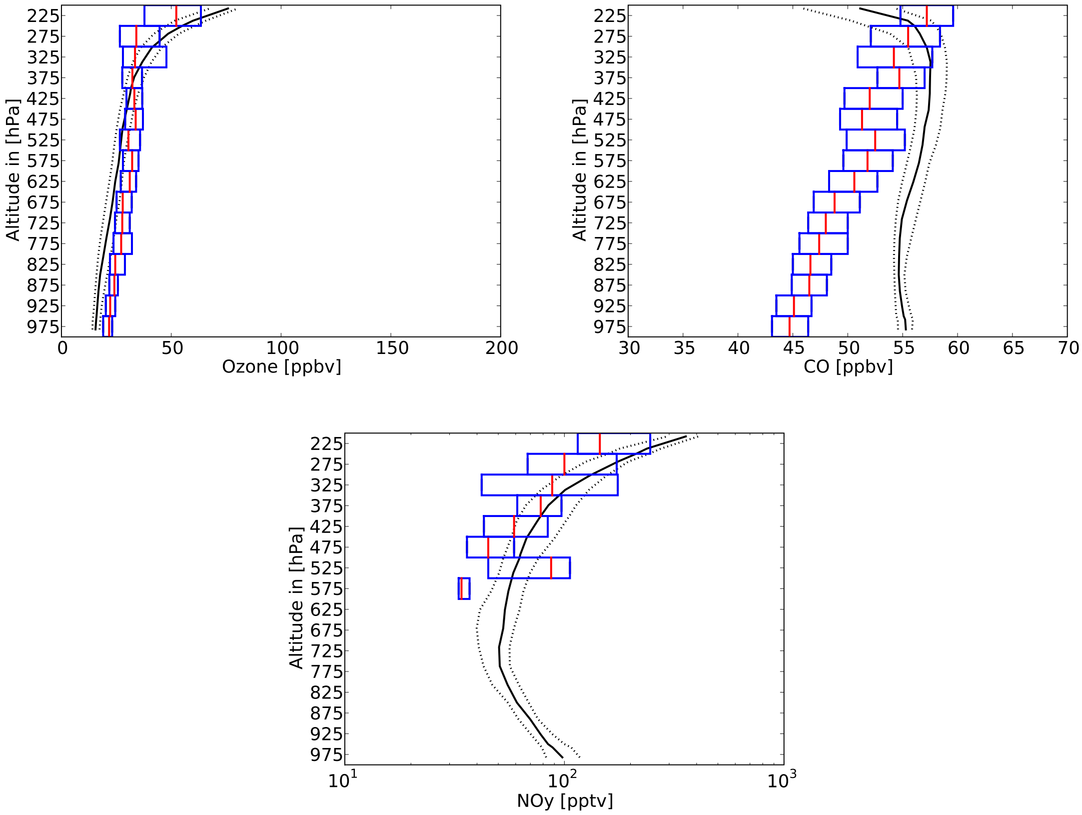

Figure 4.5: Tracer profiles of ozone, CO and NO_y. In the upper left panel and in the upper right panel, median profiles of ozone and CO are shown, respectively. The lower panel shows median profiles of NO_y. Median values measured during the INCA campaign are represented by the vertical red lines for sizebins of 50 hPa. The 25th and 75th percentiles are represented by the blue rectangle. Median values for $\text{REMO}_{\texttt{chem}}$ (for the one month time period comprising the INCA campaign) are represented by the solid black line, while the 25th and 75th percentiles are represented by the dotted black lines. For details refer to the text.

CO concentrations can be observed for the $\text{REMO}_{\texttt{chem}}$ data, which is not present in the INCA data. The variability increases slightly with height for both, $\text{REMO}_{\texttt{chem}}$ results and INCA measurements.

NO_y profiles are plotted in the lower panel of Figure 4.5. The order of magnitude and the shape of the profiles are similar with slightly higher values for $\text{REMO}_{\texttt{chem}}$ NO_y mixing ratios.

Considering the INCA CO profiles, low concentrations at the bottom and higher concentrations at higher altitudes are a sign of low emissions at the ground and the influence mainly of long range transport in higher altitudes. As the $\text{REMO}_{\texttt{chem}}$ profile has a much weaker gradient (except for the uppermost layers), it is possible that the emissions in $\text{REMO}_{\texttt{chem}}$ in the INCA-region are overestimated. Long range transport seems to be underestimated by the model, although present, as mixing ratios increase slightly with height in the upper layers.

The uppermost layers in $\text{REMO}_{\texttt{chem}}$ shown here seem to be located in the stratosphere or are at least influenced by stratospheric air as CO mixing ratios decrease and ozone mixing ratios increase at the same time. This is not the case for the INCA measurements, where CO mixing ratios increase also at the uppermost layers shown here (at least for 50 % of the measurements).

In Figure 4.6 tracer profiles similar to Figure 4.5 are plotted, but for morning hours only. Therefore only two INCA measurement flights are considered within about 9:00 h and 12:30 h local time. The two flights were performed on the 31st of March 2000 and on the 12th of April. For the calculation of the $\text{REMO}_{\texttt{chem}}$ profiles, the whole one month time period mentioned above was considered with the local hours between 9:00 h and 13:00 h.

Median ozone concentrations of INCA increase from 20 ppbv near the ground to more than 160 ppbv at 225 hPa. The interquartile range stays below 11 ppbv at pressure levels up to 475 hPa, while it reaches up to 114 ppbv above this level. Simulated ozone median values by $\text{REMO}_{\texttt{chem}}$ increase from 15.4 ppbv in the lowest level to over 77 ppbv in the uppermost level. Interquartile ranges increase with height from 3.5 ppbv in the lowest level to about 10 ppbv in the uppermost level.

Measured median values of CO from INCA, increase from 44 ppbv to 56 ppbv from the lowest level to 275 hPa, respectively. At 225 hPa CO median values are about 35 ppbv. The interquartile range for CO reach a maximum at 325 hPa with 22.5 ppbv. CO median values simulated by $\text{REMO}_{\texttt{chem}}$ increase from 55.5 ppbv in the lowest

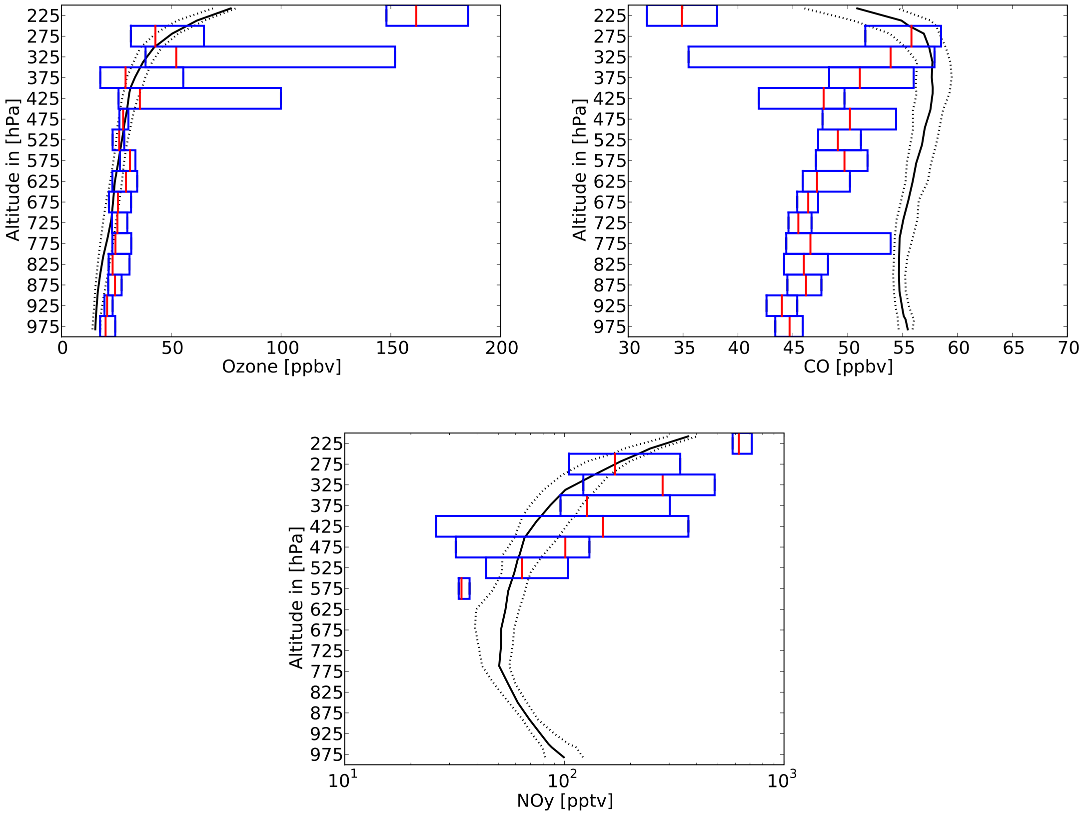

Figure 4.6: Morning hours tracer profiles of ozone, CO and NO$_y$. Tracer profiles of morning hours are plotted. The description of the plots are similar to those of Figure 4.5. For details refer to the text.

pressure level up to 57.7 ppbv at 325 hPa, before it decreases to 51 ppbv at 225 hPa. At this level, the interquartile range reaches a maximum with 8.5 ppbv.

NO_y median concentrations measured by INCA increase from 34 pptv at 575 hPa to 623 pptv at 225 hPa. Interquartile ranges are between 4 pptv and about 340 pptv. Simulated NO_y concentrations by $REMO_{\texttt{chem}}$ in the lowest pressure level are at 100 pptv and decrease to 50 pptv at about 775 hPa. They increase with altitude to 300 pptv at about 225 hPa.

Looking at the INCA-measurements which took place mostly during the morning (Figure 4.6), we see a different shape of INCA profiles compared to the daily mean profiles (Figure 4.5) while the $REMO_{\texttt{chem}}$ profiles are similar. For the morning flights, we see a strong decrease of CO measurements at the uppermost level (and a strong increase in ozone mixing ratios for the same level). These gradients are much stronger than in the $REMO_{\texttt{chem}}$ profiles.

Considering all INCA measurements (not only the measurements between the 25th and the 75th percentile), there is a large spread in the upper levels (not shown). Therefore the missing decrease in the INCA profile of CO mixing ratios at the highest model level for all times of day is probably related to the fact that the measurement flights of INCA do not cover all times of day equally. Also, the high ozone values of the INCA measurements during the morning might be related to single and rather local events of intrusion of stratospheric air at a specific location, which are not present in the field mean mixing ratios of the $REMO_{\texttt{chem}}$ profiles.

NO_y median concentrations of INCA show a slight positive shift if only morning values are considered. Additionally most of the interquartile ranges are greater, showing a larger spread in the measured values This indicates - like in the case for ozone - intrusion of stratospheric air in the upper levels during the time of the measurements.

Separating also the INCA measurements and the $REMO_{\texttt{chem}}$ profiles for afternoon/evening and night hours (not shown here), the monthly median $REMO_{\texttt{chem}}$ profiles are very similar showing no indication of a daily cycle for the species considered. The INCA measurements of ozone and CO do not show a strong variation for the lower levels for the different times of day supporting the $REMO_{\texttt{chem}}$ results.

Altogether, $REMO_{\texttt{chem}}$ and INCA agree reasonably well in the profiles of ozone and NO_y. The bias in the lower levels for CO of up to 20 % might be related to relatively high emissions values in $REMO_{\texttt{chem}}$ in the INCA region.

4.2.2 Comparison with MOPITT

In contrast to in situ measurements, satellite data has several advantages. Satellite retrievals usually cover large areas of the globe in a relatively short timeframe. Long-term consistent measurement datasets are produced during the lifetime of a satellite. A disadvantage of satellite data is the limited vertical resolution compared to in situ measurements, e.g., from measurement campaigns using airplane or balloon-borne sondes.

The MOPITT Instrument

MOPITT measures the global distribution of CO in the troposphere. The MOPITT instrument is located on board the Earth Observing System (EOS) Terra satellite of the National Aeronautics and Space Administration (NASA), which is flying in a sun-synchronous orbit. The Terra satellite was launched on the 19th of December 1999. Measurements from the MOPITT sensor are available since March 2000. The spatial horizontal resolution (instantaneous field of view) of MOPITT is 22 km × 22 km in nadir geometry. The swath width (width of the scanned area) is about 640 km. MOPITT data is provided on the so-called *retrieval grid*, which consists of the surface pressure level (p_{surface}) and the pressure levels 850, 700, 500, 350, 250 and 150 hPa. If the surface pressure is below one or more of these levels, it is neglected in the CO retrieval.

The MOPITT instrument uses a modulation cell containing CO as high-spectral resolution optical filter. From the transmitted radiation two synthetic signals are derived: The average signals and the difference signals (A-signals and D-signals, respectively). The A-signals are provided by calculating the mean radiation transmitted by the absorption cell. The D-signals are calculated as the difference between the cell states of minimum and maximum absorption. This corresponds to small and large optical depth conditions of the absorption cell, respectively.

The A-signal radiance is mainly sensitive to surface temperature (T_{surface}) and surface emissivity ($\epsilon_{\text{surface}}$) as it is dominated by the spectral region between the absorption lines of CO, leading to a rather high signal. The D-Signal is dominated by the spectral region close to the CO-absorption line and is therefore more sensitive to the atmospheric CO content. In the current CO retrievals used in this study one channel containing “A” radiances is used as well as three channels containing “D” radiances (for details refer to Deeter et al. (2003)).

MOPITT Retrieval

Measured radiances not only depend on the CO content of the atmosphere, surface temperature and on surface emissivity. Also other quantities defining the physical state of the atmosphere are important: The temperature profile as well as the water vapor profile of the atmosphere. These profiles cannot be calculated from the measured radiances.

To derive values and uncertainties for CO, T_{surface} and $\epsilon_{\mathrm{surface}}$ from the measured radiances (the procedure is called *retrieval*), the temperature and the water vapor profiles for each MOPITT pixel are interpolated from NCEP reanalysis data. They are used together with the measured radiances and the a priori state vector $\mathbf{x}_{\mathrm{a}}$ (containing the a priori CO profile, T_{surface} and $\epsilon_{\mathrm{surface}}$) to iteratively calculate the retrieved state vector $\mathbf{x}'$, which approximates the “real“ state of the atmosphere. The iteration is done using a forward radiative transfer model via the maximum a posteriori optimal estimation technique (for details refer to, e.g., Rodgers (2000) and Deeter et al. (2003)).

The a priori state vector $\mathbf{x}_{\mathrm{a}}$ as well as the a priori covariance matrix $\hat{\mathbf{C}}_{\mathrm{a}}$ is fixed. The a priori state vector is used for the retrieval of MOPITT CO profiles. It is derived from the global measurement dataset described in Deeter et al. (2003). The advantage of a globally fixed a priori state vector is that spatial patterns in the retrieved CO profiles cannot be caused by a variation in the a priori state vector. Another advantage is that the relative weight of the measured radiances in the retrieval increases for a globally fixed a priori state vector. The a priori state vector is shown in Figure 4.7 for the retrieval pressure levels. Standard deviations are calculated from the variances represented by the diagonal elements of the a priori covariance matrix.

Together with the state vector $\mathbf{x}'$ the error covariance matrix $\hat{\mathbf{C}}_{\mathrm{x}}$ is retrieved. Using the fixed a priori covariance matrix $\hat{\mathbf{C}}_{\mathrm{a}}$ the averaging kernel for a certain retrieved profile can be calculated as

$$\hat{\mathbf{A}} = \hat{\mathbf{I}} - \hat{\mathbf{C}}_{\mathrm{x}}\hat{\mathbf{C}}_{\mathrm{a}}^{-1}. \tag{4.1}$$

It relates the retrieved state vector $\mathbf{x}'$ to the ”true“ state vector of the atmosphere $\mathbf{x}_{\mathrm{true}}$ via

$$\mathbf{x}' = \hat{\mathbf{A}}\mathbf{x}_{\mathrm{true}} + (\hat{\mathbf{I}} - \hat{\mathbf{A}})\mathbf{x}_{\mathrm{a}}. \tag{4.2}$$

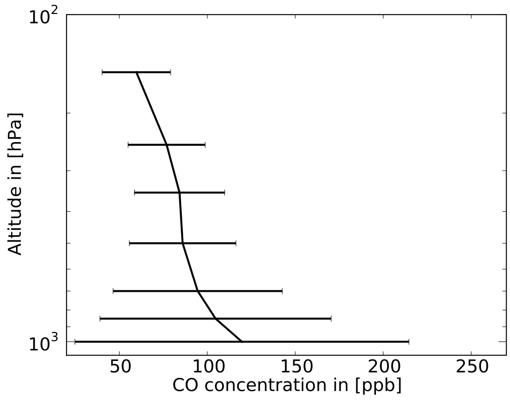

Figure 4.7: CO a priori profile. The vertical a priori CO profile is plotted together with the standard deviation derived from the a priori covariance matrix. For details refer to the text.

The averaging kernel describes the amount of a priori data included in each retrieval, which is usually non-zero as $\hat{\mathbf{A}}$ is not equal to $\hat{\mathbf{I}}$ for real retrievals. Additionally the averaging kernel describes the dependency of the CO concentration of each retrieval level on the CO concentrations of all levels.

As an example the daytime mean averaging kernels for April 2000 are plotted in Figure 4.8 for an ocean area (south Pacific, region 1 in Figure 3.1) and for an area over land (Amazon, region 3 in Figure 3.1). A typical daytime averaging kernel for retrieved surface CO concentrations over land shows the highest sensitivity on height levels of 700 hPa or 500 hPa and relatively low sensitivity on surface CO concentrations. This means that in this case the retrieved surface CO concentration is mainly influenced by CO concentrations in upper levels and by the a priori profile. The reason for the low information content in the retrievals in the surface level is the low sensitivity of the D-channels in the lowest layers of the atmosphere. The D-channels are used for the retrieval of the CO profile. Another example is the averaging kernel for 500 hPa in Figure 4.8. It shows a peak of the retrieval of CO content in 500 hPa altitude also at 500 hPa. The nonzero components at the other altitudes show that the retrieved CO concentrations are also influenced by CO on the other retrieval altitudes and by the a priori profile as it is shown in

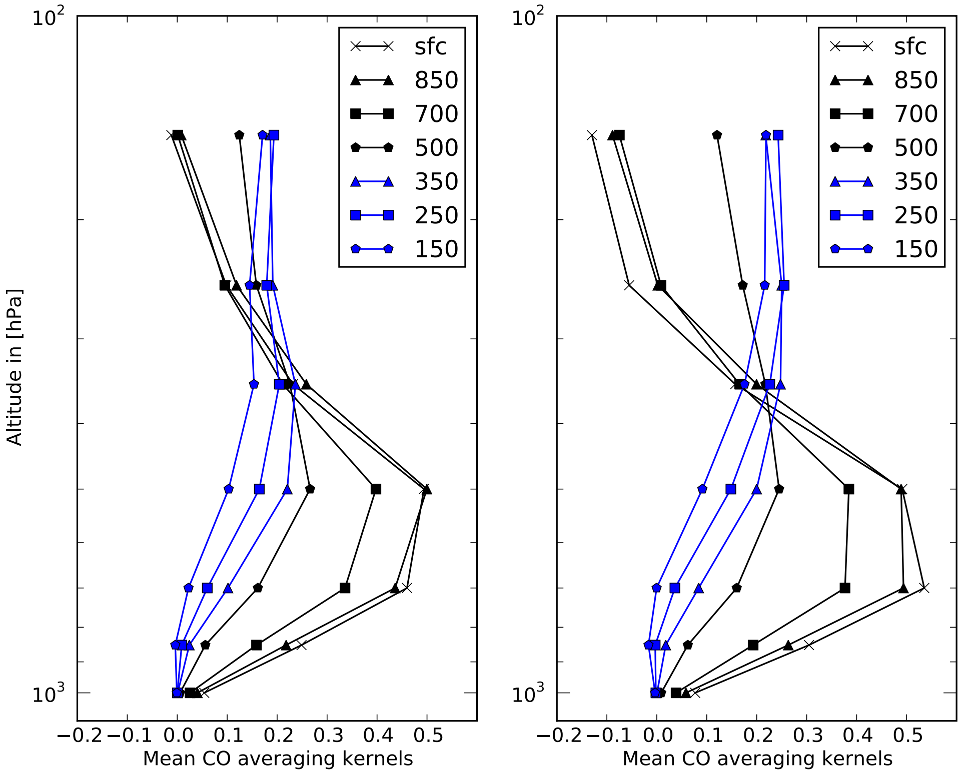

Figure 4.8: Daytime mean CO averaging kernels. The daytime mean CO averaging kernels are plotted for April 2000 for the south Pacific (region 1 shown in Figure 3.1) on the left hand side and for the Amazon region (region 3 shown in Figure 3.1) on the right hand side. Kernels for different retrieval heights are plotted: for the surface (denoted as *sfc*), 850, 700, 500, 350, 250 and 150 hPa. For details refer to the text.

Equation 4.2. This has to be taken into account when interpreting the retrieval results in comparison with model results.

Comparing the averaging kernels for the south Pacific and the Amazon in Figure 4.8, one can observe a downward shift of the averaging kernels over land. This signifies an increasing sensitivity to lower altitude CO concentrations. The higher thermal surface-atmosphere contrast over the Amazon region leads to a higher sensitivity of the D-channels in the lower troposphere and finally to a higher vertical information content in the retrieved profiles. In general, better separated averaging kernels – and therefore higher vertical information content in the retrieval – is obtained for higher thermal surface-atmosphere contrast (cf. Deeter et al., 2004a).

During the night, the temperature contrast between the atmosphere and the surface is smaller than during the day. The shape of the averaging kernels become similar and therefore the averaging kernels themselves are mathematically less independent of each other (not shown here). Well separated averaging kernels contain more independent vertical information. Additionally they are shifted to upper levels leading to an even reduced information content, e.g., of the real surface CO concentration and the 850 hPa CO concentration in the retrievals. In general, the vertical sensitivity of the MOPITT retrievals is much smaller during the night than during the day. Therefore only CO profiles retrieved during daytime are considered in the comparison with model data in this study.

The MOPITT data used in this study is the MOPITT Level-3 monthly mean gridded CO data, derived from daytime retrievals. It is aggregated from the Level-2 data product, which consists of geolocated retrieved CO profiles and total column amounts, onto a $1° \times 1°$ global grid. A global coverage is obtained after approximately three days. The retrieval of CO profiles is based on the assumption that only clear-sky radiances are used. Therefore only pixels which are not contaminated by clouds are used in the retrieval. Clouds are detected by the MOPITT cloud detection algorithm described in Warner et al. (2001). Depending on the cloudiness at overflight times, the calculated monthly average of CO concentration is based on a certain number of retrievals. In regions with frequent cloud cover, the monthly average can be based only on a few retrieved profiles, or cannot be calculated at all. The cloud detection algorithm of Warner et al. (2001) works well with cloud cover of more than 5 % to 10 %.

Extensive validation of the MOPITT data has been done (see, e.g., Deeter et al., 2004b; Crawford et al., 2004; Bremer et al., 2004; Warner et al., 2007). According to

Pan et al. (1998) theoretical MOPITT retrieval errors for CO are of approximately 10 %. Vertical CO profiles from MOPITT retrievals are compared with in situ data from different measurement campaigns, e.g., by Emmons et al. (2004). They found a general good agreement between satellite and in situ data. The mean bias of surface CO concentrations is relatively large (8.1 % ± 21.5 %) during Phase 1 of the MOPITT retrievals (March 2000 to May 2001). It decreases with height to a bias of −0.2 % ± 15.8 % at 150 hPa. The total column CO bias is found to be 4.9 % ± 10.8 %. The standard deviation of the bias for each level and for the total column is always larger than the bias itself. This is related to uncertainties in the retrieval and to an uncertainty in the determination of the bias. MOPITT retrieval errors are not shown in the graphs of this study.

REMO Pseudo Retrieval

In order to compare MOPITT retrievals with REMO results, it is important to consider the overpass times of the TERRA satellite. The TERRA satellite is flying in a sun-synchronous orbit (i.e., it passes the same places at the same time). For the REMO model region (depicted in Figure 3.1) the overpasses lie approximately between 13:00 and 16:00 UTC. For the comparison, only REMO data within this timeframe is considered in order to avoid a bias due to the daily cycle of CO.

As discussed before, the vertical information content of the MOPITT retrievals is limited. When comparing, it is important to apply the vertical sensitivity of MOPITT (represented by the averaging kernels) to the model data. The procedure is called *pseudo retrieval*. In this case, the CO profiles from the REMO data ($\mathbf{x}_{\mathrm{remo}}$) are taken as the "real" CO content $\mathbf{x}_{\mathrm{true}}$ in Equation 4.2:

$$\mathbf{x}'_{\mathrm{remo}} = \hat{\mathbf{A}}\mathbf{x}_{\mathrm{remo}} + (\hat{\mathbf{I}} - \hat{\mathbf{A}})\mathbf{x}_{\mathrm{a}}. \tag{4.3}$$

After the pseudo retrieval the resulting vertical profiles $\mathbf{x}'_{\mathrm{remo}}$ have the same a priori information content as the corresponding MOPITT retrievals. From both, MOPITT retrievals and REMO pseudo retrievals, the retrieved total column CO content is calculated.

Comparing the Seasonality of Total Column CO Concentrations

The yearly cycle of CO total column values is shown for the year 2000 (March to November) in Figure 4.9 for different regions of South America. Error bars

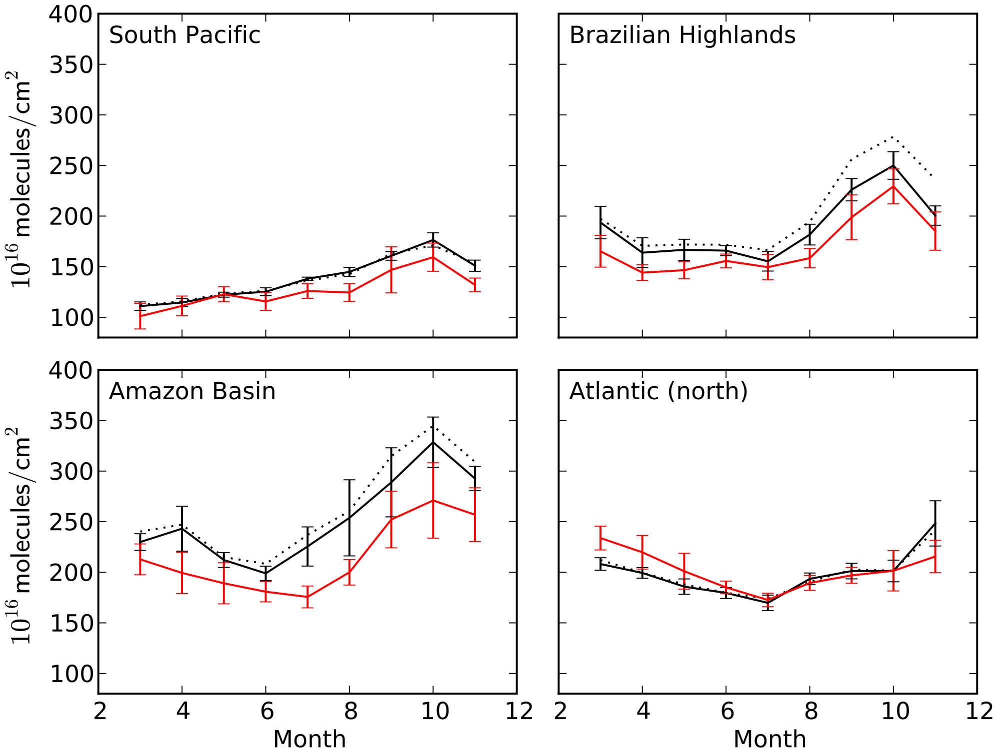

Figure 4.9: CO total column in different regions in South America. The yearly cycle of the total column of CO is plotted for different regions in South America (see Figure 3.1) in [10^{16} molecules/cm^2]. Total column values for REMO pseudo retrievals and for MOPITT retrievals are plotted in black and in red, respectively. The error bars correspond to the standard deviation of the monthly mean values in the region. The black dotted line corresponds to the REMO pseudo retrieval without considering the cloud cover in the model.

correspond to the standard deviation of the monthly mean values. They therefore represent the spatial variability of the monthly mean values in the region.

In some regions CO concentration is related to cloud cover. MOPITT retrievals are only performed if no cloud cover is detected. This might lead to a bias in the retrieved CO concentration of the atmosphere. To take this into account, REMO pseudo retrievals are only performed if the cloud cover in the REMO results is smaller than 10 %. The corresponding CO concentrations are plotted as solid black lines in Figure 4.9, 4.12 and 4.13. As a reference, REMO pseudo retrievals without considering the REMO cloud cover are plotted as dotted black line, omitting the error bars for clarity reasons. Gridboxes without a MOPITT retrieval are masked out in both REMO retrievals.

For comparison of CO total column, four regions are selected (see Figure 3.1) in order to represent typical wind and emission patterns described in the following. The south Pacific region (region 1) represents a remote area dominated by background CO concentrations. The Brazilian highlands region (region 2) is located in proximity to the Amazon basin and include the megacities of São Paulo, Rio de Janeiro and Belo Horizonte. This area is dominated by local emissions and by transport from the Atlantic and the Amazon region. The Amazon basin (region 3) is located in the center of the South American continent. It is mostly dominated by local emissions as horizontal advection is rather week. The Atlantic region in the northern part of the model domain (region 4) is dominated by advection from African emissions, which originate from outside the model domain.

In the following the yearly cycle of CO total column values of MOPITT and $\text{REMO}_{\texttt{chem}}$ depicted in Figure 4.9 is considered. For the months of April and October, horizontal plots of CO total column retrievals of MOPITT and pseudo retrievals of $\text{REMO}_{\texttt{chem}}$ are depicted in Figure 4.10.

Peak values are reached in October in the three regions south Pacific, Brazilian highlands and the Amazon basin of 176, 250 and 329 molecules/cm^2 in $\text{REMO}_{\texttt{chem}}$ and 160, 230 and 271 molecules/cm^2 in MOPITT, respectively, as can be observed in Figure 4.9. Minimum values simulated by $\text{REMO}_{\texttt{chem}}$ and measured by MOPITT can be found in March in the south Pacific region. They are at 111 and 101 molecules/cm^2, respectively. In the Brazilian highlands, CO total column values are below 170 molecules/cm^2 between April and May, while they are below 156 molecules/cm^2 for MOPITT in the same time period. Minimum values for the CO total column in the Amazon basin can be found in June for $\text{REMO}_{\texttt{chem}}$

(200 molecules/cm^2) and in July for MOPITT (176 molecules/cm^2). In the Atlantic region, the minimum in CO total column values is located in July around 170 molecules/cm^2 for both, MOPITT and REMO$_{\texttt{chem}}$. The maxima in the considered time period are in March and November between 200 and 250 molecules/cm^2.

Over the land areas (the Brazilian highlands and the Amazon basin), the yearly cycle associated with the so-called *fire season* can be observed. Relatively low CO total column values in the first half of the year can be related to the wet season, when the occurrence of forest fires is low. During the dry season in the second half of the year (the fire season) the number of forest fires increase strongly. This corresponds to elevated CO total column values in the Amazon basin and the Brazilian highlands during this time of the year.

The CO total column values in the remote area of the south Pacific show a steady increase starting from March until October after which the total column CO decreases again. The increase of CO can be associated with the increase in southern hemisphere CO emissions from biomass burning in the second half of the year as the global lifetime of CO is about two months. This is long enough for hemispheric transport.

The region in the northern part of the South Atlantic (region 4) is dominated by easterly winds. African emissions are transported into the model domain via the boundaries and dominate the CO concentration in the investigated region. African peak fire season in Western Africa south of the Sahel zone is around November and December. In the West African coastal zone the peak fire season is around February to April (e.g., van der Werf et al., 2003). During single events, fire emissions can also be transported from South Africa up to the north eastern coast of South America. The fire seasons in Africa can therefore explain the high column concentrations in the region in the beginning and in the end of the year in the Atlantic region.

When comparing total column values for MOPITT retrievals and REMO pseudo retrievals in Figure 4.9 (the red and black solid lines, respectively) a positive bias in the REMO pseudo retrievals can be observed except for the region in the northern Atlantic. In the south Pacific region, where the CO concentrations are relatively small, the positive bias of REMO in comparison with MOPITT exceeds 10 % only in August and November. The yearly cycle, with its increasing emissions until the peak of the fire season in October, is similar in both retrievals, indicating an influence of the fire emissions even in this rather remote area.

The variability of the retrieved monthly mean CO total column values in the region is represented by the standard deviation in Figure 4.9. It is smaller in REMO than in MOPITT. This can result from the relatively small number of MOPITT retrievals per month in this region (cf. Figure 4.11 for the months of April and October): Relatively few retrievals in a single gridbox lead to a high variance in the expected monthly mean value. Furthermore the satellite track does not necessarily cover the entire region at one overpass. Total column values for CO might be retrieved at different days for different gridboxes. In contrast, the contribution to the REMO retrieval comprises the whole domain for each considered hour, except for cloud covered gridboxes. At a certain time, CO total column fields are rather homogeneous in the south Pacific region, as there are no distinct local emission sources. This leads to less variation in the monthly means of the REMO pseudo retrievals compared to the MOPITT retrievals in this region.

The yearly cycle in the Brazilian highland region in Figure 4.9 shows a positive bias for REMO in comparison with the MOPITT total column CO concentrations of less than 15 % except for March 2000. The CO total column concentrations are influenced by local emissions as well as by rather clean air masses transported over the Atlantic into the region. The spatial variability is of about the same magnitude in REMO as in MOPITT. Inhomogeneities in the monthly mean CO concentrations are relatively large, due to scattered local emission sources.

The positive bias in the Amazon basin exceeds 10 % for all months except for March. Local fire emissions dominate the CO total column concentrations, which can also be seen in the high spatial variability of the monthly means. Wind speed is rather low in the lower part of the troposphere leading to a relatively low horizontal dispersion of CO emissions. In combination with convective transport, CO is transported to higher levels. As MOPITT retrievals and REMO pseudo retrievals are most sensitive in the lower free troposphere (cf. Figure 4.8), strong convective transport in combination with overestimated emissions in REMO might lead to the positive bias in REMO.

The region in the north eastern part of the model domain located in the Atlantic is dominated by transport from the boundary. Strong winds advect CO emitted in Africa into the region of interest. Except for March and November, the weighted difference between MOPITT and REMO lies within a 10 % distance. The positive bias of MOPITT in comparison with REMO can be related to relatively low boundary concentrations of CO in the REMO simulation. Additionally, the number of retrievals per gridbox is relatively low in MOPITT from March to May and in November in this region compared to June to October (not shown). This explains also that inhomogeneities are present in the MOPITT retrievals during this month, although emissions are homogeneous over the ocean and the advected CO plumes are rather broad.

Comparing the Spatial Patterns of Total Column CO Concentrations

Horizontal plots of the total column retrieved CO concentrations from MOPITT and the CO concentrations from the REMO pseudo retrievals are shown in Figure 4.10 for April and October 2000. The corresponding number of pixels which are used for the MOPITT retrievals in each gridbox is plotted in Figure 4.11. White pixels signify that during the whole month time period, no retrieval was possible due to cloudiness. REMO pseudo retrievals are performed in those gridboxes where MOPITT retrievals are present.

Considering the horizontal pattern of the total column CO concentrations in Figure 4.10 for April and October 2000, large scale patterns can be compared between MOPITT and REMO. The two months of April and October are chosen in order to represent CO concentrations outside and inside the biomass burning season in the Amazon, respectively. In white gridboxes corresponding to MOPITT retrievals, no retrieval was possible due to clouds, whereas in white gridboxes corresponding to REMO pseudo retrievals, no MOPITT retrieval was possible or the cloud cover modelled by REMO exceeded 10 %. The corresponding number of MOPITT retrievals per gridbox per month for April and October are shown in Figure 4.11.

The number of MOPITT retrievals per gridbox is an indicator for the reliability of the MOPITT retrievals themselves. It has to be kept in mind when interpreting the retrieved CO total column values. Fewer retrievals per gridbox can be associated with less confidence in the calculated monthly mean value for this gridbox. Near the equator, satellite tracks are overlapping leading to more potential retrievals per gridbox than over high latitudes, where satellite tracks do not overlap. Also in the Amazon region the retrievals per gridbox are rather sparse, which can be related to elevated cloud cover.

In April (upper plots in Figure 4.10), the main pattern of the MOPITT retrieval and the REMO pseudo retrieval agree rather well. The positive bias of REMO in the regions considered before can also be observed here. In the Amazon basin and west of

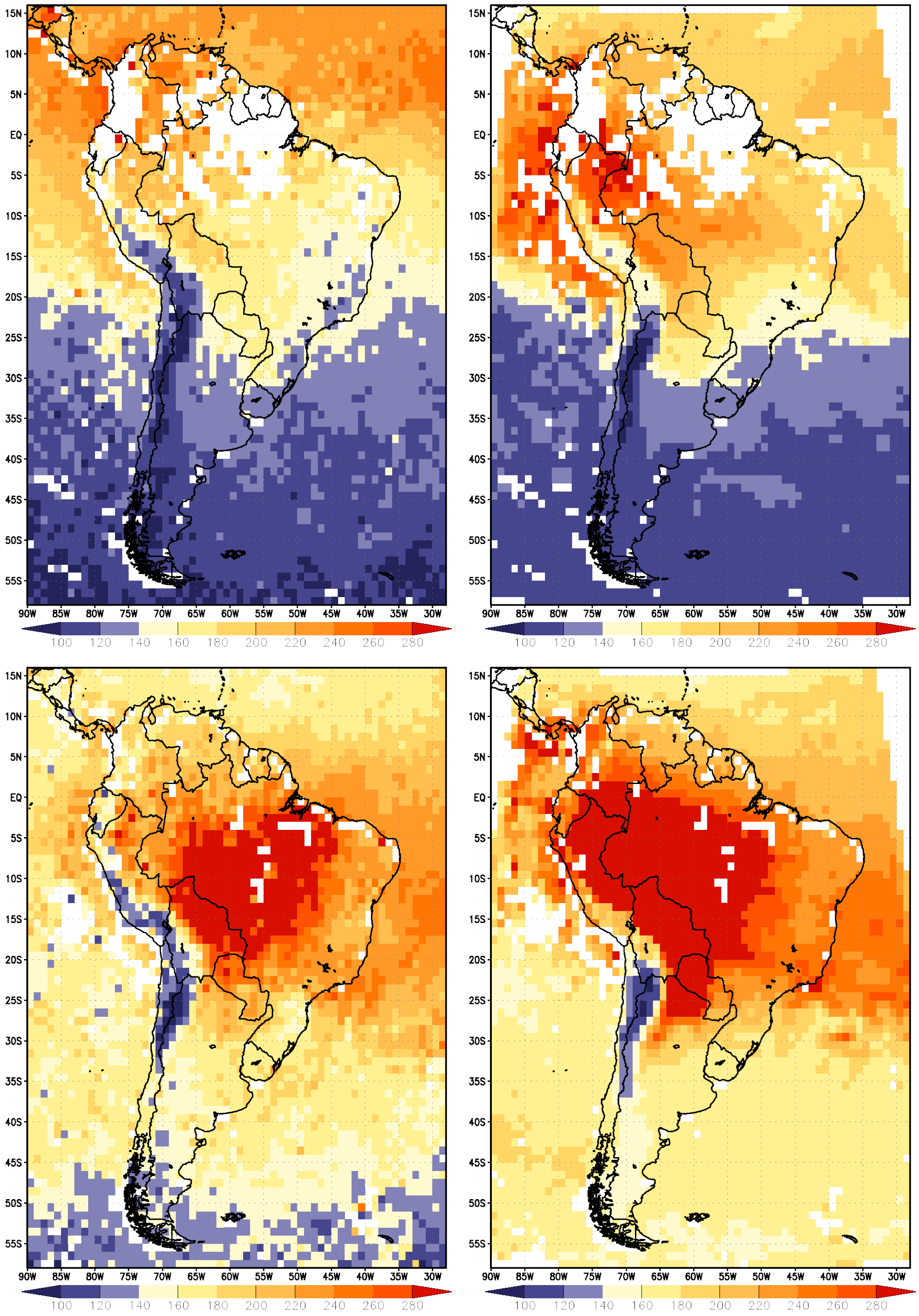

Figure 4.10: Monthly mean CO total column. The total column is plotted for CO in [10^{16} molecules/cm^2]. MOPITT retrievals are shown on the left hand side. REMO pseudo retrieval results are shown on the right hand side. The upper and lower plots show results for April and October, respectively. For details refer to the text.

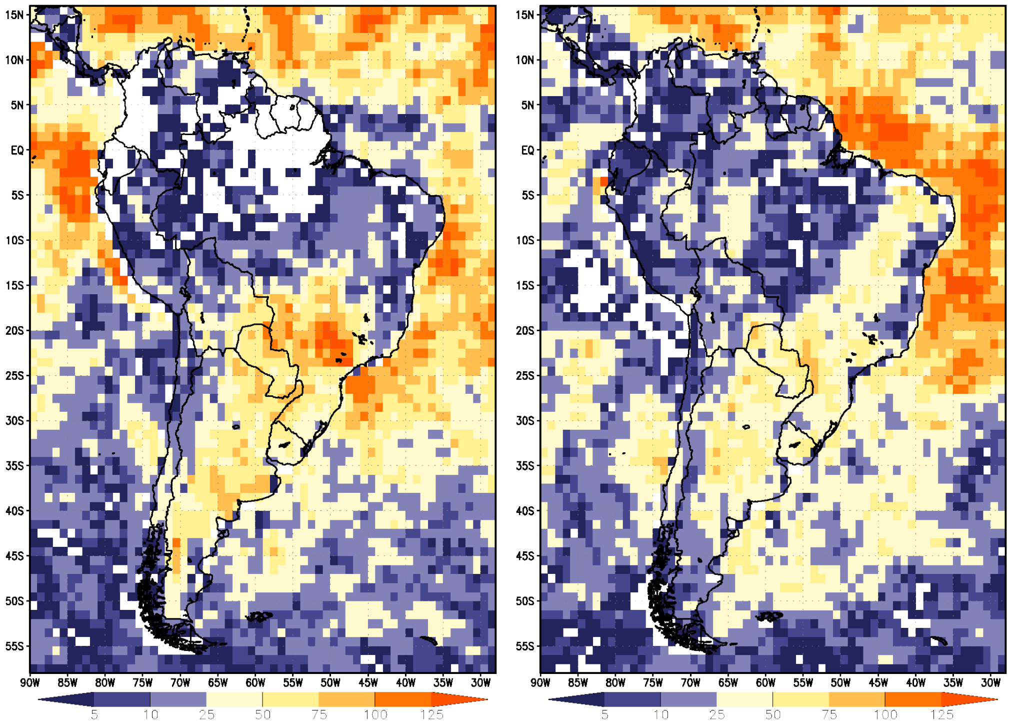

Figure 4.11: Monthly number of pixels used for CO retrieval. The number of pixels which contributed to the monthly mean total CO column calculation of each gridbox is plotted. Results are shown for April and October on the left hand side and on the right hand side, respectively. For details refer to the text.

the northern Andes, REMO pseudo retrievals exceed $260 \cdot 10^{16}$ molecules/cm^2 in large areas, whereas the MOPITT retrievals exceed this value only in a few gridboxes. At least for the Amazon basin, the number of retrievals in MOPITT is very low (cf. Figure 4.11). Monthly mean values calculated from only a few retrievals might underestimate the CO total column values in MOPITT. Over the Pacific, where more MOPITT retrievals contribute to the monthly mean, CO total column values are slightly higher and therefore closer to the REMO pseudo retrievals. The Andes can be recognized in both plots with relatively low CO total column concentrations reaching into the northern part of South America. In the north eastern part of the plotted domain, CO total column concentrations are slightly higher in MOPITT than in REMO. This could be the result of an underestimation in CO in the REMO boundary data, as this area is dominated by advection from the boundaries, as discussed earlier.

In October (lower plots in Figure 4.10) the CO total column concentration in a large area is dominated by biomass burning. The CO total column concentrations are larger than in April in the whole model domain. The area in which the total CO column concentration exceeds $280 \cdot 10^{16}$ molecules/cm^2 is mainly located in the Amazon basin. In the REMO pseudo retrievals it has a larger extent towards the south and towards the north west than the MOPITT retrievals. In the MOPITT retrievals the CO total column concentrations near the mouth of the Amazon river exceed 280×10^{16} molecules/cm^2, while they are lower in the REMO pseudo retrievals. In the inflow region in the northern part of the model domain in the Atlantic, concentrations are similar in both plots. In the southern part of the depicted area, towards Antarctica, CO total column concentrations are lower in the MOPITT retrievals than in the REMO pseudo retrievals. Note that in this region as well as in the Amazon the number of MOPITT retrievals per gridbox is rather low (cf. Figure 4.11). Monthly mean values are based on only a few measurements and are therefore less reliable.

In both months shown here, April and October, the MOPITT retrievals look more patchy than the REMO pseudo retrievals. This is caused by the nature of the satellite retrievals with their limited swath width and temporal coverage of the domain, discussed above.

In summary, an overall good agreement between the main features of MOPITT and REMO can be observed. In some parts of the model domain, REMO pseudo retrievals show higher total column concentrations of CO than MOPITT retrievals.

This can be the result of an underestimation of CO total column concentrations in MOPITT, possibly related to cloud cover (see section below). On the other hand, a positive bias in the REMO pseudo retrievals might result from several factors: The wind simulated in the REMO simulation (run in climate mode) might deviate from reality, leading to a CO transport to other regions. Although the main wind patterns are supposed to be the same on a climate time scale, they might deviate from reality in the relatively small time frame considered.

An overestimated convective transport of CO into atmospheric layers of relatively high sensitivity of the pseudo retrievals (about 700 hPa, see Figure 4.8) can lead to an overestimation of CO concentrations in the whole column (cf. Section 4.2.2). On the other hand, an underestimation of the total column CO concentration of MOPITT might result from predominant pollution transport to layers of lower sensitivity. In reality, heat release related to biomass burning leads to high buoyancy and a related strong convective transport to atmospheric layers of high altitudes. Pollutants released at the biomass burning site are transported efficiently to the free troposphere and even to the lower stratosphere (see, e.g., Lavoué et al., 2000; Luderer et al., 2006; Freitas et al., 2007). The heat release of biomass burning and the related convective transport is not yet implemented in the REMO model. As a result, the model in the current setup tends to overestimate CO concentrations in the lower model levels. Together with the relatively high sensitivity of all averaging kernels at levels of 700 hPa and 500 hPa an overestimation of CO at these altitudes is likely to lead to an overestimation of total column CO.

Another important factor of uncertainty is the biomass burning in the emission inventories (Bian et al., 2007). An overestimation in the biomass burning emissions in the inventory might also lead to the relatively high CO total column concentrations in the REMO pseudo retrieval.

Another possible source of the positive bias of REMO with respect to MOPITT is discussed in the following section.

Relating Cloud Cover with the CO Total Column

Cloud cover is highly variable in time and space. In a climate simulation, clouds cannot be expected to occur exactly at the same time and in the same gridbox as in reality (although the cloud statistic can be expected to be similar). Gridboxes that are not considered in MOPITT due to a detected cloudiness of more than

10 % in all retrievals, are also masked out in the REMO pseudo retrievals. Nevertheless, there are gridboxes in which a MOPITT retrieval was possible due to a detected low cloudiness, while in the same gridboxes the cloud cover exceeds 10 % in REMO. In the discussed comparison between REMO and MOPITT total column values, gridboxes with a cloud cover of more than 10 % in the REMO simulation are also not considered in the REMO pseudo retrievals (solid black line in Figure 4.9). The dotted black line in the same figure represents the total column values of the REMO pseudo retrievals in which also cloudy gridboxes (according to the REMO simulation) are considered.

In the south Pacific region and in the Atlantic region there is practically no difference for the two cases of considering REMO clouds in the REMO pseudo retrievals or not. Both regions are located over the ocean with homogeneous low local emission sources. They are dominated by strong winds, advecting CO into and out of the region. Oxidation of CO (Equation 1.6) in a considered gridbox plays a minor role in determining the total column CO concentration of the very same gridbox. Air is well mixed in both regions not leaving time to chemical processes to develop inhomogeneities in the CO field originating from a heterogeneous cloud cover.

In the Brazilian highlands as well as in the Amazon basin there is a difference between the two methods which is largest during the fire season in September, October and November. Including gridboxes in the REMO pseudo retrievals, for which the cloud cover is greater than 10 % in REMO, leads to a positive bias compared to the case where those gridboxes are omitted. Therefore, cloud cover in REMO is related to higher CO total column concentrations in the REMO pseudo retrieval.

The positive bias in the REMO pseudo retrieval which includes the cloudy gridboxes in REMO can be explained by a reduced loss of CO via the reaction with OH (Equation 1.6). OH is produced via the photolysis of ozone at wavelength of $\lambda <$ 320 nm:

$$\mathrm{O_3} + h\nu \longrightarrow \mathrm{O(^1D)} + \mathrm{O_2} \tag{4.4}$$

$$\mathrm{O(^1D)} + \mathrm{H_2O} \longrightarrow 2\,\mathrm{OH} \tag{4.5}$$

In the presence of clouds, the actinic flux is reduced. This leads to a lower concentration of OH (Equations 4.4 - 4.5) and in consequence to less CO destruction and therefore to higher CO concentrations.

In a region, where the major source of CO is chemical production via methane (Equation 1.1) or NMHC, reduced OH concentrations would also reduce CO production.

This process counteracts the reduced CO destruction and therefore diminishes the net effect of OH concentrations on CO concentrations. In the Brazilian highlands and in the Amazon basin, where a positive bias can be observed, CO emissions play a major role in the CO production leaving the chemical production of CO less important. Additionally the CO concentrations in the gridbox are dominated by chemical processes and local sources rather than by advection of CO from other gridboxes as the wind velocities in both regions are rather low. In the south Pacific region and in the Atlantic region, where no significant bias can be observed, both conditions are not fulfilled: Wind velocities are high and there are no large local sources of CO.

The common procedure of averaging CO satellite retrievals over larger areas therefore leads to a potential systematic underestimation of CO concentrations when comparing with model data without accounting for the effect of cloudy pixels.

Vertical CO Profiles

Vertical profiles of the MOPITT retrievals and the REMO pseudo retrievals are depicted in Figure 4.12 for April 2000 and in Figure 4.13 for October 2000 for the four regions discussed above: south Pacific, Brazilian highlands, Amazon basin and Atlantic. Note that again the error bars correspond to the standard deviation of the monthly mean values for each retrieval level. They therefore represent the spatial variability of the monthly mean values in the region for each retrieval level.

It is important to note that the vertical profiles of the retrieved MOPITT and the pseudo retrieved REMO CO concentrations depend partly on the a priori CO profile Figure 4.7. Examples of vertical sensitivity are shown in Figure 4.8, represented by the averaging kernels.

A maximum in retrieved CO concentrations can be found at the lowest pressure level in all four regions for April and October and for MOPITT retrievals and REMO pseudo retrievals. The values for April are 74 and 66 ppbv in the south Pacific region, 99 and 91 ppbv in the Brazilian highlands, 129 and 155 ppbv in the Amazon basin and 135 and 123 ppbv in the Atlantic region for MOPITT and REMO, respectively. The strongest decrease of CO concentrations with height can be found in the lower two pressure levels in the case of the south Pacific and in the lower three pressure levels in the Amazon basin and in the Atlantic region. In the Amazon basin REMO pseudo retrievals have a positive bias ranging from 27 ppbv in the lowest pressure

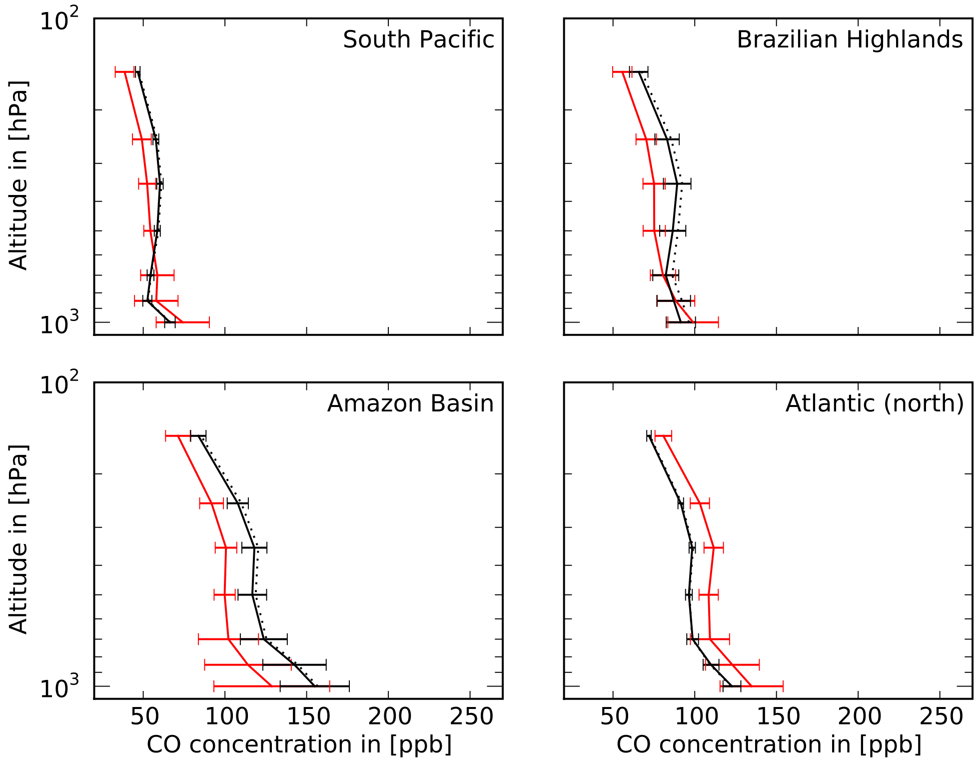

Figure 4.12: Vertical CO profiles in different regions in South America for April 2000. CO profiles for REMO pseudo retrievals and for MOPITT retrievals are plotted in black and in red, respectively. The error bars (located at retrieval pressure levels) correspond to the standard deviation of the monthly mean values in the region. The black dotted line corresponds to the REMO pseudo retrieval without considering the cloud cover in the model. The different regions are shown in Figure 3.1

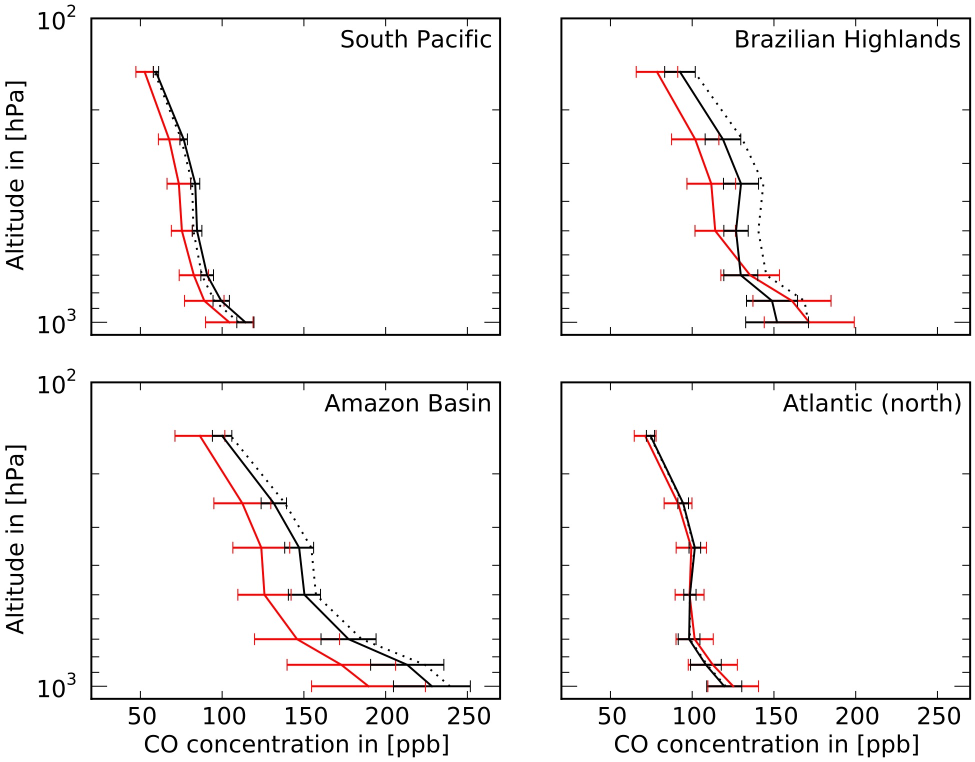

Figure 4.13: Vertical CO profiles in different regions in South America for October 2000. CO profiles for REMO pseudo retrievals and for MOPITT retrievals are plotted in black and in red, respectively. The error bars (located at retrieval pressure levels) correspond to the standard deviation of the monthly mean values in the region. The black dotted line corresponds to the REMO pseudo retrieval without considering the cloud cover in the model. The different regions are shown in Figure 3.1

level to 13 ppbv in the uppermost pressure level. The positive bias of MOPITT retrievals in the Atlantic region is about 10 ppbv in April. In the south Pacific and in the Brazilian highlands, no constant bias can be observed.

In October, vertical profiles show the highest gradients mostly in the lower pressure levels. Absolute values of CO concentrations are higher than in April: In the south Pacific region and in the Atlantic, CO concentrations in the lowest pressure level are around 110 ppbv and 120 ppbv, respectively, for MOPITT and for REMO. In the Brazilian highlands, REMO pseudo retrievals in the lowest pressure level are at 152 ppbv, while MOPITT retrievals are at 172 ppbv at the same level. In the Amazon basin, MOPITT retrievals are at 189 ppbv in the lowest pressure level, while the REMO pseudo retrieval has a positive bias of 39 ppbv. This positive bias decreases with height to about 14 ppbv in the uppermost pressure level. In the south Pacific, the positive bias of REMO is about 10 ppbv, while no constant bias can be observed in the other regions.

The differences in the yearly cycle between both retrievals (cf. Figure 4.9) can also be observed in the retrieved vertical profiles for the specific months. The vertical profiles show, e.g., the positive bias of REMO in the Amazon basin in April and in October and the positive bias of MOPITT in the Atlantic region in April together with the good agreement in October.

The positive bias in the REMO pseudo retrievals in the case in which the cloudy gridboxes are not considered in REMO pseudo retrievals, can also be observed in the retrieved vertical profiles. It is highest during the biomass burning season in October in the Brazilian highlands and in the Amazon basin. The bias decreases slightly with height showing a greater influence of cloudiness in the lower levels. This might be related to an efficient chemical loss via Equation 1.6 in atmospheric layers, where the CO concentration is high. These layers are located in the lower troposphere near the emission sources.

The spatial variability of the monthly mean CO concentrations at different levels is represented by the error bars. Different spatial variability shown in the total column CO retrievals in Figure 4.9 are also represented in the vertical profiles. In addition the vertical profiles show a decrease with height of the spatial variability in MOPITT retrievals as well as in REMO pseudo retrievals. The decrease is more pronounced in regions comprising distinct heterogeneous emission sources, like the biomass burning emissions in the Amazon and in the Brazilian highlands. The reason is that lower atmospheric layers are dominated by the heterogeneous fire emissions, while in upper layers horizontal transport also influences CO concentrations and leads to mixing of air masses.

Considering the variability of the total column values in the region and the MOPITT retrieval error (not shown in the plots), there is a good agreement between MOPITT and REMO.

4.3 Conclusions and Outlook

The comparison of $R_{\text{reference}}$ with the INCA measurements and the MOPITT retrievals shows a good performance of $\text{REMO}_{\texttt{chem}}$. While ozone and NO_y profiles agree reasonably well with INCA, a positive bias of $\text{REMO}_{\texttt{chem}}$ of about 20 % can be observed for CO profiles in the lower troposphere. This can be related to an overestimation in the CO emissions in this region or to a reduced chemical loss of CO via Equation 1.6.

The comparison of REMO pseudo retrievals with MOPITT shows a good agreement of the horizontal patterns and of the yearly cycle of the CO total column. Positive and negative biases of REMO pseudo retrievals are mostly within the range of 10 % of the corresponding MOPITT pseudo retrieval. This corresponds to the MOPITT retrieval error. Only in the Amazon basin – the region with the most frequent biomass burning events – the positive bias exceeds 10 % in the majority of cases. This can be related either to an overestimation in the REMO emission inventories or to a higher uncertainty (more than 10 %) in the MOPITT retrievals as retrievals are relatively sparse due to cloudiness.

The REMO pseudo retrievals show that the selection process of non-cloudy pixels for the calculation of the CO concentrations leads to a potential underestimation of CO. This happens in areas where CO is produced to a large extent by sources other than methane and NMHC oxidation and where horizontal advection plays a minor role in determining the CO concentration. This might also cause a negative bias, when MOPITT retrievals are compared to reality without considering the effect of cloudy pixels.

Despite the relatively good agreement with observation data, $\text{REMO}_{\texttt{chem}}$ simulations can be improved. So far, NO_x production by lightning is not included in $\text{REMO}_{\texttt{chem}}$. Labrador et al. (2005) investigated the impact of NO_x emissions from lightning and found the highest impact to be in the tropical middle and upper troposphere. In the lower extratropical troposphere they found that including lightning NO_x production in their model leads to a slight decrease in total surface NO_x concentrations, confirming similar results by Stockwell et al. (1999). As the focus of this study lies on tropospheric air pollution near the surface, the bias due to missing lightning NO_x is supposed to be small. Nevertheless it plays an important role for the middle and upper tropospheric NO_x concentrations.

Another important issue is the consideration of the daily cycle and the so-called *weekend effect* in anthropogenic emissions. Anthropogenic emissions are not distributed equally over the day as well as over the days of the week. Peak emissions of primary pollutants (like CO, NO and reactive hydrocarbons), e.g., originating from commuter traffic, are present during work days in the morning and in the late afternoon hours in the case of the Los Angeles region (Elkus and Wilson, 1977). These patterns differ for different regions of the world (related to cultural habits) and can even vary from city to city. The weekend effect was observed in tropospheric NO_2 concentrations, e.g., by Beirle et al. (2003) using satellite retrievals from the Global Ozone Monitoring Experiment (GOME). In the $\text{REMO}_{\texttt{chem}}$ experiments discussed in this study, only monthly mean emissions are assumed. Although important for air pollution peaks inside and in the vicinity of cities, the effect of the daily cycle might be diminished due to pollutant dilution of the relatively coarse horizontal grid used in $\text{REMO}_{\texttt{chem}}$. Nevertheless, going to higher resolutions the influence of both, weekend effect and daily emission cycle will increase and will be included in $\text{REMO}_{\texttt{chem}}$ in the future. An advantage of using "flat" monthly mean emissions is that the daily cycle in the concentrations can be directly attributed to changing meteorological conditions.

In addition to the daily cycle of anthropogenic emissions, the emissions emanating from biomass burning related to human activities also show a distinct diurnal cycle. Typical deforestation fires peak in the afternoon at around 15 h (e.g., Prins et al., 1998; Hoelzemann, 2006). Additionally, Prins et al. (1998) show a day to day variation of South American fire counts related to biomass burning emissions. The daily cycle of biomass burning emissions is of minor importance for air quality in distant areas due to dilution during transport. Day to day variation of biomass burning emissions on the other hand might also influence air quality in distant areas as the time between peak emission events is of the same magnitude as the time needed for transport. In the future it is planned to include higher time-resolved biomass burning emissions in the modelling framework of $\text{REMO}_{\texttt{chem}}$.

As discussed in Section 4.2.2, the injection height of the fire emissions plays an important role in local air pollution and long range transport. Due to the fact that biomass burning emissions are released in the lowest model level, local air pollution near the emission sources is overestimated while long range transport is underestimated. Fire emissions also influence the air quality in megacities (see Chapter 5). This effect might be overestimated in $\text{REMO}_{\texttt{chem}}$, as long range transport of pollutants from biomass burning is reduced in the middle and upper troposphere by not including plume rise in the model (e.g., refer to Freitas et al. (2006)). Pollutant concentrations in the lower troposphere are therefore enhanced.

Photolysis rates are calculated by a preprocessor and are then interpolated and modified according to the actual actinic flux (see Section 2.2.1). Online calculation of photolysis rates is more computational demanding, but would lead to more accurate reaction rates for photolysis reactions.

Deeter et al. (2007) found that lognormal retrieval are closer to reality than the normal operational retrieval due to the fact that constraint values - such as tracer concentrations which are positively constraint - are better represented by lognormal distributions. An improved retrieval algorithm for both, MOPITT retrieval and REMO pseudo retrieval can lead to a better agreement as several biases originating from the normal retrieval procedure are avoided.

Future studies will quantify the effects of lightning NO_x, weekend effect and daily cycle in emissions onto tropospheric tracer concentrations. A subgrid scale plume rise model or a parametrization of plume rise will be included in the model to improve the representation of biomass burning emissions. A further downscaling inside the model domain can improve the model results and reduce the dilution of chemical tracers.

5 Megacity and Biomass Burning Impact on Regional Air Quality

In this chapter, the impact of megacity and biomass burning emissions on air quality in South America is investigated. In Section 5.1.1 $\text{REMO}_{\texttt{chem}}$ simulations with modified emission inventories used in this chapter are presented. In order to quantify the relative impact of the different emission sources on regional air quality, different impact measures are defined in Section 5.1.2. Two study regions, in which the relative impact is investigated in detail are defined in Section 5.1.3.

Simulated regional air quality in South America is discussed in Section 5.2.1, while the impact on regional air quality on a continental scale is investigated in Section 5.2.2. The influence of transport patterns on tracer concentrations is investigated for two study regions in Section 5.2.3. Production of ozone is investigated in the same two study regions in Section 5.2.4.

5.1 Methodology

5.1.1 Simulation Setup

Like the reference run $\text{R}_{\text{reference}}$ the sensitivity runs are embedded in the long term hindcast of the ERA-40 period $\text{R}_{\text{ERA 40}}$ as described in Section 4.1. Again there is no feedback of the chemical mechanism onto meteorology (cf. Figure 2.3). This is essential for the interpretation of the sensitivity runs as modified tracer concentrations are subject to exactly the same meteorology in all sensitivity runs. Therefore changes in the resulting tracer concentration fields can be directly attributed to the respective emission changes.

In order to investigate the impact of emissions from megacities and from biomass burning, the respective emissions of the emission inventory described in Section 4.1 are modified as follows:

- 90 % reduction of megacity emissions

- omission of biomass burning emissions

Modified Megacity Emissions

Anthropogenic emissions from megacities in South America are reduced by 90 %. Megacities with modified emissions in this study are listed in Table 1.1. Their location in the model domain is depicted in Figure 1.1. A model run is performed embedded in $R_{\mathrm{ERA\,40}}$ including the modified emission inventory. In the following this run is denoted as $R_{\mathrm{decreased\,MCs}}$.

The reduction of 90 % of anthropogenic emissions can be thought of as a drastic – although unrealistic – technological improvement of combustion processes.

The locations of the gridboxes corresponding to megacities in South America with modified anthropogenic emissions are depicted in Figure 1.1. The number of modified gridboxes of each megacity is listed in Table 1.1. Each gridbox comprises an area of approximately $55 \times 55\,\mathrm{km}^2$. While the size of the megacities is usually in the order of magnitude of only one gridbox in reality, more than one gridbox is attributed to each megacity in the emission inventory used in $\mathrm{REMO}_{\mathtt{chem}}$. A megacity can be located on the intersection of two or more gridboxes leading to an attribution of their emissions to several REMO gridboxes. Megacities are attributed to gridboxes according to their geographic location and their emission pattern in the anthropogenic emission inventory. Megacity emissions are rather constant throughout the year. For comparison, the seasonal cycle of anthropogenic emissions attributed to megacities considered in this study in the year 2000 is plotted in Figure 5.1 together with biomass burning emissions: As an example, emissions of four different species (CO, NO, formaldehyde (HCHO) and ethane (C_2H_6)) are depicted.

CO emissions from the megacities considered in this study are between 4.4 Tg/yr and 5 Tg/yr, while NO emissions are about 0.5 Tg/yr. Emissions of HCHO and C_2H_6 are about 0.01 Tg/yr and 0.05 Tg/yr, respectively.

Modified Biomass Burning Emissions

In contrast to megacity emissions, fire emissions have a strong seasonal cycle and vary in magnitude from year to year (Schultz et al., 2008b).

Emissions from biomass burning exhibit a strong seasonal cycle with very low emis-

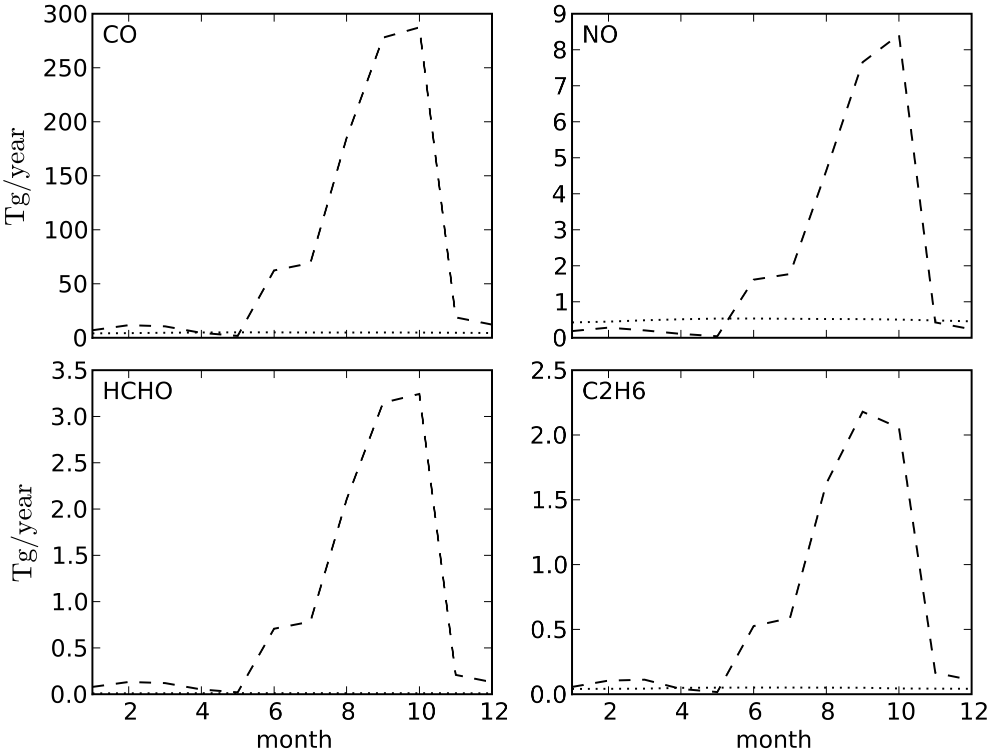

Figure 5.1: Megacity and biomass burning emissions in South America. The yearly cycle of monthly mean emissions emanating from megacities (dotted line) and biomass burning (dashed line) are plotted for selected species. For details refer to the text.

sions from November to May (during the wet season) and high emissions during June to October (the so-called *biomass burning season*). CO emissions from biomass burning are between 2 Tg/yr and 20 Tg/yr in the wet season. In the same time period biomass burning emissions of NO lie between 0.04 Tg/yr and 0.4 Tg/yr, emissions of HCHO and C_2H_6 both lie between 0.02 Tg/yr and 0.2 Tg/yr. During the biomass burning season, emissions from biomass burning are larger. They peak in October for CO, NO and HCHO with total emissions corresponding to 290 Tg/yr, 8.4 Tg/yr and 3.2 Tg/yr, respectively. Emissions of C_2H_6 peak at about 2.2 Tg/yr in September.

The order of magnitude of biomass burning emissions and megacity emissions is the same for CO and NO between January and May and for December. During the fire season, biomass burning emissions greatly surpass megacity emissions. Biomass burning emissions from HCHO and C_2H_6 exceed emissions emanating from megacities during the whole year except for May where biomass burning emissions are lowest.

Not only the amount of trace gases and aerosols emitted by fires changes with time, but also the location. As an example, total CO emissions in the model region are plotted in Figure 4.1. The main features are discussed in Section 4.1.

In order to assess the relative impact of biomass burning emissions on air pollution a REMO simulation is performed in which all emissions from biomass burning are set to zero in the emission inventory. This simulation is denoted as $R_{\text{no fires}}$.

In summary, biomass burning emissions vary greatly in magnitude and location throughout the year, while megacity emissions are rather constant. Fires are located mostly in the Amazon, i.e., away from the coast and high population centers. Therefore, the impact of fire emissions on the population might not scale with the total amount of emitted pollutants by biomass burning, although it is very high during the fire season compared to megacity emissions. The impact is investigated quantitatively in this chapter.

5.1.2 Relative Impact Measures

In order to quantify the impact of emissions from megacities (*MCs*), a measure for each species similar to the one proposed by Guttikunda et al. (2005) is defined: The relative impact of the reduction of megacity emissions by 90 %, e.g., on NO_x

concentrations is defined as

$$I^{\mathrm{MCs}}_{\mathrm{NO_x}} = \frac{C_{\mathrm{NO_x}}(\mathrm{R_{reference}}) - C_{\mathrm{NO_x}}(\mathrm{R_{decreased\,MCs}})}{C_{\mathrm{NO_x}}(\mathrm{R_{reference}})} \tag{5.1}$$

where $C_{\mathrm{NO_x}}$ ($\mathrm{R_{reference}}$) and $C_{\mathrm{NO_x}}$ ($\mathrm{R_{decreased\,MCs}}$) denote the $\mathrm{NO_x}$ concentration in $\mathrm{R_{reference}}$ and $\mathrm{R_{decreased\,MCs}}$, respectively. This measure represents the relative change of trace gas concentrations with respect to $\mathrm{R_{reference}}$ due to, e.g., changes in the emission inventory in $\mathrm{R_{decreased\,MCs}}$.

Similar to $I^{\mathrm{MCs}}_{\mathrm{NO_x}}$, the impact of biomass burning emissions (*fires*) on $\mathrm{NO_x}$ concentrations is defined as

$$I^{\mathrm{fires}}_{\mathrm{NOx}} = \frac{C_{\mathrm{NO_x}}(\mathrm{R_{reference}}) - C_{\mathrm{NO_x}}(\mathrm{R_{no\,fires}})}{C_{\mathrm{NO_x}}(\mathrm{R_{reference}})} \tag{5.2}$$

with $C_{\mathrm{NO_x}}$ ($\mathrm{R_{no\,fires}}$) denoting the $\mathrm{NO_x}$ concentrations in $\mathrm{R_{no\,fires}}$.

The impact measure of a certain pollutant increases with an increasing influence of its corresponding emission source onto the pollutants concentration in a certain region: A relative impact $I^{\mathrm{MCs}}_{\mathrm{NO_x}}$ (R 1) of 40 % signifies that the reduction of emissions from megacities by 90 % leads to a decrease in $\mathrm{NO_x}$ concentrations of 40 % in R 1 compared to the unmodified emissions case. A negative relative impact of, e.g., −10 % signifies that the modified emission inventory would lead to an increase of the pollutant concentration of 10 %. The impact measures are applied to the different study regions defined in the following section.

In order to quantify the total impact of a distinct emission source in the model domain, the concepts of *impact area* and *population impact* are introduced. The definitions follow the suggestion of Lawrence et al. (2007). They investigated pollution potentials of megacities using the total surface area of the model grid cells with a tracer density exceeding certain thresholds. In this study, the impact area A is defined as the total area experiencing relative impact values exceeding a certain threshold. For example, the impact area for $\mathrm{NO_x}$ emissions from megacities is defined as:

$$A^{\mathrm{MCs}}_{\mathrm{NOx}}(10\,\%) = \text{surface area with } I^{\mathrm{MCs}}_{\mathrm{NOx}} > 10\,\% \tag{5.3}$$

The impact area for other pollutants and other emission sources is defined accordingly.

In order to assess the impact of different emission sources and trace gases on the population, the population impact P is defined similar to the impact area. It is defined as the number of people living in the corresponding impact area A. The population impact of megacity emissions of NO_x, e.g., is defined as

$$P_{\mathrm{NOx}}^{\mathrm{MCs}}(10\,\%) = \text{population living in } A_{\mathrm{NOx}}^{\mathrm{MCs}}(10\,\%) \tag{5.4}$$

The population impact for other pollutants and other emission sources is defined accordingly.

In this study, population data from the Gridded Population of the World Version 3 (GPWv3) [1] is used to calculate the population impact.

5.1.3 Study Regions

Two *impact regions* (R 1 and R 2) are selected in which the development of trace gas concentrations is investigated for a one month time period before and during the biomass burning season. The impact regions are depicted in Figure 1.1.

The two regions mentioned above comprise 2 × 2 gridboxes with an area of approximately 12100 km^2. The size is comparable to the areas attributed to megacities. R 1 is located west of São Paulo with a distance of approximately 165 km between the two centers. R 2 is located close to the coast south-west of São Paulo in a distance of about 700 km. The distance to Buenos Aires is about 1100 km, which is located south-west of R 2. In R 1 it is possible to study the direct outflow of São Paulo, while the medium range transport can be investigated in R 2.

5.2 Results and Discussion

In this section the impact of megacity emissions and emissions from biomass burning on air quality in the lowest model level is quantified. In Section 5.2.1, regional air quality in South America as simulated by REMO$_{\texttt{chem}}$ is analyzed. In Section 5.2.2, the total area and the population influenced by emissions from megacities and biomass burning is quantified using the relative impact measures defined in Section 5.1.2.

---

[1] Center for International Earth Science Information Network (CIESIN), Columbia University; and Centro Internacional de Agricultura Tropical (CIAT). 2005. Gridded Population of the World Version 3 (GPWv3): Population Grids. Palisades, NY: Socioeconomic Data and Applications Center (SEDAC), Columbia University. Available at http://sedac.ciesin.columbia.edu/gpw. (10th of December 2008).

In order to get a complete picture of the impact of different emission sources on air quality in a specific region, several factors have to be taken into account: Tracer concentrations near the surface are influenced by chemical reactions and emissions as well as by advection of tracers emitted in distant regions. In the following sections, different factors influencing air quality in the study regions R 1 and R 2 are analyzed. Two different time periods are considered: a one month time period before and a one month time period during the biomass burning season (April and October, respectively). In Section 5.2.3, the influence of transport patterns on air quality is investigated. In Section 5.2.4 different ozone production regimes are investigated.

5.2.1 Regional Air Quality in South America

Many trace species and aerosols determine the air quality in a certain region as described in Section 1.3. In this section simulated near-surface ozone concentrations are analyzed together with the respective consequences for air quality. The two months of April and October are considered. They represent a time period outside and inside the biomass burning season, respectively (cf. Section 5.1.1).

Ozone Concentrations in the Lowest Model Level

Monthly mean ozone concentrations are shown in Figure 5.2 for the lowest model level. The height of the lowest model level is approximately 60 m.

Simulated ozone concentrations in April range between values below 10 ppbv in the north-western part of Brazil to values between 30 and 40 ppbv at low latitudes near the northern border of the model domain. These values can also be observed close to the megacities of São Paulo and Rio de Janeiro as well as at some locations in the center of Brazil. At high latitudes (about south of Buenos Aires), ozone concentrations range between 10 and 20 ppbv.

In October, highest simulated ozone values can be found in the eastern part of Bolivia and northern Paraguay. Peak monthly mean ozone concentrations range between 80 ppbv and 90 ppbv. In large parts of Brazil simulated near surface ozone values are greater than 30 ppbv. In single gridboxes close to São Paulo and Rio de Janeiro, monthly mean ozone concentrations range up to between 40 ppbv and 50 ppbv. In the regions around Santiago de Chile and Buenos Aires, mean ozone concentrations range between 10 ppbv and 30 ppbv. The ozone values close to the

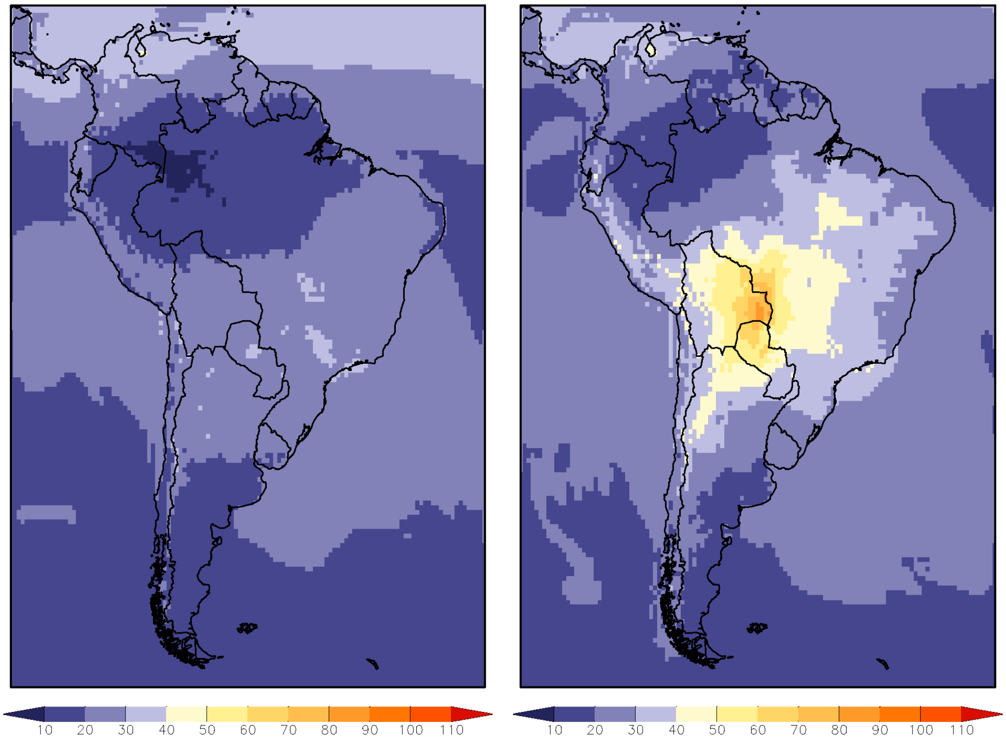

Figure 5.2: Monthly mean surface ozone concentrations for April and October 2000. Simulated monthly mean ozone concentrations are plotted in [ppbv] for the lowest model level for April and October 2000 on the left and on the right hand side, respectively.

coastal region in northern South America, range between 20 and 40 ppbv.

Elevated ozone concentrations in several gridboxes in the south-western coastal region of Brazil indicate pollution originating from the megacities of São Paulo and Rio de Janeiro. This slight elevation of ozone concentration can be observed in April and in October 2000 in Figure 5.2. A slight elevation of monthly mean ozone can be observed for October 2000 in the region in Peru where Lima is located.

In the Amazon region in the north-western part of Brazil, monthly mean ozone concentrations are relatively low and can reach concentrations below 10 ppbv in April. Different factors can be the reason for the comparatively low ozone concentrations in the Amazon region in April: High cloudiness in the wet season in the Amazon region leads to a decreased actinic flux and therefore to a decrease in ozone production (see Section 1.4). Ozone production can also be reduced due to relatively low NO_x concentrations in this region: In April (outside the biomass burning season), NO_x concentrations are about two to four times lower in the discussed part of the Amazon region than in large parts of the rest of the continent (not shown). Together with the large amount of volatile organic compounds emitted from the Amazon forest, a NO_x-limited ozone production seems likely (cf. Section 1.4). In the south-western part of Brazil, where ozone concentrations are higher, also increased NO_x concentrations can be observed in comparison with the north-western Amazon region. This supports the assumption of NO_x limited ozone production in the Amazon region during April.

In October, elevated ozone concentrations are present in the southern part of the Amazon region and parts of Bolivia and Paraguay. At similar locations, large fire emissions can be observed in October (cf. Figure 4.1). Together with CO, large amounts of NO_x are emitted (not shown). In a region, where ozone production is NO_x-limited, additional emitted NO_x by biomass burning, leads to an increase in ozone production. This seems to be the case in the region with increased ozone concentrations discussed above.

Exceedance of Air Quality Guidelines for Ozone

Air pollution can influence human health as described in Section 1.3. Whether human health is affected by a certain pollutant and to what extent the human body suffers from inhalation of polluted air depends on the concentration of the respective pollutant. The *World Health Organization* (WHO) compiled guideline values for different pollutants based on epidemiological research (WHO, 2000, 2006). The goal is to provide concentration thresholds of pollutants under which the risk of hazardous effects on human health is minimized. For pollutant concentrations below the guideline values, it is believed that no hazardous effects on human health will occur. Nevertheless it is possible that highly sensitive people are affected at or even below the given thresholds. This can be the case for people who are already affected by other diseases, children and elderly people. Exposure values in the WHO guideline are provided for exposure to single pollutant species separately. Health effects can occur below the given thresholds under a combined exposure to several pollutants.

In this study the exceedance of WHO guideline values are used as an indicator for air quality and the corresponding effects on human health. As gridboxes in the $\mathrm{REMO}_{\mathtt{chem}}$ simulation are large compared to pollution patterns inside megacities, horizontal gradients can exist with higher extremes than those present in the simulated trace gas concentrations.

The threshold for ozone recommended by the WHO is a concentration of $100\,\mu\mathrm{g/\,m^3}$ as an eight hour mean value (WHO, 2006). The value of $100\,\mu\mathrm{g/\,m^3}$ of ozone corresponds to approximately 50 ppbv at a pressure of 1024 hPa and a temperature of 20° C. The number of days at which the WHO guideline for ozone is exceeded in the $\mathrm{REMO}_{\mathtt{chem}}$ simulation in a specific gridbox is plotted in Figure 5.3 for the month of April and October 2000.

In April 2000 WHO air quality guidelines for ozone are exceeded on several days mainly in two regions of South America. In the north-western part of South America, in the coastal regions of western Venezuela, Bolivia and Ecuador, guideline values for ozone are exceeded in up to 20 days. In the south-eastern part of South America, in the coastal region where São Paulo and Rio de Janeiro are located, the number of days in which ozone concentrations surpass $100\,\mu\mathrm{g/\,m^3}$ in an eight hour mean lie between 10 and 15 days. Around Belo Horizonte, the WHO guidelines are exceeded in between one and five days. This is also the case for gridboxes close to Buenos Aires although in the gridboxes where the city itself is located, the threshold is not exceeded.

In October, WHO air quality guidelines are exceeded in regions similar to those in April. In the area around São Paulo and Rio de Janeiro the number of days in which air quality guidelines are exceeded is slightly increased. Additionally, in the area of high biomass burning activity discussed above (in the southern part of the Amazon

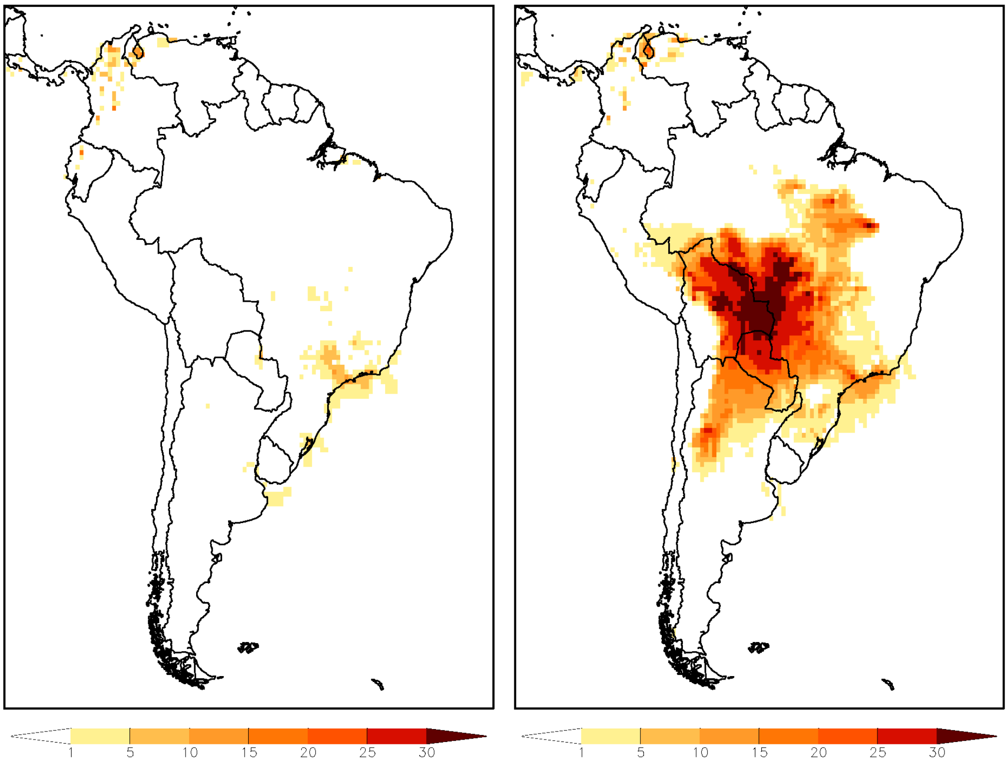

Figure 5.3: Number of days of exceedance of WHO air quality guidelines for ozone. The number of days is plotted in which the WHO air quality guidelines for ozone are exceeded in a gridbox. This number is plotted for April and October 2000 on the left and on the right hand side, respectively.

region and parts of Bolivia and Paraguay), air quality guidelines are exceeded on every day in October in a large area. In great parts of central South America, the WHO guideline values for ozone are exceeded in more than half of the month.

Comparing simulated air quality conditions in April and October, megacity regions show similar pollution patterns with an increased number of days in which the WHO guidelines for ozone are exceeded in October. In central South America, air quality conditions differ significantly between the two months. In the biomass burning season (October) air quality guidelines are exceeded in regions in which there is nearly no day of exceedance in April. This is related to biomass burning in central South America in October and the resulting comparatively high ozone concentrations discussed above.

WHO air quality guidelines can also be exceeded in areas in which the monthly mean ozone concentration is relatively low. This is for example the case for the region around Buenos Aires (cf. Figure 5.2 and Figure 5.3). It indicates that pollution peak periods exist in those areas. During these periods, the ozone concentration is exceptionally high while monthly mean ozone concentrations are rather low.

5.2.2 Regional Air Quality Impact of Megacities and Biomass Burning

In this section the relative impact of megacity emissions and emissions emanating from biomass burning on air quality is assessed. The reference run $\mathrm{R}_{\mathrm{reference}}$ is used together with the two sensitivity runs $\mathrm{R}_{\mathrm{decreased\,MCs}}$ and $\mathrm{R}_{\mathrm{no\,fires}}$ to calculate the relative impact measures $I_{\mathrm{O}_3}^{\mathrm{MCs}}$ and $I_{\mathrm{O}_3}^{\mathrm{fires}}$ described in Section 5.1.2.

Monthly Mean Impact of Megacity Emissions

The monthly mean relative impact of megacity emissions on ozone concentrations is shown in Figure 5.4 for the months of April and October 2000. The region with a monthly mean $I_{\mathrm{O}_3}^{\mathrm{MCs}}$ of more than one percent covers large parts of southern Brazil, Paraguay, Uruguay and northern Argentina in April and October 2000. Around 200 km north and south of Santiago de Chile a monthly mean $I_{\mathrm{O}_3}^{\mathrm{MCs}}$ of more than one percent is simulated. This is also the case along the west coast of South America, north of Santiago de Chile up to northern Peru. Also the region around Bogotá and north-western Venezuela shows a mean relative impact of megacity emissions of more

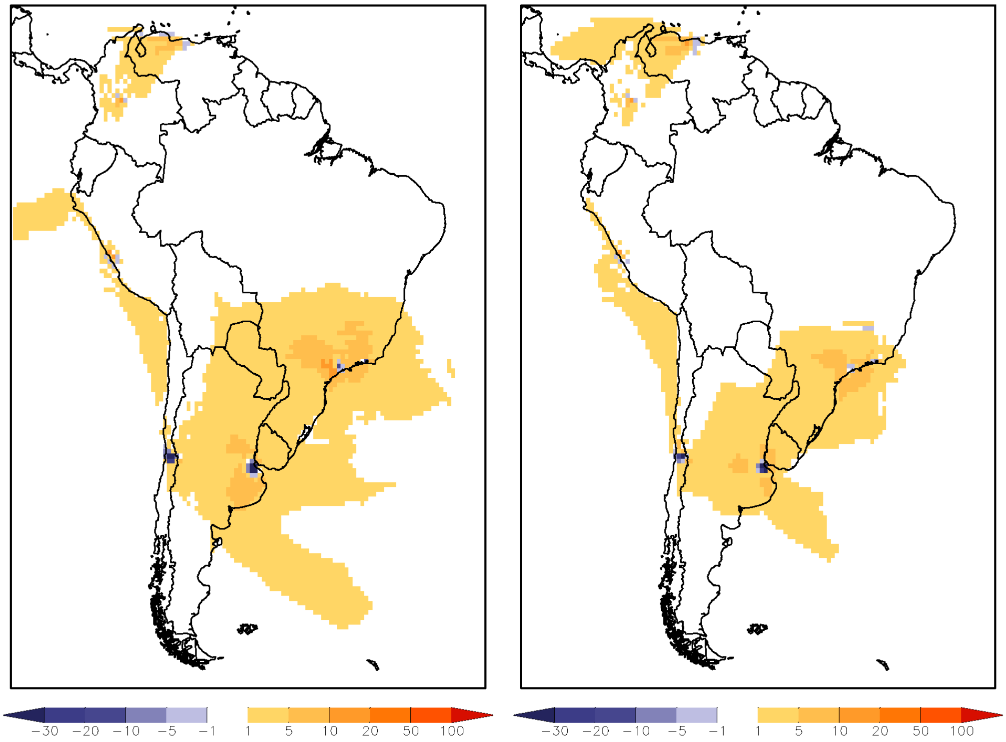

Figure 5.4: Relative impact of megacities on ozone concentrations. Simulated monthly mean impact of South American megacities on ozone concentrations ($I_{O_3}^{MCs}$) is plotted in [%] for the lowest model level for April and October 2000 on the left and on the right hand side, respectively.

than one percent. In regions around Buenos Aires and São Paulo, monthly mean $I_{\mathrm{O}_3}^{\mathrm{MCs}}$ lies between 5 %-10 % in large areas.

In the megacities themselves and in some adjacent gridboxes, $I_{\mathrm{O}_3}^{\mathrm{MCs}}$ shows negative values. Lowest relative impact can be observed in Santiago de Chile and Buenos Aires, where $I_{\mathrm{O}_3}^{\mathrm{MCs}}$ lies partly below -30 % in April and October 2000. In April, São Paulo and Rio de Janeiro show negative $I_{\mathrm{O}_3}^{\mathrm{MCs}}$ down to between -10 % to -20 % in a gridbox. In October, negative $I_{\mathrm{O}_3}^{\mathrm{MCs}}$ reach down to between -1 % to -5 % in São Paulo and between -5 % and -10 % in Rio de Janeiro.

Monthly mean relative impact of megacities shows similar patterns in April and October. The order of magnitude of the affected areas is the same in both months. Different shapes of impact areas represent predominant wind directions. Along the west coast of South America, north of Santiago de Chile, pollutants from Santiago de Chile are transported by coastal winds up to Peru. Emissions from Buenos Aires are transported over the southern south Atlantic Ocean. Mean $I_{\mathrm{O}_3}^{\mathrm{MCs}}$ fields extend further south in April than in October, indicating steady north-westerly wind directions. The region with a monthly mean $I_{\mathrm{O}_3}^{\mathrm{MCs}}$ around São Paulo, Rio de Janeiro and Belo Horizonte has a slightly larger extent in April than in October. This can be related to a stronger dispersion in the lower levels in April and to a more efficient transport to upper levels in October and to the higher absolute ozone concentrations in October. $I_{\mathrm{O}_3}^{\mathrm{MCs}}$ in the region around Bogotá and Caracas is rather low. This is probably due to effective convective transport in these regions.

Negative $I_{\mathrm{O}_3}^{\mathrm{MCs}}$ can be related to $\mathrm{NO_x}$ titration, which happens close to strong sources of $\mathrm{NO_x}$ in combination with rather low VOC concentrations (cf. Section 1.4). This seems to be the case for the cities of Santiago de Chile and Buenos Aires and to a smaller extent in the case of São Paulo.

Monthly Mean Impact of Biomass Burning Emissions

The monthly mean relative impact of emissions emanating from biomass burning on ozone concentrations ($I_{\mathrm{O}_3}^{\mathrm{fires}}$) is depicted in Figure 5.5 for the simulated months of April and October 2000.

In April, $I_{\mathrm{O}_3}^{\mathrm{fires}}$ lies between 1 % and 5 % in an area east of the Andes range extending from northern Venezuela down to central Argentina following the eastern slope of the Andes range. The width of the area is approximately 1000 km. In smaller areas inside this region, $I_{\mathrm{O}_3}^{\mathrm{fires}}$ values are greater: In a region in central Paraguay, $I_{\mathrm{O}_3}^{\mathrm{fires}}$

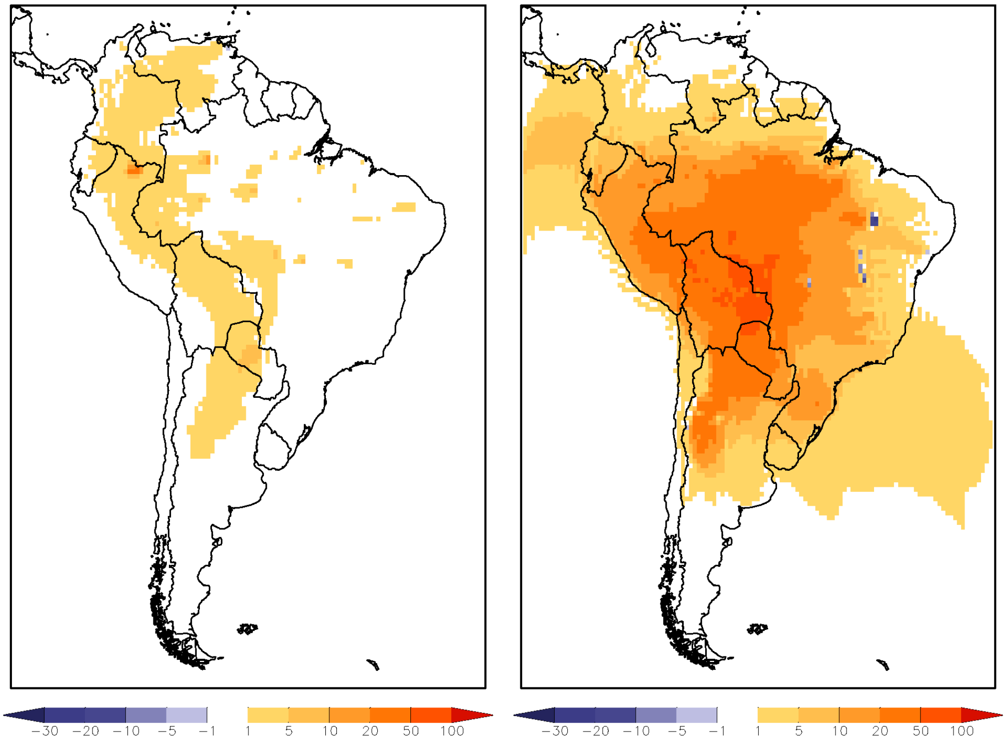

Figure 5.5: Relative impact of biomass burning on ozone concentrations. Simulated monthly mean impact of biomass burning on ozone concentrations ($I_{\mathrm{O}_3}^{\mathrm{fires}}$) is plotted in [%] for the lowest model level for April and October 2000 on the left and on the right hand side, respectively.

values are between 5 % and 10 %, while in a region in northern Peru a region with a relative impact of up to between 20 % and 50 % can be found. In the Amazon region small areas of about ten gridboxes show a relative impact between 1 % and 10 %.

Simulated $I_{\mathrm{O_3}}^{\mathrm{fires}}$ for October 2000 shows maximum values between 50 % and 100 % in a region covering northern Paraguay, eastern Bolivia and parts of an adjacent region in Brazil (see Figure 5.5). A region with a monthly mean relative impact of more than 10 % covers the Amazon region, most parts of central Brazil, Peru, Bolivia, Paraguay and northern Argentina. $I_{\mathrm{O_3}}^{\mathrm{fires}}$ values of more than 1 % are simulated for the whole South American continent except the southern part south of central Argentina and Chile and the coastal regions in the north and in the north-east. In some gridboxes in the eastern part of Brazil, negative $I_{\mathrm{O_3}}^{\mathrm{fires}}$ values of down to between -20 % and -30 % are simulated.

In the region around Santiago de Chile, monthly mean $I_{\mathrm{O_3}}^{\mathrm{fires}}$ is less than 1 % in April and in October. This is also the case for Buenos Aires, Lima, Caracas, São Paulo, Rio de Janeiro and Belo Horizonte in April. In October, $I_{\mathrm{O_3}}^{\mathrm{fires}}$ range between 1 % and 5 % close to Buenos Aires and between 5 % and 10 % in the region of the Brazilian megacities.

The month of April 2000 is characterized by low $I_{\mathrm{O_3}}^{\mathrm{fires}}$ values covering a restricted area in central South America. During this time period, biomass burning emissions are rather low (cf. Section 5.1.1). Wildland fires are sparsely scattered in the Amazon region and on the eastern side of the Andes. Southerly transport along the Andes range is related to the South American low level jet discussed in Section 1.2.

During the biomass burning season in October, wildland fire emissions are much higher than outside the biomass burning season in April leading to elevated $I_{\mathrm{O_3}}^{\mathrm{fires}}$ values in most regions of South America. Elevated $I_{\mathrm{O_3}}^{\mathrm{fires}}$ values can be related to strong biomass burning in this region (cf. Figure 4.1). Negative $I_{\mathrm{O_3}}^{\mathrm{fires}}$ values in the western part of Brazil can be attributed to $\mathrm{NO_x}$ titration due to strong local fire emissions. Nevertheless, coastal areas are affected to a much lesser extent than the interior of the continent. The north-easterly coastal region show monthly mean $I_{\mathrm{O_3}}^{\mathrm{fires}}$ values of less than 1 %. This is due to the predominant north-easterly winds transporting relatively clean air towards the coast. Frequent onshore wind conditions lead to relatively low monthly mean $I_{\mathrm{O_3}}^{\mathrm{fires}}$ values in the region of Rio de Janeiro, São Paulo and Buenos Aires. For Santiago de Chile the predominant wind direction is southerly wind resulting in a negligible relative impact of biomass burning. In Patagonia the predominant westerly winds described in Section 1.2 lead to low air pollution conditions.

Monthly Maximum Impact of Megacity Emissions

The relative impact of an emission source during peak periods is important for air pollution studies. In order to assess which regions are affected to a certain extent by the emissions from megacities and fires during peak periods, the monthly maxima $I_{\mathrm{O_3}}^{\mathrm{MCs}}$ and $I_{\mathrm{O_3}}^{\mathrm{fires}}$ are investigated. They show the upper limit of relative impact, which the respective emissions have on ozone concentrations in the simulated months.

The monthly maximum relative impact of emissions emanating from megacities on ozone concentrations is depicted in Figure 5.6 for the simulated months of April and October 2000.

In April 2000 monthly maxima $I_{\mathrm{O_3}}^{\mathrm{MCs}}$ are between 20 % and 50 % in regions around South American megacities. These regions extend over up to around 10 gridboxes in the case of Caracas, Bogotá, Santiago and Lima, while they reach a regional size of several thousands of kilometers diameter in the case of São Paulo, Rio de Janeiro and Buenos Aires. The region with a maximum relative impact of more than 10 % covers most of northern Argentina and Uruguay as well as large areas over the southern south Atlantic. Additionally, parts of Bolivia and most parts of Paraguay are experiencing a maximum relative impact of more than 10 %. Most of the north-eastern part of South America is not affected by $I_{\mathrm{O_3}}^{\mathrm{MCs}}$ of more than 1 %.

In October 2000 simulated monthly maxima $I_{\mathrm{O_3}}^{\mathrm{MCs}}$ are similar to $I_{\mathrm{O_3}}^{\mathrm{MCs}}$ for April. Differences are peak values of maximum $I_{\mathrm{O_3}}^{\mathrm{MCs}}$ in northern Paraguay of between 50 % and 100 %. This is also the case in an area of a few gridboxes (ca. 10000 km^2) in north-western Argentina. Most parts of north-eastern South America are not affected by $I_{\mathrm{O_3}}^{\mathrm{MCs}}$ of more than 1 %. This includes the Amazon region as well as parts of Peru and Bolivia together with the Nordeste region in Brazil.

During the biomass burning season in October, $I_{\mathrm{O_3}}^{\mathrm{MCs}}$ patterns are rather similar to those of April. The area with a relative impact $I_{\mathrm{O_3}}^{\mathrm{MCs}}$ of more than 1 % extends further into the Amazon region in April than in October. Higher absolute ozone concentrations in October which are caused by biomass burning lead to the comparatively low relative impact of megacity emissions in October in this region. While megacities located in the northern part of South America show a relatively small maximum $I_{\mathrm{O_3}}^{\mathrm{MCs}}$ area in the lowest model level, a comparatively large area around Buenos Aires, São Paulo and Rio de Janeiro can be observed in the simulation. This

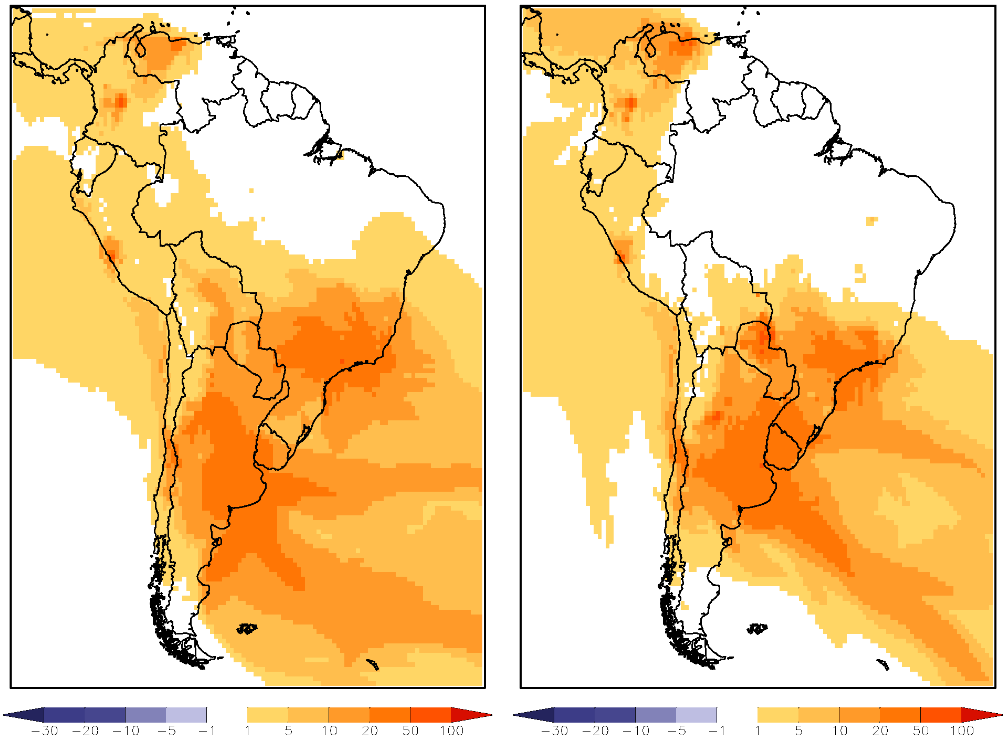

Figure 5.6: Maximum relative impact of megacities on ozone concentrations. Simulated monthly maximum impact of South American megacities on ozone concentrations ($I_{\mathrm{O_3}}^{\mathrm{MCs}}$) is plotted in [%] for the lowest model level for April and October 2000 on the left and on the right hand side, respectively.

is the case for April as well as for October. The results indicate that for the northern megacities convective transport plays a major role in the export of air pollution, while the megacities of Buenos Aires, São Paulo, Rio de Janeiro and to a certain extent also Santiago de Chile show an effective horizontal transport of air pollution in the lowest model level.

Two regions in Paraguay and northern Argentina show elevated maximum $I_{\mathrm{O_3}}^{\mathrm{MCs}}$ values in October in a relatively small area away from the megacities. In these regions, biomass burning is relatively strong (cf. Figure 4.1). Strong fire emissions in combination with emissions from megacities lead to effective ozone production.

During peak periods, large parts of the continent can be affected by emissions from South American megacities. Especially coastal regions are affected as South American megacities are mainly located in coastal areas. The location of peak relative impact on ozone concentrations ($I_{\mathrm{O_3}}^{\mathrm{MCs}}$) close to the megacities matches in some parts the location of exceedance of the WHO air quality index for ozone shown in Figure 5.3. This is, e.g., the case in the region around São Paulo. Thus, emissions from megacities are a major cause of exceedance of air quality thresholds in this regions.

Monthly Maximum Impact of Biomass Burning Emissions

In Figure 5.7 the monthly maximum relative impact of biomass burning emissions on ozone concentrations in the lowest model level is depicted for April and October 2000.

In April 2000 regions with a monthly maximum relative impact $I_{\mathrm{O_3}}^{\mathrm{fires}}$ of more than 5 % are mainly restricted to the interior of the South American continent. Several areas of the size of about 5-10 gridboxes in the Amazon region show $I_{\mathrm{O_3}}^{\mathrm{fires}}$ values of more than 10 %. In an area covering northern Argentina, parts of Paraguay and Brazil $I_{\mathrm{O_3}}^{\mathrm{fires}}$ values between 10 % and 50 % are simulated.

In October 2000, large parts of the continent are experiencing $I_{\mathrm{O_3}}^{\mathrm{fires}}$ values of more than 10 %. In central South America, in a region covering northern Argentina, Paraguay, Bolivia and parts of Peru and Brazil, $I_{\mathrm{O_3}}^{\mathrm{fires}}$ lies between 50 % and 100 %. In the coastal areas close to São Paulo and Rio de Janeiro, $I_{\mathrm{O_3}}^{\mathrm{fires}}$ lies mainly between 20 % and 50 % while the gridboxes associated with Buenos Aires show a maximum $I_{\mathrm{O_3}}^{\mathrm{fires}}$ of between 50 % and 100 %.

The biomass burning season in October leads to a significantly increased monthly

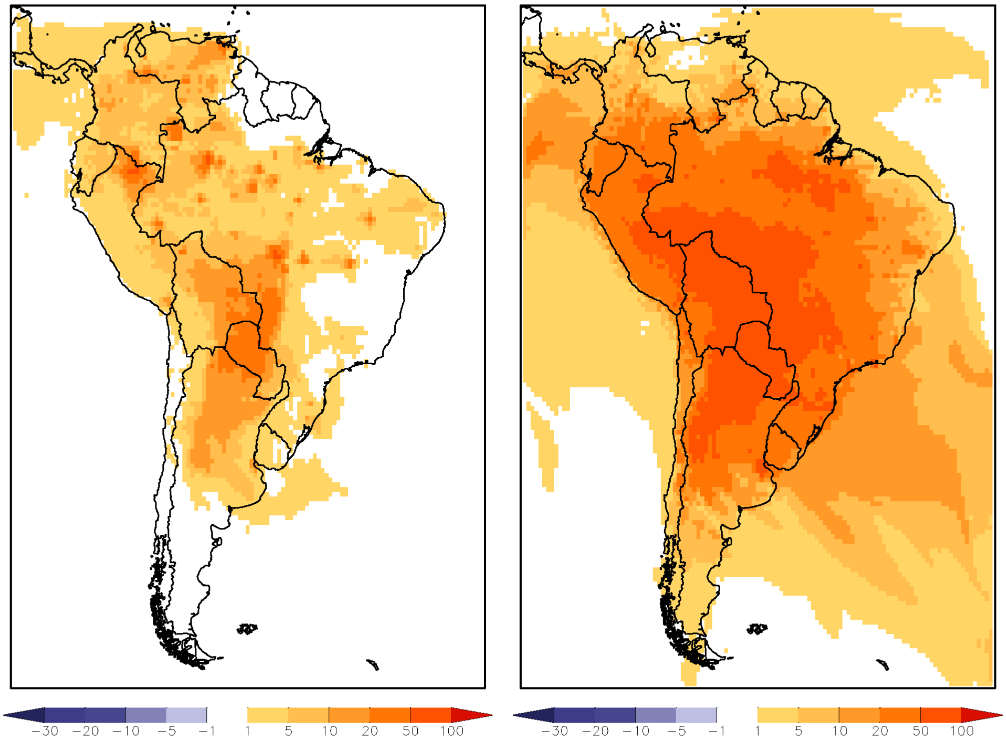

Figure 5.7: Maximum relative impact of biomass burning on ozone concentrations. Simulated monthly maximum impact of biomass burning emissions on ozone concentrations ($I_{O_3}^{\text{fires}}$) is plotted in [%] for the lowest model level for April and October 2000 on the left and on the right hand side, respectively.

maximum relative impact of biomass burning emissions on ozone concentrations. Practically the entire South American continent is affected by biomass burning emissions by more than 5 % for at least one day in October. For remote regions like Patagonia a maximum relative impact of between 1 % and 5 % is simulated. This is also the case for the north-eastern coastal region of South America, where the predominant wind direction is north east.

In central South America, relative impact of biomass burning emissions in October is highest. It is the region with the main fire activity in this month (cf. Figure 4.1). While megacities located in coastal regions are experiencing a very low impact of biomass burning emissions in April, the relative impact is elevated during peak periods in October. In the case of Buenos Aires, the interaction of biomass burning emissions and emissions emanating from the megacity itself lead to a local peak in monthly maximum $I_{\mathrm{O_3}}^{\mathrm{fires}}$ in April as well as in October. This indicates that during peak impact periods of biomass burning emissions, ozone production is more effective compared to the surrounding area.

Yearly Cycle of Mean Relative Impact

As already described in Section 1.3 the amount of emitted tracers can change throughout the year together with their respective location. The location of emissions emanating from megacities is fixed, while the location of wildland fires changes with time. The amount of the emitted trace gases of megacities is rather constant throughout the year, while biomass burning emissions show a distinct seasonality (Section 5.1.1). This influences the monthly mean relative impact of the respective emissions sources.

In this section, the total influenced area and the number of inhabitants influenced by a certain emission source is investigated for different trace species. The concept of impact area introduced in Section 5.1.2 is used with an impact threshold of 10 %. For the calculation of the population impact, the same threshold of 10 % is used.

In Figure 5.8 the monthly mean area with a relative impact from megacities and fires on the concentration of ozone, CO, $\mathrm{NO_x}$ and $\mathrm{NO_y}$ is shown.

Monthly mean relative impact area $A_{\mathrm{NO_y}}^{\mathrm{MCs}}$ increases from $1{\cdot}10^6$ km^2 in January to more than $4{\cdot}10^6$ km^2 in July, before it decreases again to about $1.4{\cdot}10^6$ km^2 in November. $A_{\mathrm{NO_x}}^{\mathrm{MCs}}$ increases from January to July from $0.5{\cdot}10^6$ km^2 to $3{\cdot}10^6$ km^2 in July. It decreases to about $0.7{\cdot}10^6$ km^2 in November. $A_{\mathrm{CO}}^{\mathrm{MCs}}$ values range between

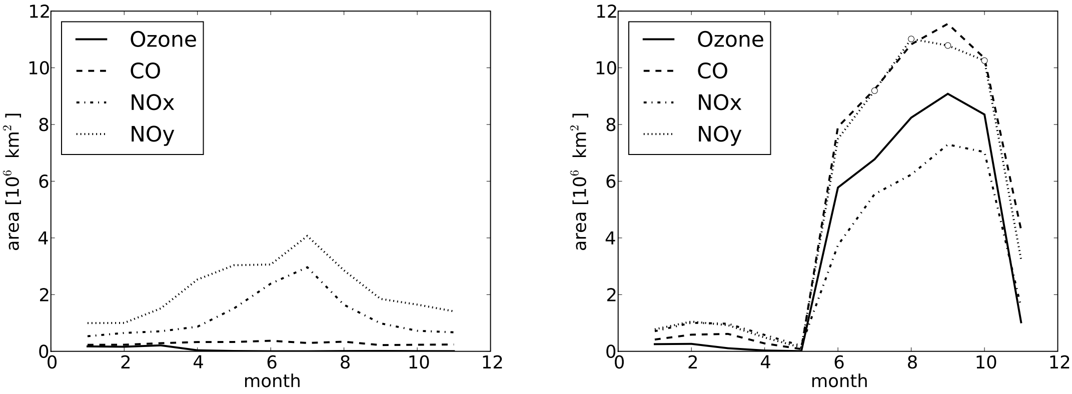

Figure 5.8: Yearly cycle of mean A^{MCs} (10 %) and A^{Fires} (10 %). Simulated yearly cycle of monthly mean relative impact areas A^{MCs} (10 %) and A^{Fires} (10 %) are shown on the left and on the right hand side, respectively. Circles correspond to months in which the impact area is greater than the model domain.

$0.2{\cdot}10^6$ km^2 and $0.4{\cdot}10^6$ km^2 with a peak value in June. $A^{\mathrm{MCs}}_{\mathrm{O_3}}$ values are around $0.2{\cdot}10^6$ km^2 from January to March, while they stay below $0.04{\cdot}10^6$ km^2 during the rest of the year.

From January to May, monthly mean relative impact area for fire emissions for $\mathrm{NO_y}$ and $\mathrm{NO_x}$ ($A^{\mathrm{fires}}_{\mathrm{NO_y}}$ and $A^{\mathrm{fires}}_{\mathrm{NO_x}}$, respectively) stays below $1{\cdot}10^6$ km^2. In this time period, $A^{\mathrm{fires}}_{\mathrm{CO}}$ stays below $0.6{\cdot}10^6$ km^2 while $A^{\mathrm{fires}}_{\mathrm{O_3}}$ does not surpass $0.3{\cdot}10^6$ km^2. From June to October, values for $A^{\mathrm{fires}}_{\mathrm{NO_y}}$ and $A^{\mathrm{fires}}_{\mathrm{CO}}$ range between about $7.5{\cdot}10^6$ km^2 to around $11.5{\cdot}10^6$ km^2 in August and September, respectively. $A^{\mathrm{fires}}_{\mathrm{O_3}}$ values range between around $6{\cdot}10^6$ km^2 and $9{\cdot}10^6$ km^2 while $A^{\mathrm{fires}}_{\mathrm{NO_x}}$ values range between around $4{\cdot}10^6$ km^2 and $7{\cdot}10^6$ km^2 in the same time period.

$A^{\mathrm{MCs}}_{\mathrm{NO_y}}$ and $A^{\mathrm{MCs}}_{\mathrm{NO_x}}$ are increasing from the beginning of the year until the southern hemisphere winter (June, July and August). Afterwards, both impact areas decrease again until they reach values at the end of the year which are comparable to those of January and February. The peak of the impact area in winter is caused by southern South American megacities, especially by Buenos Aires (not shown). Emissions are transported over the southern South Atlantic, where the overall $\mathrm{NO_x}$ and $\mathrm{NO_y}$ concentrations are low due to the lack of local sources. Additionally, relatively low

OH concentrations in winter might lead to a reduced degradation of NO_x. Reduced atmospheric convective activity in winter causes higher NO_x and NO_y concentrations in the lowest model level emanating from the principal emission sources of these species in the region.

In contrast to $A^{\mathrm{MCs}}_{\mathrm{NO_y}}$ and $A^{\mathrm{MCs}}_{\mathrm{NO_x}}$, $A^{\mathrm{MCs}}_{\mathrm{CO}}$ stays rather constant throughout the year at a lower magnitude. This indicates that the influence of megacities is smaller in the case of regional scale air pollution of CO. Transport patterns are the same for all pollutants, therefore also CO is transported towards the southern South Atlantic. With its lifetime of about two months, CO is relatively well mixed in the troposphere This indicates that other emissions sources contribute to CO concentrations in the South Atlantic. CO emissions emanating from megacities are comparatively low, e.g., compared to biomass burning emissions (c.f. Figure 5.1). These factors lead to a relatively small impact of megacity emissions and thus preventing a peak in the impact area in winter.

$A^{\mathrm{MCs}}_{\mathrm{O_3}}$ is small compared to the impact areas of the other species discussed above. In the first three months of the year, $A^{\mathrm{MCs}}_{\mathrm{O_3}}$ has the same size as $A^{\mathrm{MCs}}_{\mathrm{CO}}$, but is one order of magnitude smaller during the rest of the year. In the area where the megacities are located, a negative $I^{\mathrm{MCs}}_{\mathrm{O_3}}$ is simulated (c.f. Figure 5.5). This means that megacity emissions lead to a decrease in ozone concentrations close to the emission source, which is an indication for NO_x titration of ozone. Further downwind, megacity emissions lead to ozone production. Monthly mean relative impact of megacity emissions on ozone concentrations is rather low, while monthly maximum relative impact on ozone concentrations exceeds the relative impact on CO concentrations almost during the whole year (not shown). This is due to the fact that peak concentrations of ozone in an emission plume degrade relatively fast.

Biomass burning impact areas show a seasonal cycle with relatively low values from April to May and relatively high values during the biomass burning season between June and October. This represents the seasonal cycle of the biomass burning emissions shown in Figure 5.1. Also the decrease of emissions in November leads to a corresponding decrease in the total impact area.

During the biomass burning season, the impact area of biomass burning emissions is about three times larger for NO_x and NO_y than the corresponding impact area of megacity emissions. Outside the biomass burning season, impact areas are of about the same magnitude in January to March, while $A^{\mathrm{MCs}}_{\mathrm{NO_y}}$ surpasses $A^{\mathrm{fires}}_{\mathrm{NO_y}}$ largely in April and May. During the biomass burning season $A^{\mathrm{fires}}_{\mathrm{CO}}$ and $A^{\mathrm{fires}}_{\mathrm{O_3}}$ are much larger than $A_{\mathrm{CO}}^{\mathrm{MCs}}$ and $A_{\mathrm{O_3}}^{\mathrm{MCs}}$, respectively. Higher total emissions in a larger area in which the pollutants are emitted lead to the simulated large biomass burning impact areas compared to the simulated megacity impact areas.

The concept of the impact area is useful to investigate the extent of the dispersion of different pollutants from distinct emission sources. In order to investigate to what extent inhabitants of South America are affected, the concept of population impact introduced in Section 5.1.2 is used in the following.

In Figure 5.9 number of inhabitants that experience a monthly mean relative impact of more than 10 % from megacities (P^{MCs} (10 %)) and fires (P^{fires} (10 %)) for concentrations of ozone, CO, $\mathrm{NO_x}$ and $\mathrm{NO_y}$ is shown.

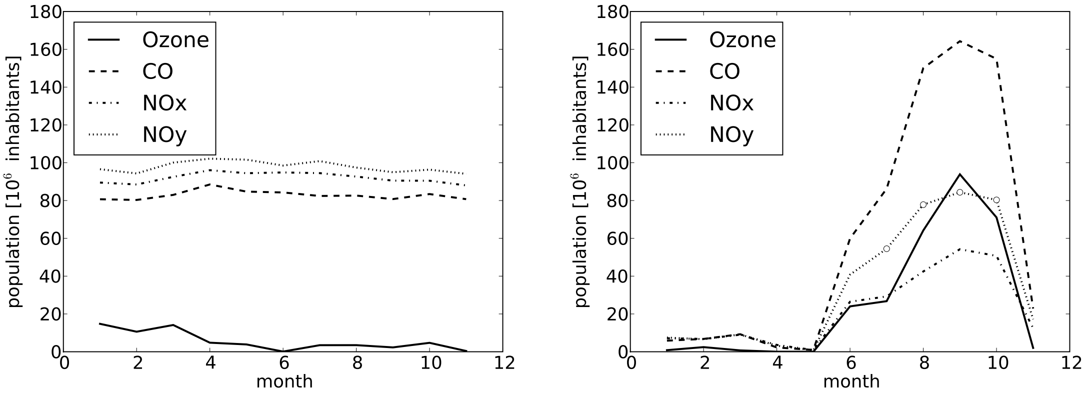

Figure 5.9: Yearly cycle of mean P^{MCs} (10 %) and P^{fires} (10 %). Simulated yearly cycle of monthly mean relative population impact P^{MCs} (10 %) and P^{fires} (10 %) are shown on the left and on the right hand side, respectively. Circles correspond to months in which the impact area is greater than the model domain potentially leading to a higher population impact than shown in the figures.

$P_{\mathrm{NO_y}}^{\mathrm{MCs}}$ values in the entire simulated period from January to November lie around $100 \cdot 10^6$ inhabitants. In the same time period, values for $P_{\mathrm{NO_x}}^{\mathrm{MCs}}$ and $P_{\mathrm{CO}}^{\mathrm{MCs}}$ are around $90 \cdot 10^6$ inhabitants and $83 \cdot 10^6$ inhabitants, respectively. Values for $P_{\mathrm{O_3}}^{\mathrm{MCs}}$ are around $12 \cdot 10^6$ inhabitants from January to March, while they range below $5 \cdot 10^6$ inhabitants during the rest of the year.

Considering the fire emission impact, values for $P^{\mathrm{fires}}_{\mathrm{NO_y}}$, $P^{\mathrm{fires}}_{\mathrm{NO_x}}$ and $P^{\mathrm{fires}}_{\mathrm{CO}}$ are below $10{\cdot}10^6$ inhabitants between January and May. In May, a minimum of around $1{\cdot}10^6$ inhabitants is simulated. For ozone, $P^{\mathrm{fires}}_{\mathrm{O_3}}$ lies below $3{\cdot}10^6$ inhabitants. Between June and October, $P^{\mathrm{fires}}_{\mathrm{NO_y}}$ lies between $40{\cdot}10^6$ inhabitants and $80{\cdot}10^6$ inhabitants, while the values for $P^{\mathrm{fires}}_{\mathrm{NO_x}}$ are between about $25{\cdot}10^6$ inhabitants and $55{\cdot}10^6$ inhabitants. In the same time period, values for $P^{\mathrm{fires}}_{\mathrm{CO}}$ range between $60{\cdot}10^6$ inhabitants and $165{\cdot}10^6$ inhabitants and $P^{\mathrm{fires}}_{\mathrm{O_3}}$ vary from $24{\cdot}10^6$ inhabitants to $94{\cdot}10^6$ inhabitants. Peak P^{fires} are simulated for all species in September.

Monthly mean relative population impact for emissions emanating from megacities is approximately constant throughout the year for CO, $\mathrm{NO_x}$ and $\mathrm{NO_y}$. This is related to the corresponding anthropogenic emissions, which are approximately constant (cf. Figure 5.1). $P^{\mathrm{MCs}}_{\mathrm{O_3}}$ decreases during the biomass burning season which is related to lower ozone concentrations in this period of the year. This is also indicated by a lower $A^{\mathrm{MCs}}_{\mathrm{O_3}}$ (cf. Figure 5.8). Compared to the other pollutants investigated, $P^{\mathrm{MCs}}_{\mathrm{O_3}}$ is comparatively low. This is related to the low ozone concentrations close to the emissions source located directly inside the megacities leading to a negative $A^{\mathrm{MCs}}_{\mathrm{O_3}}$, as discussed before.

Monthly mean relative impact on population from emissions emanating from biomass burning is directly related to the monthly mean amount of biomass burning emissions (cf. Figure 5.1) with a comparatively high population impact during the biomass burning season and low population impact outside the biomass burning season. Outside the biomass burning season, fire emissions are relatively small. They are located in inner-continental areas away from coastal regions with a high population density. Emissions are diluted to a large extent before they reach highly populated areas. During the biomass burning season, even diluted fire emissions have a significant impact in populated areas due to the high amount of emitted trace gases as shown in Figure 5.9.

Although the amount of emitted tracers by biomass burning in the dry season is much larger than the amount of emitted tracers by megacities, population impact has a similar order of magnitude for all considered pollutants except ozone. This is due to the location of the different emission sources: Megacities, which are themselves highly populated, are located in more populated coastal regions, while biomass burning occurs mostly inside the continent, e.g., in the Amazon region. This leads to a similar order of magnitude in population impact during the biomass burning season of the remote fire emission sources compared to the closer megacity emissions source with respect to highly populated areas of South America.

5.2.3 Influence of Transport Patterns on Air Quality

In this section, the influence of transport patterns on air quality is investigated for the two months of April and October 2000 in R 1 and R 2 (cf. Section 5.1.3).

Period Outside the Biomass Burning Season

In order to analyze the influence of transport on air pollution in R 1, wind patterns are considered together with $\mathrm{NO_y}$ concentrations. $\mathrm{NO_y}$ can be seen as a good approximation of a passive tracer. Concentrations of primary pollutants (e.g., CO and $\mathrm{NO_x}$) and concentrations of secondary pollutants (e.g., ozone) are subject to the same transport patterns as the passive tracer, but are additionally modified by chemical processes.

In Figure 5.10, wind speed, wind direction, $\mathrm{NO_y}$ concentration in the lowest model layer and the relative impact of emission sources on $\mathrm{NO_y}$ ($I^{\mathrm{MCs}}_{\mathrm{NO_y}}$ and $I^{\mathrm{fires}}_{\mathrm{NO_y}}$) are shown for the simulated month of April 2000. Wind conditions are shown in order to analyze the dependency of tracer concentrations on transport processes.

Between the 2nd and the 9th of April (in the following referred to as episode $\mathrm{AP1_{R\,1}}$), 10 m wind speed is mainly between 3 and 7 m/s. After the 9th of April, mean wind speed lies mostly between 1 and 3 m/s. Wind direction in Figure 5.10 is defined in degrees deviating from northerly winds. A wind direction of 90°, e.g., corresponds to easterly wind. This direction corresponds to exact downwind conditions for R 1 from São Paulo. It is marked by a dashed black line in the upper right panel in Figure 5.10. During episode $\mathrm{AP1_{R\,1}}$, the wind direction is steady between 100° and 160°. From the 10th to the 18th (referred to as episode $\mathrm{AP2_{R\,1}}$) wind direction is rotating while wind speed is low (below 3 m/s). It stabilizes between the 19th and 22st (referred to as episode $\mathrm{AP3_{R\,1}}$) between 150° and 300°. Between the 23rd and the end of the month (referred to as episode $\mathrm{AP4_{R\,1}}$) wind direction lies mainly between 50° and 140°, crossing several times the 90° wind direction.

The main features of the $\mathrm{NO_y}$ concentration plot in the lower left panel in Figure 5.10 are related to similar time periods as for the description of the wind patterns. In episode $\mathrm{AP1_{R\,1}}$ $\mathrm{NO_y}$ concentrations are between 0.3 and 4 ppbv. They fluctuate between 2 ppbv and 13 ppbv in episode $\mathrm{AP2_{R\,1}}$. Afterwards, during episode $\mathrm{AP3_{R\,1}}$,

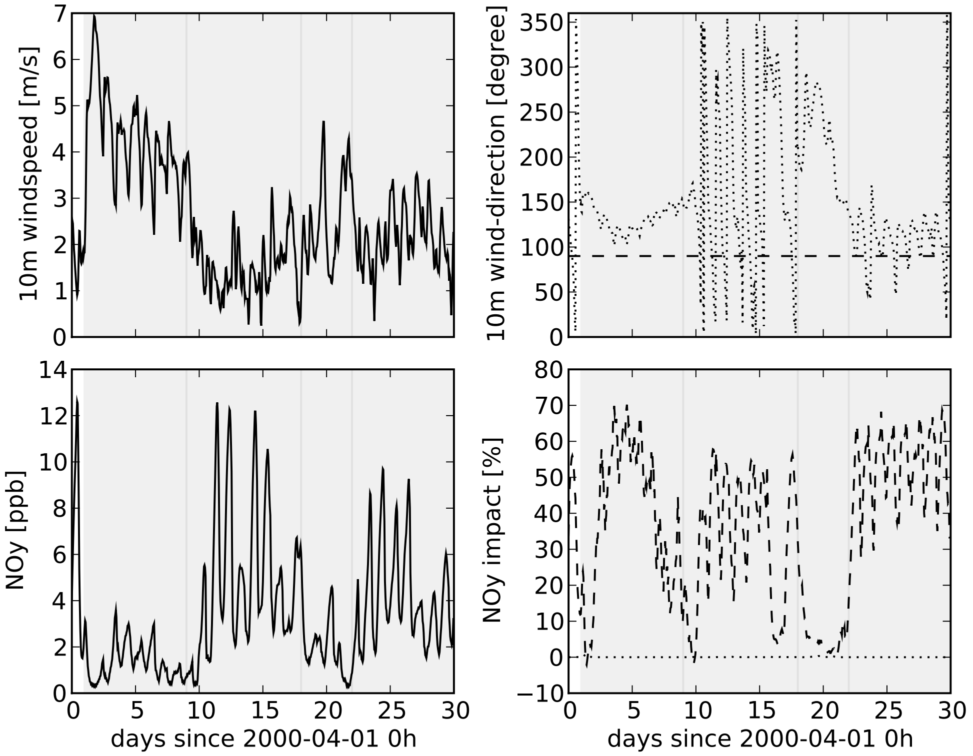

Figure 5.10: Hourly mean wind speed, wind direction, NO_y concentrations and impact on NO_y concentrations for R 1 in April 2000. 10 m wind speed and 10 m wind direction is shown in the upper left and upper right panel, respectively. The dashed line in the upper right panel corresponds to easterly wind, the exact downwind direction from São Paulo. The lower left panel shows the NO_y concentrations in R 1. The lower right panel shows the impact of megacities ($I^{\mathrm{MCs}}_{\mathrm{NO_y}}$ (R 1), dashed line) and the impact of biomass burning emissions ($I^{\mathrm{fires}}_{\mathrm{NO_y}}$ (R 1), dotted line) on NO_y concentrations.

$\mathrm{NO_y}$ concentrations are between 0.3 ppbv and 5 ppbv, before they fluctuate between 1.5 ppbv and 10 ppbv till the end of the month, during episode $\mathrm{AP4_{R\,1}}$.

The impact of the reduction of megacity emissions by 90 % on $\mathrm{NO_y}$ concentrations in R 1 (denoted as $I^{\mathrm{MCs}}_{\mathrm{NO_y}}$ (R 1)) is plotted in Figure 5.10. Maximum $I^{\mathrm{MCs}}_{\mathrm{NO_y}}$ (R 1) of about 70 % can be found on the 4th and 5th of April and in the second half of April in episode $\mathrm{AP4_{R\,1}}$. It is smaller than 10 % only for a few time periods: On the 2nd, on the 10th and on the 17th of April as well as during episode $\mathrm{AP3_{R\,1}}$. The impact of biomass burning emissions on $\mathrm{NO_y}$ concentrations in R 1 (denoted as $I^{\mathrm{fires}}_{\mathrm{NO_y}}$ (R 1)) is smaller than 0.4 % during the whole month.

Air quality in R 1 is mainly determined by São Paulo as it is the closest megacity. The period of episode $\mathrm{AP1_{R\,1}}$ is characterized by relatively low $\mathrm{NO_y}$ concentrations. This can be mainly related to the high wind speed during this period, which leads to a faster dilution and mixing of polluted and unpolluted air. It is unlikely that direct advection of unpolluted air is responsible for the relatively low $\mathrm{NO_y}$ concentrations, as R 1 is strongly influenced by megacities during this time period. This is indicated by $I^{\mathrm{MCs}}_{\mathrm{NO_y}}$ (R 1) which is partly close to 70 % during this time period. The reason is that wind directions are around 90° close to the exact downwind direction from São Paulo.

During the next period, episode $\mathrm{AP2_{R\,1}}$, wind velocities are low compared to the monthly mean. They are mostly below 2 m/s with a few exceptions, where wind speed rises up to 3 m/s for a few hours. The associated wind direction is turning. This leads to regular downwind constellations from São Paulo in R 1. They are directly related in time with peak concentrations in $\mathrm{NO_y}$, which occur mostly within a few hours after exact downwind conditions from São Paulo. This can also be seen in $I^{\mathrm{MCs}}_{\mathrm{NO_y}}$ (R 1) where peak impact corresponds to downwind conditions whereas a minimum $I^{\mathrm{MCs}}_{\mathrm{NO_y}}$ (R 1) corresponds to wind directions away from downwind conditions from São Paulo in R 1. Peak impacts during this time period are around 60 % for downwind conditions and around 20 % for wind directions away from downwind. The latter relatively high impact values away from downwind conditions can be explained by a good horizontal mixing of polluted air in the region around São Paulo under low wind speed conditions.

During episode $\mathrm{AP3_{R\,1}}$ the wind direction is mainly between about 180° and 290°. This corresponds to southerly and north-westerly wind, respectively, and is related to wind directions other than downwind from São Paulo. This can also be seen in $I^{\mathrm{MCs}}_{\mathrm{NO_y}}$ (R 1), which is mostly smaller than 5 % in the considered time period. The corresponding concentrations of NO_y are comparatively low. Even though the time period is hardly influenced by megacities, NO_y concentrations are slightly higher than in the first period discussed. This can be related to NO_y sources other than megacities or biomass burning, like, e.g., anthropogenic emissions from smaller cities in combination with smaller wind speeds than in the first period.

The last episode in April (episode $AP4_{R\,1}$), is characterized by downwind conditions from São Paulo in R 1: Wind direction lies close to easterly wind throughout this time period. Peak NO_y concentrations of up to 10 ppbv are reached during low wind conditions with wind speeds of about 1 m/s. Around these periods, also $I^{MCs}_{NO_y}$ (R 1) reaches a maximum of about 70 %. Lowest NO_y values during episode $AP4_{R\,1}$ correspond to relatively low $I^{MCs}_{NO_y}$ (R 1) of about 30 %.

High relative impact on NO_y concentrations in R 1 ($I^{MCs}_{NO_y}$ (R 1)) can be related to downwind conditions from São Paulo. Downwind conditions together with relatively low wind speeds lead to high NO_y concentrations, while high wind speeds lead to low NO_y concentrations.

In the following the impact of long range transport patterns on tracer concentrations is investigated. The study region R 2 is located in a larger distance away from South American megacities compared to R 1.

In Figure 5.11, wind speed, wind direction, NO_y concentration in the lowest model layer and the relative impact of emission sources on NO_y ($I^{MCs}_{NO_y}$ and $I^{fires}_{NO_y}$) are shown for the simulated month of April 2000.

Wind velocities in R 2 range between 0.1 and 6.4 m/s in April. In the beginning of the month (episode $AP1_{R\,2}$), between the 2nd and the 9th of April, wind velocities range between about 0.2 and 6.4 m/s, while the wind direction in R 2 range between 20° and about 150°. Between the 10th and the 16th of April (episode $AP2_{R\,2}$) the wind direction is turning and frequently corresponding to the exact downwind direction from São Paulo of 45° for a few hours. This is also the case between the 25th and the 30th of April (episode $AP3_{R\,2}$). In both periods, wind velocities range between about 0.2 and 5 m/s.

NO_y concentrations in episode $AP1_{R\,2}$ range between 0.4 and 2.7 ppbv. In episode $AP2_{R\,2}$, NO_y range between 1 and 6 ppbv while the maximum concentrations in episode $AP3_{R\,2}$ is 5 ppbv. The relative impact of megacities in R 2 in episode $AP1_{R\,2}$ ($I^{MCs}_{NO_y}$ (R 2)) is close to zero (e.g., smaller than 0.5 %), except for the first day (2nd of April) where it reaches 2 %. In episode $AP2_{R\,2}$, $I^{MCs}_{NO_y}$ (R 2) reach up to 1.7 %, while

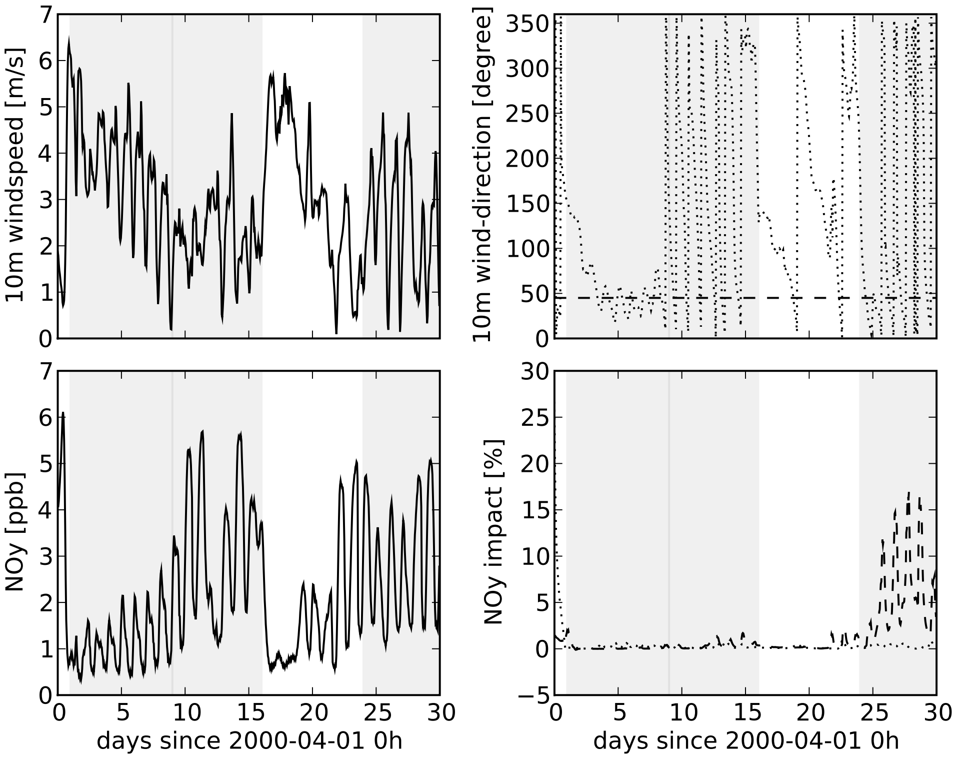

Figure 5.11: Hourly mean wind speed, wind direction, NO_y concentrations and impact on NO_y concentrations for R 2 in April 2000. 10 m wind speed and 10 m wind direction is shown in the upper left and upper right panel, respectively. The dashed line in the upper right panel corresponds to north-easterly wind, the exact downwind direction from São Paulo. The lower left panel shows the NO_y concentrations in R 2. The lower right panel shows the impact of megacities ($I^{MCs}_{NO_y}$ (R 2), dashed line) and the impact of biomass burning emissions ($I^{fires}_{NO_y}$ (R 2), dotted line) on NO_y concentrations.

it is close to 17 % in episode $\mathrm{AP3}_{\mathrm{R\,2}}$. $I^{\mathrm{fires}}_{\mathrm{NO_y}}$ (R 2) is close to zero during the whole month of April, excluding the first day.

Relatively strong winds in episode $\mathrm{AP1}_{\mathrm{R\,2}}$ lead to low $\mathrm{NO_y}$ concentrations in R 2, as air parcels are diluted: They are mixed with advected air from the South Pacific as indicated by relatively steady wind directions around the north-east and by the absence of megacity or fire impact.

The second period considered (episode $\mathrm{AP2}_{\mathrm{R\,2}}$) is characterized by low wind speeds together with turning wind directions. $\mathrm{NO_y}$ concentrations are higher than in episode $\mathrm{AP1}_{\mathrm{R\,2}}$, while $I^{\mathrm{MCs}}_{\mathrm{NO_y}}$ (R 2) is still relatively small indicating that local sources determine the $\mathrm{NO_y}$ concentrations in R 2 in this period: Small episodes of a few hours of exact downwind direction from São Paulo are not sufficient to transport a significant amount of $\mathrm{NO_y}$ into R 2.

In comparison with episode $\mathrm{AP2}_{\mathrm{R\,2}}$, $I^{\mathrm{MCs}}_{\mathrm{NO_y}}$ (R 2) is significantly higher during episode $\mathrm{AP3}_{\mathrm{R\,2}}$, although wind velocities are of about the same magnitude. The relatively constant wind directions close to the exact downwind direction from São Paulo in the beginning of episode $\mathrm{AP3}_{\mathrm{R\,2}}$ indicate that $\mathrm{NO_y}$ is transported to R 2. In contrast to R 1, the wind direction is only an indication for the origin of the air parcels, as the distance to megacities is rather large. The non-zero values of $I^{\mathrm{MCs}}_{\mathrm{NO_y}}$ (R 2) confirm the influence of megacity emissions.

Altogether the air quality in region R 1 close to São Paulo is influenced more frequently and to a greater extent by megacity emissions than the more remote area R 2. Periods of low megacity impact on air quality are possible in R 1 under wind directions away from São Paulo downwind conditions. Despite the large distance to emission sources, $I^{\mathrm{MCs}}_{\mathrm{NO_y}}$ (R 2) surpasses 15 % during single events for several hours.

Period Inside the Biomass Burning Season

In order to investigate the transport patterns of $\mathrm{NO_y}$ during the biomass burning season, concentrations and relative impact of $\mathrm{NO_y}$ are investigated in the following for the month of October 2000. In this month, the biomass burning emissions are on their yearly maximum (cf. Figure 5.1).

In Figure 5.12, wind conditions, $\mathrm{NO_y}$ concentrations and the relative impacts related to megacities and biomass burning emissions of $\mathrm{NO_y}$ are plotted for R 1.

Wind velocity in R 1 in October ranges between about 0.5 and 6 m/s. Wind direction

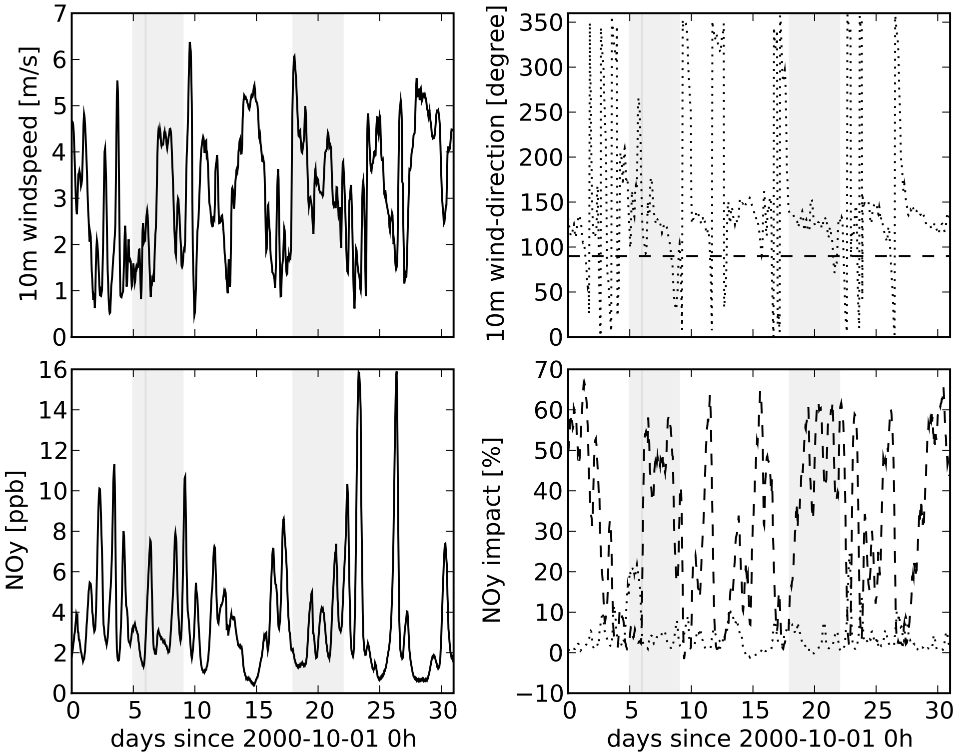

Figure 5.12: Hourly mean wind speed, wind direction, NO_y concentrations and impact on NO_y concentrations for R 1 in October 2000. 10 m wind speed and 10 m wind direction is shown in the upper left and upper right panel, respectively. The dashed line in the upper right panel corresponds to easterly wind, the exact downwind direction from São Paulo. The lower left panel shows the NO_y concentrations in R 1. The lower right panel shows the impact of megacities ($I^{\mathrm{MCs}}_{\mathrm{NO_y}}$ (R 1), dashed line) and the impact of biomass burning emissions ($I^{\mathrm{fires}}_{\mathrm{NO_y}}$ (R 1), dotted line) on NO_y concentrations.

is turning for several periods of a few hours to days. In other periods, wind direction is rather constant: On the 6th of October (episode $\mathrm{OC1_{R\,1}}$), wind velocity is between 1 and 2.5 m/s, with wind directions between about 100° and 270°. Between the 7th and the 9th (episode $\mathrm{OC2_{R\,1}}$), wind direction varies between 180° and 30°, with wind velocities ranging from 1 to 4.5 m/s. In the period between the 19th and 22nd of October (episode $\mathrm{OC3_{R\,1}}$), wind direction is between 70° and 150°, with wind velocities ranging from 2 to 6 m/s.

$\mathrm{NO_y}$ concentrations in episode $\mathrm{OC1_{R\,1}}$ are between 1.5 and 3.5 ppbv. It is characterized by a relative impact of fire emissions $I_{\mathrm{NO_y}}^{\mathrm{fires}}$ (R 1) of about 20 %, while $I_{\mathrm{NO_y}}^{\mathrm{MCs}}$ (R 1) is smaller than 7 %. In episode $\mathrm{OC2_{R\,1}}$, $\mathrm{NO_y}$ concentrations range between 2 and 8 ppbv. $I_{\mathrm{NO_y}}^{\mathrm{MCs}}$ (R 1) is partly close to 60 %, while $I_{\mathrm{NO_y}}^{\mathrm{fires}}$ (R 1) stays below 10 %. In episode $\mathrm{OC3_{R\,1}}$, $\mathrm{NO_y}$ concentrations range between 1.4 and 7.4 ppbv, with $I_{\mathrm{NO_y}}^{\mathrm{fires}}$ (R 1) below 10 %. $I_{\mathrm{NO_y}}^{\mathrm{MCs}}$ (R 1) surpasses 60 % for a few hours.

Low wind speeds in combination with wind directions away from the downwind direction from São Paulo lead to a relative large $I_{\mathrm{NO_y}}^{\mathrm{fires}}$ (R 1) in episode $\mathrm{OC1_{R\,1}}$. Southerly winds transport $\mathrm{NO_y}$ emitted by biomass burning into R 1. In episode $\mathrm{OC2_{R\,1}}$, megacity emissions dominate $\mathrm{NO_y}$ concentrations in R 1, while $I_{\mathrm{NO_y}}^{\mathrm{fires}}$ (R 1) is close to zero. This is related to wind directions close to the downwind direction from São Paulo during episode $\mathrm{OC2_{R\,1}}$. This is also the case in episode $\mathrm{OC3_{R\,1}}$, where high $I_{\mathrm{NO_y}}^{\mathrm{MCs}}$ (R 1) can be observed together with rather low $I_{\mathrm{NO_y}}^{\mathrm{fires}}$ (R 1). Comparatively low absolute $\mathrm{NO_y}$ concentrations are related to high wind speeds leading to a stronger dilution than in the other periods in this month.

Wind conditions, $\mathrm{NO_y}$ concentrations and relative impacts in R 2 related to megacities and biomass burning emissions of $\mathrm{NO_y}$ are plotted for October 2000 in Figure 5.13.

Wind velocities range mainly between 2 and 6 m/s, with a few short periods of about 0.5 m/s. Maximum wind velocities reach up to about 8 m/s. Wind directions are turning with only a few periods of rather steady wind. $\mathrm{NO_y}$ concentrations range from about 0.6 ppbv up to 9.5 ppbv. $I_{\mathrm{NO_y}}^{\mathrm{fires}}$ (R 2) reaches up to 67 %. In several periods of a few hours, $I_{\mathrm{NO_y}}^{\mathrm{fires}}$ (R 2) is smaller than 10 %. $I_{\mathrm{NO_y}}^{\mathrm{MCs}}$ (R 2) surpasses 10 % in only three periods of about half a day.

For analysis, two periods with a specific impact pattern are considered in R 2 for October 2000: On the 5th of October (episode $\mathrm{OC1_{R\,2}}$), $I_{\mathrm{NO_y}}^{\mathrm{MCs}}$ (R 2) reaches up to 20 %, while $I_{\mathrm{NO_y}}^{\mathrm{fires}}$ (R 2) is mostly below 5 %. Absolute values of $\mathrm{NO_y}$ concentrations

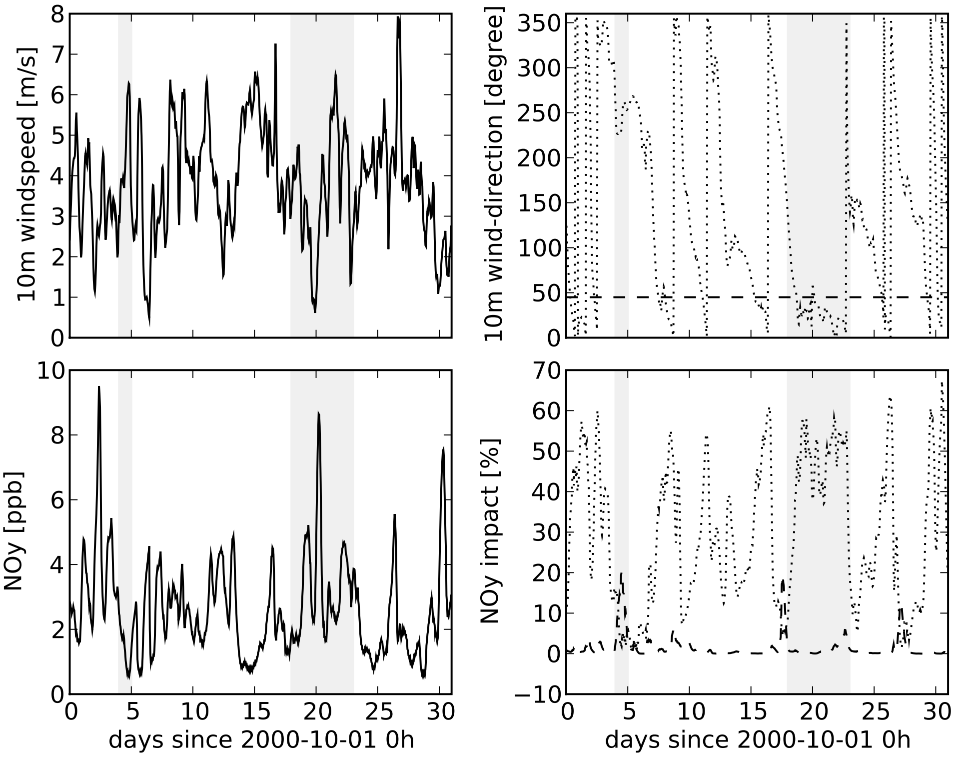

Figure 5.13: Hourly mean wind speed, wind direction, NO_y concentrations and impact on NO_y concentrations for R 2 in October 2000. 10 m wind speed and 10 m wind direction is shown in the upper left and upper right panel, respectively. The dashed line in the upper right panel corresponds to easterly wind, the exact downwind direction from São Paulo. The lower left panel shows the NO_y concentrations in R 2. The lower right panel shows the impact of megacities ($I^{\mathrm{MCs}}_{\mathrm{NO_y}}$ (R 2), dashed line) and the impact of biomass burning emissions ($I^{\mathrm{fires}}_{\mathrm{NO_y}}$ (R 2), dotted line) on NO_y concentrations.

range between 2.5 and 0.5 ppbv. In the second period from the 20th to the 23rd of October 2000 (episode $\mathrm{OC2_{R\,2}}$), $I^{\mathrm{MCs}}_{\mathrm{NO_y}}$ (R 2) is below 6 %, while $I^{\mathrm{fires}}_{\mathrm{NO_y}}$ (R 2) ranges mainly between 37 % and 57 %. Wind direction during episode $\mathrm{OC2_{R\,2}}$ is rather constant between northerly and north-easterly wind.

Predominant south-westerly winds during episode $\mathrm{OC1_{R\,2}}$ lead to transport of emissions from Buenos Aires into R 2. Biomass burning emissions in the area between R 2 and Buenos Aires are rather small. Therefore the $\mathrm{NO_y}$ concentration in advected air parcels is dominated by $\mathrm{NO_y}$ emissions from Buenos Aires during episode $\mathrm{OC1_{R\,2}}$.

During episode $\mathrm{OC2_{R\,2}}$, biomass burning emissions are dominating the $\mathrm{NO_y}$ concentration in R 2, shown by a large value of $I^{\mathrm{fires}}_{\mathrm{NO_y}}$ (R 2). Although the wind direction in R 2 ranges between northerly and north easterly wind and is close to the downwind direction from São Paulo, $I^{\mathrm{MCs}}_{\mathrm{NO_y}}$ (R 2) is rather small. Over the distance between São Paulo and R 2, wind directions are changing (not shown): Wind directions away from the downwind direction lead to dilution of megacity emissions before they can reach R 2.

Altogether, biomass burning emissions are more important for $\mathrm{NO_y}$ concentrations in R 2 than the remote megacity emissions in October 2000. In contrast, megacity emissions dominate $\mathrm{NO_y}$ concentrations in R 1 also during the biomass burning season in October 2000. Under special wind conditions short periods of higher relative impact of biomass burning on $\mathrm{NO_y}$ concentrations are possible.

5.2.4 Ozone Production Regimes

Ozone is a major secondary pollutant in the troposphere (WHO, 2006). The investigation of its concentration and production regimes in the atmosphere is subject to a number of model studies and measurement campaigns (e.g., Trainer et al., 1993; Olszyna et al., 1994; Derwent et al., 1995; Brasseur et al., 1998; Sillman, 1999; Reich et al., 2006; Brasseur et al., 2006). In this section ozone concentrations and production regimes are investigated for the two study regions defined in Section 5.1.3. Different transport patterns investigated in Section 5.2.3 are taken into account.

Ozone concentrations are plotted as a function of megacity impact on $\mathrm{NO_y}$ concentrations in Figure 5.14. The daily cycle of ozone concentrations is not represented in the plots as only ozone concentrations at local noon are taken into account. The plots show ozone concentrations in time periods of relatively high and relatively low megacity emission impact.

In April in R 1, ozone concentrations reach from 20 ppbv to about 65 ppbv for $I_{\mathrm{NO_y}}^{\mathrm{MCs}}$ between 0 % and 68 %. While the range of $I_{\mathrm{NO_y}}^{\mathrm{MCs}}$ is similar in episode $\mathrm{AP1_{R\,1}}$, ozone concentrations are below 30 ppbv. For episode $\mathrm{AP2_{R\,1}}$ and episode $\mathrm{AP4_{R\,1}}$, ozone concentrations are mostly above 30 ppbv, while the $I_{\mathrm{NO_y}}^{\mathrm{MCs}}$ mainly surpasses 40 %. episode $\mathrm{AP3_{R\,1}}$ is characterized by $I_{\mathrm{NO_y}}^{\mathrm{MCs}}$ values between 0 % and 10 % and ozone concentrations between 20 ppbv and 35 ppbv.

In October 2000 in R 1 ozone concentrations range between about 20 ppbv and 70 ppbv with $I_{\mathrm{NO_y}}^{\mathrm{MCs}}$ between 0 % and 65 %. In R 2, $I_{\mathrm{NO_y}}^{\mathrm{MCs}}$ stays mainly below 10 %, while ozone concentrations reach 45 ppbv in April and 62 ppbv in October.

Altogether, no clear correlation between ozone concentrations and $I_{\mathrm{NO_y}}^{\mathrm{MCs}}$ can be derived from Figure 5.14. Nevertheless, some important features can be observed. During episode $\mathrm{AP1_{R\,1}}$, relatively low ozone concentrations, which are in approximation independent of $I_{\mathrm{NO_y}}^{\mathrm{MCs}}$, are related to the strong winds during this period discussed in Section 5.2.3. Relatively high wind velocity lead to a stronger dispersion and a better vertical mixing compared to low wind conditions. During the downwind situations from São Paulo in episode $\mathrm{AP2_{R\,1}}$ and episode $\mathrm{AP4_{R\,1}}$, $I_{\mathrm{NO_y}}^{\mathrm{MCs}}$ as well as ozone concentrations are comparatively high. This is not the case for the wind direction away from the downwind situation in episode $\mathrm{AP3_{R\,1}}$, where $I_{\mathrm{NO_y}}^{\mathrm{MCs}}$ as well as ozone concentrations are comparatively low.

In general, ozone concentrations do not exceed 50 ppbv in April, outside the biomass burning season, when the $I_{\mathrm{NO_y}}^{\mathrm{MCs}}$ is less than 30 %. On the other hand, ozone concentrations are comparatively high in most of the cases of high $I_{\mathrm{NO_y}}^{\mathrm{MCs}}$ values. The latter is also the case for October, while comparatively high ozone concentrations can be observed also for low $I_{\mathrm{NO_y}}^{\mathrm{MCs}}$ values. This indicates that other factors than megacity emissions like, e.g., biomass burning or local emission sources influences the ozone concentrations during this time period.

While absolute ozone concentrations are not completely determined by megacity emissions, the impact of megacity emissions on ozone concentrations and the impact of megacity emissions on $\mathrm{NO_y}$ concentrations is strongly correlated (not shown). This indicates that non-linear effects of ozone production play a minor role in medium and long-range transport.

Trainer et al. (1993) observed a strong correlation between ozone and $\mathrm{NO_y}$ con-

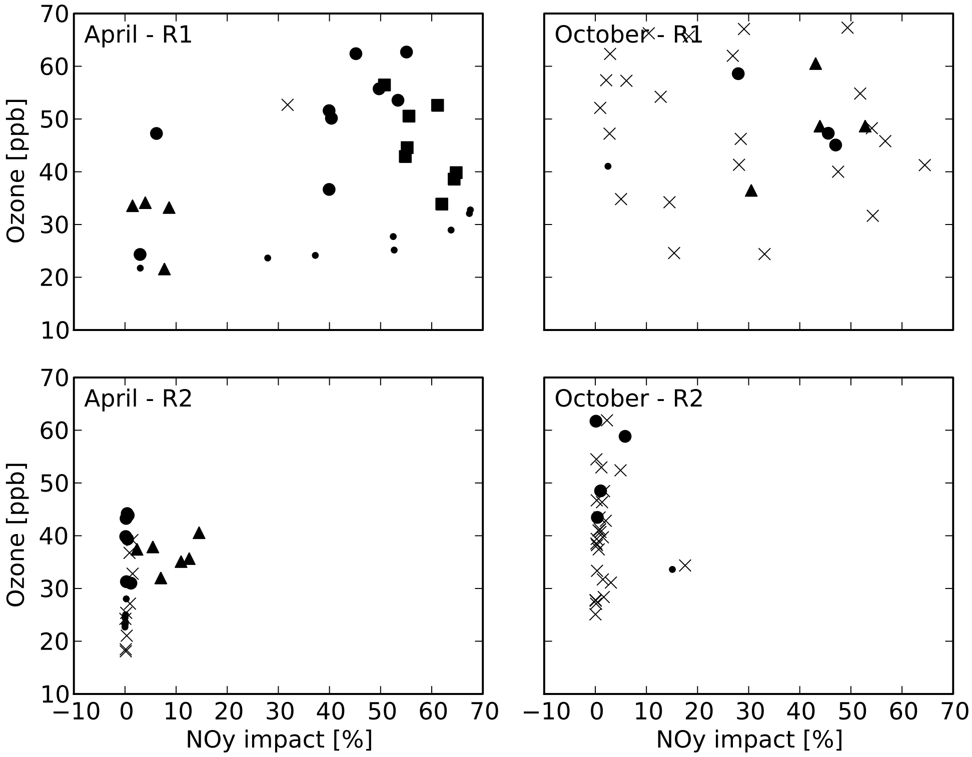

Figure 5.14: Ozone concentrations as a function of megacity impact on NO_y concentrations. Ozone concentrations at local noon are plotted as a function of megacity emission impact on NO_y concentrations for the two study regions R 1 and R 2 and for the two months of April and October 2000. Different marker symbols represent the different time periods of characteristic impact patterns investigated in Section 5.2.3. The small dots correspond to the first time period, the circles to the second, the triangles to the third and the squares to the fourth time period of the respective month. Data not belonging to a time period is marked with a cross.

centrations at rural sites in photochemically aged air. They related the correlation of elevated ozone to elevated NO_y concentrations to the importance which anthropogenic emissions - especially oxides of nitrogen - play for rural ozone production. This correlation can also be observed in $REMO_{\texttt{chem}}$ simulations for R 1 and R 2 (not shown). As discussed before, not all elevated ozone situations can be directly related to megacity emissions. They are likely to be related to other anthropogenic emission sources of nitrogen oxides, like, e.g., emissions emanating from smaller cities in the proximity of R 1 and R 2.

The two main anthropogenic precursors of ozone are NO_x and VOCs. In general, two different ozone production regimes can be distinguished. During *NO_x-sensitive* ozone production, ozone concentrations increase with increasing NO_x concentrations and are affected to a much lesser extent by VOC concentrations. In the *VOC-sensitive* regime, ozone concentrations increase with increasing VOC concentrations, whereas they decrease with increasing NO_x concentrations (see, e.g., Sillman, 1999).

In general, ozone production close to anthropogenic emissions sources tend to be VOC-sensitive as the amount of emitted NO_x is rather high compared to emitted VOC in a freshly emitted plume. Further downwind, NO_x reacts away more rapidly than VOC leading to NO_x-sensitive ozone production.

Several major factors influence the NO_x-VOC-sensitivity of ozone production regime according to Sillman (1999). The VOC/NO_x ratio is used to determine the sensitivity of ozone production regimes, but has some deficiencies leading to erroneous simulated sensitivity by photochemical models (see, e.g., Milford et al., 1994). Reactivity of the VOC-mix with OH plays an important role as well as VOC emitted by natural sources such as isoprene emissions from plants. Photochemical aging is related to the transition from VOC-sensitive to NO_x-sensitive ozone production with increasing distance to the emission source discussed above. Meteorological conditions that affect the oxidation capacity of the atmosphere such as solar actinic flux, cloud cover and water vapor also influence ozone production together with its NO_x-VOC-sensitivity. Increased atmospheric mixing and dilution tends to generate NO_x-sensitive chemistry (cf. Sistla et al., 1996).

In order to investigate the NO_x-VOC-sensitivity of ozone production there are several indicators and indicator ratios, which are widely used together with observations. Milford et al. (1994) suggested to use total reactive nitrogen (NO_y) as an indicator for ozone production regimes. They found that under conditions with low NO_y concentration of less than 10 ppbv, NO_x-sensitive ozone production is likely.

Low NO_y concentrations are an indicator for low precursor concentrations. Removal processes of NO_y such as wet deposition are factors of uncertainty, using this indicator, as a considerable amount of precursors would not be considered as NO_y is removed from the atmosphere. In this study, the regions R 1 and R 2, both show mainly NO_y concentrations below this threshold indicating predominant NO_x-sensitive ozone production inside as well as outside the biomass burning season (not shown).

According to Sillman (1995), the ratio $O_3/(NO_y - NO_x) = O_3/NO_z$ can be used an indicator for NO_x and VOC-sensitive ozone production regimes. For a ratio of $O_3/NO_z < 7$ VOC-sensitive ozone production is likely to occur. In the case of the study regions R 1 and R 2, this ratio is always above 10, also indicating NO_x-sensitive ozone production (not shown).

5.3 Conclusions

In this chapter, the impact of pollutants emitted by different emission sources and their impact on the regional air quality are investigated. April and October represent two months outside and inside the biomass burning season, respectively. Outside the biomass burning season in southern hemisphere summer, relatively low ozone concentrations are simulated compared to southern hemisphere winter, in which the biomass burning season is located. Slightly elevated ozone concentrations in coastal areas indicate the influence of megacities on elevated ozone concentrations in summer as well as in winter.

During the biomass burning season in October, ozone concentrations are significantly higher than in April in most parts of South America. In central South America, in the inner continent, ozone concentrations are highest. This can be related to biomass burning emissions in this area and to more stable atmospheric conditions in winter time, slowing down pollutant dispersion.

$REMO_{\texttt{chem}}$ model simulations show that the area in which ozone concentrations are affected by emissions emanating from megacities in a monthly mean is similar for April and October 2000. In the cities of Santiago de Chile, Buenos Aires and São Paulo, a negative impact on ozone concentrations is simulated. This can be related to NO_x titration of ozone due to high local NO_x concentrations.

Simulated monthly mean impact of biomass burning emissions on ozone concentrations are restricted to the inner continent of South America. They affect large parts of the continental ozone concentrations by at least 1 % except for Patagonia and the north-eastern coast, where the predominant on-shore wind direction prohibits an impact of South American emission sources.

The investigation of the monthly maximum impact on ozone concentrations shows that the impact of megacity emissions on ozone concentrations can reach more than 20 % on a regional scale of several thousand kilometers. Largest impact areas are simulated for São Paulo, Rio de Janeiro and Buenos Aires.

In contrast to the megacity emissions, the maximum impact on ozone concentrations of biomass burning is mostly less than 5 % in coastal regions in April, while it reaches more than 20 % in October in many areas.

The patterns of the impact regions and the yearly cycle with pronounced seasonality in the case of the biomass burning leads to a rather small impact of biomass burning on the population outside the biomass burning season. Inside the biomass burning season, the same order of magnitude of people are affected by biomass burning emissions as by emissions emanating from megacities for the investigated species, except for ozone. The impact on population of megacity emissions due to ozone concentrations is rather low. This is due to NO_x titration of ozone inside the megacities, which leads to ozone production away from the emission source region where the population density is lower.

The investigation of the two impact areas R 1 and R 2 for transport patterns of a passive tracer shows that the region relatively close to São Paulo is frequently perturbed by megacity emissions in April as well as in October. This is less frequent and to a lesser amount the case for the more remote region of R 2 in April. For R 1, high impact patterns can be related to downwind conditions from São Paulo and to rather low wind velocities. This is not possible to the same extent for the more remote area R 2.

While R 1 is still dominated by megacity emissions, during the biomass burning season represented by the month of October, this is not the case for R 2. In this region, biomass burning emissions determine the air quality during most of the month, while megacity emissions only play a minor role during episodes of a few days.

While there is no clear correlation between ozone concentrations and the impact of megacity emissions on NO_y concentrations, several factors indicate that the influence of megacity emissions favors high ozone concentrations. This can be observed in the simulation under conditions of comparatively low wind speed outside the biomass burning season for R 1. Inside the biomass burning season, a high impact of megacity emissions coincide with high ozone concentrations. During this period high ozone concentrations are also simulated for low impact of megacity emissions indicating other sources of ozone precursors in R 1. In the rather remote region R 2, megacity impact on ozone concentrations is comparatively low. Nevertheless, an elevated impact of megacity emissions is related to slightly elevated ozone concentrations. Several indicators suggest predominant NO_x-sensitive ozone production in R 1 and R 2 in the considered months. This can be explained by the comparatively long distance to megacities, which represent strong emission sources of NO_x in the region.

6 Conclusion and Outlook

6.1 Conclusions

In the frame of this study, online-chemistry and tracer transport are successfully implemented in the newest operational version of the regional climate model REMO, which contains improved meteorological mechanisms in comparison with older REMO versions. It yields realistic trace gas concentrations when compared to horizontal total column patterns obtained from satellite observations and when compared to trace gas profiles from a measurement campaign.

Vertical convective tracer transport is improved compared to the standard convection mechanism. The latter showed unphysical oscillation patterns under strong convection conditions. The new convection mechanism for trace gases now yields realistic vertical profiles in the entire region used in this study, comprising the entire South American continent.

Simulations indicate that in regions, where CO is predominantly produced by local emission sources, cloudiness leads to higher CO concentrations. The common procedure of averaging CO satellite retrievals over larger areas therefore leads to a potential systematic underestimation of CO concentrations when comparing with model data without accounting for the effect of cloudy pixels.

In the frame of this study, the research questions verbalized in Section 1.5 are answered. This is shortly summarized in the following:

To what extent do emissions from megacities and biomass burning influence the air quality in South America?

The impact of emissions emanating from megacities and biomass burning is investigated by assessing the effects of an artificial reduction of megacity emissions by 90 % and of a 100 % reduction of emissions emanating from biomass burning. Megacity emissions show a dispersion on a continental scale (about $1000 \times 1000\,\mathrm{km}^2$), when considering the area in which the reduction of megacity emissions leads to differences in local trace gas concentrations of more than 1 %. While the spatial extent of the impact of megacity emissions is constant throughout the year, the spatial extent of biomass burning emission impact shows a strong seasonality with a peak extent in southern hemisphere winter which corresponds to the main biomass burning season. In this time period, the area affected by biomass burning emissions strongly exceeds the area influenced by megacity emissions. Outside the biomass burning season, the area of megacity impact extends to about the same order of magnitude as the area influenced by biomass burning emission for the pollutants ozone, CO and NO_x.

While the emissions from megacities affect mainly coastal areas with considerable transport over the oceans (e.g., from Buenos Aires and São Paulo), biomass burning emissions outside the biomass burning season affect trace gas concentrations of the inner continent (which is less populated than coastal areas). Nevertheless, inside the biomass burning season, almost the entire South American continent is affected. This is also represented in the exceedance of WHO air quality indices, e.g., for ozone. They are exceeded in the areas of biomass burning emission impact and close to megacities, especially São Paulo.

How much is the population affected by the different emission sources?

Because population density is highest in coastal areas, population impact of megacities (mainly located in coastal areas) is particularly high compared to biomass burning outside the biomass burning season. Population impact of megacity emissions is of about the same order of magnitude inside the biomass burning season, although total emissions from biomass burning are much higher than those of megacities in South America in this period. During this period, e.g., about 80 million people are affected by CO emissions emanating from megacities, while the impact of biomass burning emissions affect about 170 million people during the peak period in October. Thus, considering the mean impact on population throughout the year, prohibition of biomass burning during the biomass burning season has about the same effect as a reduction of South American megacity emissions by 90 %.

What are the dominant ozone production regimes in the outflow of pollutants from the megacities?

Two study regions are investigated. The first region is located in 700 km distance from São Paulo, while the second region is located in about mid-distance between São Paulo and Buenos Aires (at a distance of about 1100 km). The investigation of an artificial passive trace species (NO_y) shows a predominant influence of megacity emissions in the first study region in southern hemisphere winter as well as in summer of up to 70 %. High wind speeds are related with low absolute concentrations of NO_y, while megacity impact stays high. In the more remote study region, impact of emissions of more than 50 % is only simulated for biomass burning emissions during the biomass burning season, while the impact of megacity emissions can reach up to 20 % during periods of up to a few days.

While ozone concentrations do not show a strong correlation with the impact of megacity emissions on NO_y concentrations, ozone concentrations and NO_y concentrations are highly correlated in the two study regions. This indicates that in addition to the megacities, other emission sources dominate ozone production during the investigated time periods. Indicator values in the two study regions suggest that ozone production is predominantly NO_x limited. This can be explained by the comparatively long distance between the study regions and the megacities, which represent strong emission sources of NO_x in the region.

In the context of this study, a sensitivity run in which emissions from megacities are distributed over an area four times the size of the original megacities is performed to investigate the secondary pollutant production in the emission plume. First results show that differences in ozone concentrations are small in the two study regions (not shown). As the experiment is not in the center of this thesis, future studies will further investigate the effect of dilution of urban emissions on the formation of secondary pollutants downwind of the sources.

6.2 Outlook

It is possible to further improve $\text{REMO}_{\texttt{chem}}$ by implementing the improved vertical convective transport to meteorological prognostic variables like, e.g., specific humidity for which the standard convection scheme is used. Nevertheless, the effect of the modified convection scheme is expected to be smaller due to the relatively high abundance of specific humidity in the atmosphere compared to other trace gases.

A further assessment of the influence of fire management and emission reduction policies on air quality would give an indication of possible improvements in air quality in big population centers of South America. Additional simulations for periods other than the year 2000 will give more robust statistical information.

In order to assess in more detail the air quality in megacities, a further downscaling around an example megacity like, e.g., São Paulo will likely improve simulated trace gas concentrations in this region. Peak emissions in smaller areas than in the 50x50 km^2 sized gridboxes used in this study will better represent megacity emissions, leading to a more realistic simulation of peak pollution periods in the megacity region (cf. Poppe et al., 1998). This will allow a reasonable comparison of pollutant measurements inside and nearby the megacity agglomeration.

In the future, online-coupling of the chemical mechanism to an aerosol module, which has recently been implemented in REMO, is planned as well as the implementation of the feedback of chemical mechanisms on meteorological processes. This will make it possible to investigate feedback processes between aerosols and trace gas concentrations and vice-versa. Additionally, the combined feedback of aerosols and chemistry on meteorological processes will be investigated.

In order to evaluate and further improve regional climate models including atmospheric chemistry, in situ and satellite based measurements are needed. While satellite data is available globally, in situ measurements are relatively sparse in South America. Long term measurements of trace gases such as ozone, CO, NO_x and VOCs together with the meteorological conditions in regions of main megacity emission outflow are necessary to investigate air pollution transport and ozone production regimes as it is done for the two study regions in this work.

References

Achberger, C., M.-L. Linderson and D. Chen (2003). Performance of the Rossby Centre regional atmospheric model in Southern Sweden: comparison of simulated and observed precipitation. *Theoretical and Applied Climatology*, **76**(3), 219–234. doi: 0.1007/s00704-003-0015-6.

Arakawa, A. and V. Lamb (1977). Computational design of the basic dynamical processes of the UCLA general circulation model. *Methods in Computational Physics*, **17**, 173–265.

Arellano, J., Avelino F., P. S. Kasibhatla, L. Giglio, G. R. van der Werf and J. T. Randerson (2004). Top-down estimates of global CO sources using MOPITT measurements. *Geophysical Research Letters*, **31**, –.

Asselin, R. (1972). Frequency filter for time integrations. *Monthly Weather Review*, **100**, 487–490.

Baehr, J., H. Schlager, H. Ziereis, P. Stock, P. van Velthoven, R. Busen, J. Strom and U. Schumann (2003). Aircraft observations of NO, NOy, CO, and O-3 in the upper troposphere from 60 degrees N to 60 degrees S - Interhemispheric differences at mitlatitudes. *Geophysical Research Letters*, **30**(11), 1598. doi: 0.1029/2003GL016935.

Beirle, S., U. Platt, M. Wenig and T. Wagner (2003). Weekly cycle of NO2 by GOME measurements: a signature of anthropogenic sources. *Atmospheric Chemistry and Physics*, **3**, 2225–2232.

Betts, A. K., J. H. Ball, P. Viterbo, A. G. Dai and J. Marengo (2005). Hydrometeorology of the Amazon in ERA-40. *Journal of Hydrometeorology*, **6**(5), 764–774.

Bian, H., M. Chin, S. Kawa, B. Duncan, A. Arellano and P. Kasibhatla (2007). Sensitivity of global CO simulations to uncertainties in biomass burning sources. *Journal of Geophysical Research-Planets*, **112**(D23), D23308–1–17. doi: 0.1029/2006JD008376.

Bouwman, A. F., L. J. M. Boumans and N. H. Batjes (2002). Estimation of global NH3 volatilization loss from synthetic fertilizers and animal manure applied to arable lands and grasslands. *Global Biogeochemical Cycles*, **16**(2), 1024.

Brasseur, G. P., D. A. Hauglustaine, S. Walters, P. J. Rasch, J. F. Muller, C. Granier and X. X. Tie (1998). MOZART, a global chemical transport model for ozone and related chemical tracers 1. Model description. *Journal of Geophysical Research-Atmospheres*, **103**(D21), 28265–28289.

Brasseur, G. P., J. J. Orlando and G. S. Tyndall (1999). Atmospheric Chemistry and Global Change. Oxford University Press.

Brasseur, G. P., M. Schultz, C. Granier, M. Saunois, T. Diehl, M. Botzet, E. Roeckner and S. Walters (2006). Impact of climate change on the future chemical composition of the global troposphere. *Journal of Climate*, **19**(16), 3932–3951.

Bremer, H., J. Kar, J. R. Drummond, F. Nichitu, J. S. Zou, J. Liu, J. C. Gille, M. N. Deeter, G. Francis, D. Ziskin and J. Warner (2004). Spatial and temporal variation of MOPITT CO in Africa and South America: A comparison with SHADOZ ozone and MODIS aerosol. *Journal of Geophysical Research-Atmospheres*, **109**(D12), D12304. doi: 0.1029/2003JD004234.

Brinkop, S. and R. Sausen (1997). A Finite Difference Approximation For Convective Transports Which Maintains Positive Tracer Concentrations. *Beitraege zur Physik der Atmosphaere*, **70**(3), 245—-248.

Chang, J., R. Brost, I. Isaksen, S. Madronich, P. Middleton, W. Stockwell and C. Walcek (1987). A 3-Dimensional Eulerian Acid Deposition Model - Physical Concepts And Formulation. *Journal Of Geophysical Research-Atmospheres*, **92**(D12), 14681–14700.

Collins, W. D., C. M. Bitz, M. L. Blackmon, G. B. Bonan, C. S. Bretherton, J. A. Carton, P. Chang, S. C. Doney, J. J. Hack, T. B. Henderson, J. T. Kiehl, W. G. Large, D. S. McKenna, B. D. Santer and R. D. Smith (2006). The Community Climate System Model version 3 (CCSM3). *Journal Of Climate*, **19**(11), 2122–2143.

Crawford, J. H., C. L. Heald, H. E. Fuelberg, D. M. Morse, G. W. Sachse, L. K. Emmons, J. C. Gille, D. P. Edward, M. N. Deeter, G. Chen, J. R. Olson, V. S. Connors, C. Kittaka and A. J. Hamlin (2004). Relationship between Measurements of Pollution in the Troposphere (MOPITT) and in situ observations of CO based on a large-scale feature sampled during TRACE-P. *Journal of Geophysical Research-Atmospheres*, **109**(D15), D15S04. doi: 0.1029/2003JD004308.

Davies, H. C. (1976). A lateral boundary formulation for multi-level prediction models. *Quarterly Journal of the Royal Meteorological Society*, **102**, 405–418.

Deeter, M. N., D. P. Edwards and J. C. Gille (2007). Retrievals of carbon monoxide profiles from MOPITT observations using lognormal a priori statistics. *Journal of Geophysical Research-Atmospheres*, **112**(D11), 11311–11311. doi: 0.1029/2006JD007999.

Deeter, M. N., L. K. Emmons, D. P. Edwards, J. C. Gille and J. R. Drummond (2004a). Vertical resolution and information content of CO profiles retrieved by MOPITT. *Geophysical Research Letters*, **31**(15), L15112. doi: 0.1029/2004GL020235.

Deeter, M. N., L. K. Emmons, G. L. Francis, D. P. Edwards, J. C. Gille, J. X. Warner, B. Khattatov, D. Ziskin, J. F. Lamarque, S. P. Ho, V. Yudin, J. L. Attie, D. Packman, J. Chen, D. Mao and J. R. Drummond (2003). Operational carbon monoxide retrieval algorithm and selected results for the MOPITT instrument. *Journal of Geophysical Research-Atmospheres*, **108**(D14), 4399. doi: 0.1029/2002JD003186.

Deeter, M. N., L. K. Emmons, G. L. Francis, D. P. Edwards, J. C. Gille, J. X. Warner, B. Khattatov, D. Ziskin, J. F. Lamarque, S. P. Ho, V. Yudin, J. L. Attie, D. Packman, J. Chen, D. Mao, J. R. Drummond, P. Novelli and G. Sachse (2004b). Evaluation of operational radiances for the Measurements of Pollution in the Troposphere (MOPITT) instrument CO thermal band channels. *Journal of Geophysical Research-Atmospheres*, **109**(D3), D03308. doi: 0.1029/2003JD003970.

Dentener, F., S. Kinne, T. Bond, O. Boucher, J. Cofala, S. Generoso, P. Ginoux, S. Gong, J. J. Hoelzemann, A. Ito, L. Marelli, J. E. Penner, J.-P. Putaud, C. Textor, M. Schulz, G. R. van der Werf and J. Wilson (2006). Emissions of primary aerosol and precursor gases in the years 2000 and 1750 prescribed data-sets for AeroCom. *Atmospheric Chemistry and Physics*, **6**(12), 4321–4344.

Derwent, R. G., M. E. Jenkin, S. M. Saunders and M. J. Pilling (1998). Photochemical ozone creation potentials for organic compounds in northwest Europe calculated with a master chemical mechanism. *Atmospheric Environment*, **32**(14-15), 2429 – 2441. doi: 0.1016/S1352-2310(98)00053-3.

Derwent, R. G., D. R. Middleton, R. A. Field, M. E. Goldstone, J. N. Lester and R. Perry (1995). Analysis and interpretation of air quality data from an urban roadside location in Central London over the period from July 1991 to July 1992. *Atmospheric Environment*, **29**(8), 923 – 946. doi: OI: 10.1016/1352-2310(94)00219-B.

Déqué, M., D. P. Rowell, D. Lüthi, F. Giorgi, J. H. Christensen, B. Rockel, D. Jacob, E. Kjellström, M. de Castro and B. van den Hurk (2007). An intercomparison of regional climate simulations for Europe: assessing uncertainties in model projections. *Climatic Change*, **81**, 53–70.

Edwards, D. P., G. Pétron, P. C. Novelli, L. K. Emmons, J. C. Gille and J. R. Drummond (2006). Southern Hemisphere carbon monoxide interannual variability observed by Terra/Measurement of Pollution in the Troposphere (MOPITT). *Journal of Geophysical Research*, **111**, D16303. doi: 0.1029/2006JD007079.

Elkus, B. and K. R. Wilson (1977). Photochemical air pollution: Weekend-weekday differences. *Atmospheric Environment*, **11**(6), 509 – 515. doi: 0.1016/0004-6981(77)90067-1.

Emmons, L. K., M. N. Deeter, J. C. Gille, D. P. Edwards, J. L. Attie, J. Warner, D. Ziskin, G. Francis, B. Khattatov, V. Yudin, J. F. Lamarque, S. P. Ho, D. Mao, J. S. Chen, J. Drummond, P. Novelli, G. Sachse, M. T. Coffey, J. W. Hannigan, C. Gerbig, S. Kawakami, Y. Kondo, N. Takegawa, H. Schlager, J. Baehr and H. Ziereis (2004). Validation of Measurements of Pollution in the Troposphere (MOPITT) CO retrievals with aircraft in situ profiles. *Journal of Geophysical Research-Atmospheres*, **109**(D3), D03309. doi: 0.1029/2003JD004101.

Forkel, R. and R. Knoche (2006). Regional climate change and its impact on photooxidant concentrations in southern Germany: Simulations with a coupled regional climate-chemistry model. *Journal of Geophysical Research-Atmospheres*, **111**(D12), D12302. doi: 0.1029/2005JD006748.

Frei, C. and C. Schär (1998). A precipitation climatology of the Alps from high-resolution rain-gauge observations. *International Journal Of Climatology*, **18**(8), 873–900.

Freitas, E., C. Rozoff, W. Cotton and P. Dias (2007). Interactions of an urban heat island and sea-breeze circulations during winter over the metropolitan area of São Paulo, Brazil. *Boundary-Layer Meteorology*, **122**(1), 43–65.

Freitas, S. R., K. M. Longo and M. O. Andreae (2006). Impact of including the plume rise of vegetation fires in numerical simulations of associated atmospheric pollutants. *Geophysical Research Letters*, **33**(17), L17808. doi: 0.1029/2006GL026608.

Generoso, S., F.-M. Bréon, Y. Balkanski, O. Boucher and M. Schulz (2003). Improving the seasonal cycle and interannual variations of biomass burning aerosol sources. *Atmospheric Chemistry and Physics*, **3**(4), 1211–1222.

Gillani, N. V. and J. E. Pleim (1996). Sub-grid-scale features of anthropogenic emissions of NOx and VOC in the context of regional eulerian models. *Atmospheric Environment*, **30**(12), 2043 – 2059. doi: 0.1016/1352-2310(95)00201-4. A WMA International Specialty Conference on Regional Photochemical Measurements and Modeling.

Giorgi, F. (2006). Regional climate modeling: Status and perspectives. *Journal De Physique IV*, **139**, 101–118. doi: 0.1051/jp4:2006139008.

Giorgi, F. and F. Meleux (2007). Modelling the regional effects of climate change on air quality. *Comptes Rendus Geoscience*, **339**(11-12), 721–733. doi: 0.1016/j.crte.2007.08.006.

Gorman, D., A. Drewry, Y. L. Huang and C. Sames (2003). The clinical toxicology of carbon monoxide. *Toxicology*, **187**(1), 25–38. doi: 0.1016/S0300-483X(03)00005-2.

Guttikunda, S. K., Y. H. Tang, G. R. Carmichael, G. Kurata, L. Pan, D. G. Streets, J. H. Woo, N. Thongboonchoo and A. Fried (2005). Impacts of Asian megacity emissions on regional air quality during spring 2001. *Journal of Geophysical Research*, **110**(D20), D20301. doi: 0.1029/2004JD004921.

Hass, H. (1991). Description of the EURAD Chemistry-Transport-Model Version2. Technical report, Institut für Geophysik und Meteorologie der Universität zu Köln.

Hesstvedt, E., Ö. Hov and I. S. A. Isaksen (1978). Quasi-steady-state approximations in air pollution modeling: Comparison of two numerical schemes for oxidant prediction. *International Journal of Chemical Kinetics*, **10**(9), 971–994.

Hobbs, J., J. Lindesay and H. Bridgman (1998). Climates of the Southern Continents: past present and future. Wiley.

Hoelzemann, J. (2006). Global Wildland Fire Emission Modeling for Atmospheric Chemistry Studies. PhD thesis, IMPRS.

Hoelzemann, J. J., M. G. Schultz, G. P. Brasseur, C. Granier and M. Simon (2004). Global Wildland Fire Emission Model (GWEM): Evaluating the use of global area burnt satellite data. *Journal of Geophysical Research*, **109**, –.

Holton, J. R. (2004). An Introduction to Dynamic Meteorology. Academic Press, 3rd edition.

IPCC (2007). Climate Change 2007: The Physical Science Basis. Contribution of Working Group I to the Fourth Assessment Report of the Intergovernmental Panel on Climate Change. Cambridge University Press, Cambridge, United Kingdom and New York, NY, USA, 996 pp.

Ito, A. and J. E. Penner (2004). Global estimates of biomass burning emissions based on satellite imagery for the year 2000. *Journal of Geophysical Research*, **109**, –.

Jacob, D. (2009). Regional climate models: linking global climate change to local impacts, chapter Climate Modeling, Global Warming and Weather Prediction, pp. 7591–7602. Springer.

Jacob, D., L. Bärring, O. B. Christensen, J. H. Christensen, M. de Castro, M. Déqué, F. Giorgi, S. Hagemann, M. Hirschi, R. Jones, E. Kjellström, G. Lenderink, B. Rockel, E. Sánchez, C. Schär, S. I. Seneviratne, S. Somot, A. van Ulden and B. van den Hurk (2007). An inter-comparison of regional climate models for Europe: model performance in present-day climate. *Climatic Change*, **81**, 31–52.

Jacob, D., B. J. J. M. Van den Hurk, U. Andrae, G. Elgered, C. Fortelius, L. P. Graham, S. D. Jackson, U. Karstens, C. Kopken, R. Lindau, R. Podzun, B. Rockel, F. Rubel, B. H. Sass, R. N. B. Smith and X. Yang (2001). A comprehensive model inter-comparison study investigating the water budget during the

BALTEX-PIDCAP period. *Meteorology and Atmospheric Physics*, **77**(1-4), 19–43.

Labrador, L. J., R. von Kuhlmann and M. G. Lawrence (2005). The effects of lightning-produced NOx and its vertical distribution on atmospheric chemistry: sensitivity simulations with MATCH-MPIC. *Atmospheric Chemistry and Physics*, **5**(7), 1815–1834.

Langmann, B. (2000). Numerical modelling of regional scale transport and photochemistry directly together with meteorological processes. *Atmospheric Environment*, **34**(21), 3585–3598. doi: 0.1016/S1352-2310(00)00114-X.

Langmann, B. and S. E. Bauer (2002). On the importance of reliable background concentrations of ozone for regional scale photochemical modelling. *Journal of Atmospheric Chemistry*, **42**(1), 71–90.

Lathière, J., D. A. Hauglustaine, A. D. Friend, N. De Noblet-Ducoudré, N. Viovy and G. A. Folberth (2006). Impact of climate variability and land use changes on global biogenic volatile organic compound emissions. *Atmospheric Chemistry and Physics*, **6**, 2129–2146.

Lavoué, D., C. Liousse, H. Cachier, B. J. Stocks and J. G. Goldammer (2000). Modeling of carbonaceous particles emitted by boreal and temperate wildfires at northern latitudes. *Journal of Geophysical Research*, **105**, 26871–26890. doi: 0.1029/2000JD900180.

Lawrence, M. G., T. M. Butler, J. Steinkamp, B. R. Gurjar and J. Lelieveld (2007). Regional pollution potentials of megacities and other major population centers. *Atmospheric Chemistry and Physics*, **7**, 3969–3987.

Louis, J. F. (1979). Parametric Model Of Vertical Eddy Fluxes In The Atmosphere. *Boundary-Layer Meteorology*, **17**(2), 187–202.

Luderer, G., J. Trentmann, T. Winterrath, C. Textor, M. Herzog, H. Graf and M. Andreae (2006). Modeling of biomass smoke injection into the lower stratosphere by a large forest fire (Part II): sensitivity studies. *Atmospheric Chemistry and Physics*, **6**(12), 5261–5277.

Madronich, S. and S. Flocke (1999). Handbook of Environmental Chemistry, chapter The role of solar radiation in atmospheric chemistry, pp. 1–26. Springer-Verlag, Heidelberg.

Majewski, D. (1991). The Europa-Modell of the Deutscher Wetterdienst. In *ECMWF*, Vol. 2 of *ECMWF Seminar on numerical methods in atmospheric models*, pp. 147–191.

Marcilio, I. and N. Gouveia (2007). Quantifying the impact of air pollution on the urban population of Brazil. *Cadernos de Saúde Pública*, **23, suppl.4**, 529–536. doi: 0.1590/S0102-311X2007001600013.

Marengo, J. A. and S. Hastenrath (1993). Case-Studies Of Extreme Climatic Events In The Amazon Basin. *Journal Of Climate*, **6**(4), 617–627.

Marmer, E. and B. Langmann (2005). Impact of ship emissions on the Mediterranean summertime pollution and climate: A regional model study. *Atmospheric Environment*, **39**(26), 4659–4669.

Mellor, G. L. and T. Yamada (1974). Hierarchy Of Turbulence Closure Models For Planetary Boundary-Layers. *Journal of the Atmospheric Sciences*, **31**(7), 1791–1806.

Messerli, B., M. Grosjean and M. Vuille (1997). Water Availability, Protected Areas, and Natural Resources in the Andean Desert Altiplano. *Mountain Research and Development*, **17**(3), 229–238.

Middleton, P., W. R. Stockwell and W. P. Carter (1990). Aggregation and analysis of volatile organic compound emissions for regional modeling. *Atmospheric Environment*, **24**(5), 1107–1133.

Milford, J. B., D. Gao, S. Sillman, P. Blossey and A. G. Russell (1994). Total reactive nitrogen (NOy) as an indicator of the sensitivity of ozone to reductions in hydrocarbon and NOx emissions. *Journal of Geophysical Research*, **99**, 3533–3542. doi: 0.1029/93JD03224.

Mitchell, T. D. and P. D. Jones (2005). An improved method of constructing a database of monthly climate observations and associated high-resolution grids. *International Journal of Climatology*, **25**(6), 693–712.

Nordeng, T. E. (1994). Extended versions of the convective parametrization scheme at ECMWF and their impact on the mean and transient activity of the model in the tropics. Technical Momorandum 206, ECMWF Research Department, European Centre for Medium Range Weather Forecasts, Reading, UK.

Novelli, P. C., K. A. Masarie and P. M. Lang (1998). Distributions and recent changes of carbon monoxide in the lower troposphere. *Journal of Geophysical Research-Atmospheres*, **103**(D15), 19015–19033.

Olszyna, K. J., E. M. Bailey, R. Simonaitis and J. F. Meagher (1994). O3 and NOy relationships at a rural site. *Journal of Geophysical Research*, **99**, 14557–14563. doi: 0.1029/94JD00739.

Pal, J. S., F. Giorgi, X. Q. Bi, N. Elguindi, F. Solmon, X. J. Gao, S. A. Rauscher, R. Francisco, A. Zakey, J. Winter, M. Ashfaq, F. S. Syed, J. L. Bell, N. S. Diffenbaugh, J. Karmacharya, A. Konare, D. Martinez, R. P. da Rocha, L. C. Sloan and A. L. Steiner (2007). Regional climate modeling for the developing world - The ICTP RegCM3 and RegCNET. *Bulletin of the American Meteorological Society*, **88**(9), 1395–+.

Pan, L. W., J. C. Gille, D. P. Edwards, P. L. Bailey and C. D. Rodgers (1998). Retrieval of tropospheric carbon monoxide for the MOPITT experiment. *Journal of Geophysical Research-Atmospheres*, **103**(D24), 32277–32290.

Pleim, J. E., J. S. Chang and K. S. Zhang (1991). A nested grid mesoscale atmospheric chemistry model. *Journal of Geophysical Research-Atmospheres*, **96**(D2), 3065–3084.

Poppe, D., R. Koppmann and J. Rudolph (1998). Ozone formation in biomass burning plumes: Influence of atmospheric dilution. *Geophysical Research Letters*, **25**(20), 3823–3826.

Prins, E., J. Feltz, W. Menzel and D. Ward (1998). An overview of GOES-8 diurnal fire and smoke results for SCAR-B and 1995 fire season in South America. *Journal Of Geophysical Research*, **103**(D24), 31821–31835.

Pétron, G., C. Granier, B. Khattatov, V. Yudin, J.-F. Lamarque, L. Emmons, J. Gille and D. P. Edwards (2004). Monthly CO surface sources inventory based on the 2000–2001 MOPITT satellite data. *Geophysical Research Letters*, **31**, –.

Rechid, D. and D. Jacob (2006). Influence of monthly varying vegetation on the simulated climate in Europe. *Meteorologische Zeitschrift*, **15**(1), 99–116. doi: 0.1127/0941-2948/2006/0091.

Reich, S., J. Magallanes, L. Dawidowski, D. Gómez, N. Grošelj and J. Zupan (2006). An Analysis of Secondary Pollutants in Buenos Aires City. *Environmental Monitoring and Assessment*, **119**(1), 441–457.

Rodgers, C. D. (2000). Inverse methods for atmospheric sounding : theory and practice. World Scientific Publishing.

Roeckner, E., K. Arpe, L. Bengtsson, M. Christoph, M. Claussen, L. Dümenil, M. Esch, M. Giorgetta, U. Schlese and U. Schulzweida (1996). The atmospheric general circulation model ECHAM-4: Model description and simulation of present-day climate. Report 218, Max Planck Institute for Meteorology, Hamburg.

Schultz, M., S. Rast, M. van het Bolscher, T. Pulles, R. Brand, J. Pereira, A. Spessa, S. Dalsøren, T. van Nojie and S. Szopa (2008a). Emission data sets and methodologies for estimating emissions. Deliverable D1-6, MPI for Meteorology, Hamburg. Work Package 1,.

Schultz, M. G., A. Heil, J. J. Hoelzemann, A. Spessa, K. Thonicke, J. G. Goldammer, A. C. Held, J. M. C. Pereira and M. van het Bolscher (2008b). Global wildland fire emissions from 1960 to 2000. *Global Biogeochemical Cycles*, **22**, GB2002. doi: 0.1029/2007GB003031.

Seifert, M., J. Ström, R. Krejci, A. Minikin, A. Petzold, J.-F. Gayet, H. Schlager, H. Ziereis, U. Schumann and J. Ovarlez (2004). Aerosol-cirrus interactions: a number based phenomenon at all? *Atmospheric Chemistry and Physics*, **4**(2), 293–305.

Seinfeld, J. H. and S. N. Pandis (2006). Atmospheric Chemistry and Physics. Wiley.

Semmler, T. (2002). Der Wasser- und Energiehaushalt der arktischen Atmosphäre. PhD thesis, MPI-MET.

Sillman, S. (1995). The use of NOy, H2O2, and HNO3 as indicators for ozone-NOx-hydrocarbon sensitivity in urban locations. *Journal of Geophysical Research*, **100**, 14175—-14188. doi: 0.1029/94JD02953.

Sillman, S. (1999). The relation between ozone, NOx and hydrocarbons in urban and polluted rural environments. *Atmospheric Environment*, **33**(12), 1821–1845. doi: 0.1016/S1352-2310(98)00345-8.

Silvestri, G., C. Vera, D. Jacob, S. Pfeifer and C. Teichmann (2009). A high-resolution 43-year atmospheric hindcast for South America generated with the MPI regional model. *Climate Dynamics*, **32**(5), 693–709. doi: 0.1007/s00382-008-0423-5.

Simmons, A. and D. Burridge (1981). An Energy and Angular-Momentum Conserving Vertical Finite-Difference Scheme and Hybrid Vertical Coordinates. *Monthly Weather Review*, **109**(4), 758–766.

Sistla, G., N. Zhou, W. Hao, J. Ku, S. Rao, R. Bornstein, F. Freedman and P. Thunis (1996). Effects of uncertainties in meteorological inputs on urban airshed model predictions and ozone control strategies. *ATMOSPHERIC ENVIRONMENT*, **30**(12), 2011–2025. doi: 0.1016/1352-2310(95)00268-5. International Specialty Conference on Regional Photochemical Measurement and Modeling Studies, SAN DIEGO, CA, NOV 08-12, 1993.

Smolarkiewicz, P. K. (1983). A Simple Positive Definite Advection Scheme With Small Implicit Diffusion. *Monthly Weather Review*, **111**(3), 479–486.

Smolarkiewicz, P. K. (1984). A Fully Multidimensional Positive Definite Advection Transport Algorithm With Small Implicit Diffusion. *Journal of Computational Physics*, **54**(2), 325–362.

Stamnes, K., S.-C. Tsay, W. Wiscombe and K. Jayaweera (1988). Numerically stable algorithm for discrete-ordinate-method radiative transfer in multiple scattering and emitting layered media. *Applied Optics*, **27**(12), 2502–2509. doi: 0.1364/AO.27.002502.

Stockwell, D. Z., C. Giannakopoulos, P. H. Plantevin, G. D. Carver, M. P. Chipperfield, K. S. Law, J. A. Pyle, D. E. Shallcross and K. Y. Wang (1999). Modelling NOx from lightning and its impact on global chemical fields. *Atmospheric Environment*, **33**(27), 4477 – 4493. doi: 0.1016/S1352-2310(99)00190-9.

Stockwell, W. R., P. Middleton, J. S. Chang and X. Y. Tang (1990). The 2nd Generation Regional Acid Deposition Model Chemical Mechanism For Regional Air-Quality Modeling. *Journal of Geophysical Research-Atmospheres*, **95**(D10), 16343–16367.

Ström, J. (2002). INCA. Final report. Technical report, Stockholm University.

Ström, J., M. Seifert, B. Kärcher, J. Ovarlez, A. Minikin, J.-F. Gayet, R. Krejci, A. Petzold, F. Auriol, W. Haag, R. Busen, U. Schumann and H. C. Hansson (2003). Cirrus cloud occurrence as function of ambient relative humidity: a comparison of observations obtained during the INCA experiment. *Atmospheric Chemistry and Physics*, **3**(5), 1807–1816.

Suprit, K. and D. Shankar (2008). Resolving orographic rainfall on the Indian west coast. *International Journal of Climatology*, **28**(5), 643–657. doi: 0.1002/joc.1566.

Tie, X. X., S. Madronich, S. Walters, R. Y. Zhang, P. Rasch and W. Collins (2003). Effect of clouds on photolysis and oxidants in the troposphere. *Journal of Geophysical Research-Atmospheres*, **108**(D20), 4642. doi: 0.1029/2003JD003659.

Tiedtke, M. (1989). A comprehensive mass flux scheme for cumulus parameterization in large-scale models. *Monthly Weather Review*, **117**(8), 1779–1800.

Trainer, M., D. D. Parrish, M. P. Buhr, R. B. Norton, F. C. Fehsenfeld, K. G. Anlauf, J. W. Bottenheim, Y. Z. Tang, H. A. Wiebe, J. M. Roberts, R. L. Tanner, L. Newman, V. C. Bowersox, J. F. Meagher, K. J. Olszyna, M. O. Rodgers, T. Wang, H. Berresheim, K. L. Demerjian and U. K. Roychowdhury (1993). Correlation Of Ozone With Noy In Photochemically Aged Air. *Journal of Geophysical Research*, **98**, 2917—-2925. doi: 0.1029/92JD01910.

UN (2008). World Urbanization Prospects: The 2007 Revision. United Nations Department of Economic and Social Affairs/Population Division.

Uppala, S. M., P. W. Kallberg, A. J. Simmons, U. Andrae, V. D. Bechtold, M. Fiorino, J. K. Gibson, J. Haseler, A. Hernandez, G. A. Kelly, X. Li, K. Onogi, S. Saarinen, N. Sokka, R. P. Allan, E. Andersson, K. Arpe, M. A. Balmaseda, A. C. M. Beljaars, L. Van De Berg, J. Bidlot, N. Bormann, S. Caires, F. Chevallier, A. Dethof, M. Dragosavac, M. Fisher, M. Fuentes, S. Hagemann, E. Holm, B. J. Hoskins, L. Isaksen, P. A. E. M. Janssen, R. Jenne, A. P. McNally, J. F. Mahfouf, J. J. Morcrette, N. A. Rayner, R. W. Saunders, P. Simon, A. Sterl, K. E. Trenberth, A. Untch, D. Vasiljevic, P. Viterbo and J. Woollen (2005). The ERA-40 re-analysis. *Quarterly Journal of the Royal Meteorological Society*, **131**(612), 2961–3012.

van der Werf, G. R., J. T. Randerson, G. J. Collatz and L. Giglio (2003). Carbon emissions from fires in tropical and subtropical ecosystems. *Global Change Biology*, **9**(4), 547–562.

Vera, C., J. Baez, M. Douglas, C. B. Emmanuel, J. Marengo, J. Meitin, M. Nicolini, J. Nogues-Paegle, J. Paegle, O. Penalba, P. Salio, C. Saulo, M. A. Silva Dias, P. Silva Dias and E. Zipser (2006). The South American Low-Level Jet Experiment. *Bulletin of the American Meteorological Society*, **87**(1), 63 – 77.

Virji, H. (1981). A Preliminary-Study Of Summertime Tropospheric Circulation Patterns Over South-America Estimated From Cloud Winds. *Monthly Weather Review*, **109**(3), 599–610.

Voulgarakis, A., O. Wild, N. H. Savage, G. D. Carver and J. A. Pyle (2009). Clouds, photolysis and regional tropospheric ozone budgets. *Atmospheric Chemistry and Physics Discussions*, **9**(3), 13889–13916.

Walcek, C. J. and G. R. Taylor (1986). A Theoretical Method For Computing Vertical Distributions Of Acidity And Sulfate Production Within Cumulus Clouds. *Journal of the Atmospheric Sciences*, **43**(4), 339–355.

Warner, J., M. M. Comer, C. D. Barnet, W. W. McMillan, W. Wolf and E. Maddy (2007). A comparison of satellite tropospheric carbon monoxide measurements from AIRS and MOPITT during INTEX-A. *Journal of Geophysical Research-Atmospheres*, **112**(D12), S1217–S1217. doi: 0.1029/2006JD007925.

Warner, J. X., J. C. Gille, D. P. Edwards, D. C. Ziskin, M. W. Smith, P. L. Bailey and L. Rokke (2001). Cloud detection and clearing for the Earth Observing System Terra satellite Measurements of Pollution in the Troposphere (MOPITT) experiment. *Applied Optics*, **40**(8), 1269–1284.

Wesely, M. (1989). Parameterization of surface resistances to gaseous dry deposition in regional-scale numerical models. *Atmospheric Environment*, **23**(6), 1293–1304.

WHO (2000). Air quality guidelines for Europe, 2nd edition. No. 91 in *WHO regional publications. European series*. WHO Regional Office for Europe.

WHO (2006). WHO Air quality guidelines for particulate matter, ozone, nitrogen dioxide and sulfur dioxide, Global update 2005 Summary of risk assessment. WHO.

A Chemical Species

Trace gas species of the RADM2 chemical mechanism used in this work. Molecular weight represents a representative average if the tracer represents a lumped species.

Species name	Chemical formula	Repr.	Molec. weight
inorganics			
Nitrogen dioxide	NO_2	NO2	46
Nitric oxide	NO	NO	30
Nitrous acid	NHO_2	HONO	47
Nitrogen trioxide	NO_3	NO3	62
Nitrogen pentoxide	N_2O_5	N2O5	108
Nitric acid	HNO_3	HNO3	63
Pernitric acid	HNO_4	HNO4	79
Ozone	O_3	O3	48
Hydrogen Peroxide	H_2O_2	H2O2	34
Sulfur dioxide	SO_2	SO2	64
Sulfuric acid	H_2SO_4	SULF	98
Carbon monoxide	CO	CO	28
Carbon dioxide	CO_2	(prod. only)	44
Ground state oxygen	O^3P	O3P	16
Excited oxygen	O^1D	O1D	16
Hydroxy radical	OH	HO	17
Hydroperoxy radical	HO_2	HO2	33
Ammonia	NH_3	NH3	17
Oxygen	O_2	O2	32
Nitrogen	N_2	N2	28
Water	H_2O	H2O	18
Alkanes			
Methane	CH_4	CH4	16
Ethane	C_2H_6	ETH	30

C3 to C5 Alkanes	C_3H_8,C_4H_{10}	HC3	44
C6 to C8 Alkanes	C_7H_{16}	HC5	72
higher Alkanes	$C_{10}H_{22}$	HC8	114
Alkenes			
Ethene	C_2H_4	OL2	28
terminal alkenes	C_3H_6	OLT	42
internal alkenes	C_4H_8	OLI	56
Isoprene	C_5H_8	ISO	68
Aromatics			
Toluene	$CH_3C_6H_5$	TOL	92
Cresol	$HOC_6H_4-CH_3$	CSL	108
Xylene	$(CH_3)_2C_6H_4$	XYL	106
Carbonyls			
Formaldehyde	CH_2O	HCHO	30
Acetaldehyde	$R-CHO$	ALD	44
Ketones	CH_3COCH_3, $CH_3COC_2H_5$	KET	72
Glyoxal	$(CHO)_2$	GLY	58
Methylglyoxal	CH_3COCHO	MGLY	72
other Dicarbonyls	$R-(CHO)_2$	DCB	87
Organic Nitrogen			
Peroxyacetylnitrate	$CH_3CO_3NO_2$	PAN	121
TPAN	$CHOCH=CHCO_3NO_2$	TPAN	147
other organic nitrate	$R-ONO_2$	ONIT	119
Organic Peroxides			
Methyl hydrogen per.	CH_3OOH	OP1	48
other organic per.	$R-OOH$	OP2	62
Peroxyacetic acid	CH_3COOOH	PAA	76
Organic acids			
Formic acid	$HCOOH$	ORA1	46
Acetic acid	CH_3COOH	ORA2	60

Organic intermediates			
Acetyl peroxyl rad.	$CH_3{-}CO_3$	ACO3	75
Methyl peroxyl rad.	CH_3O_2	MO2	47
Peroxy rad. from ETH	$C_2H_5O_2$	ETHP	61
Peroxy rad. from HC3	$R{-}O_2$	HC3P	75
Peroxy rad. from HC5	$R{-}O_2$	HC5P	103
Peroxy rad. from HC8	$R{-}O_2$	HC8P	145
Peroxy rad. from OL2	$HOC_2H_4O_2$	OL2P	77
Peroxy rad. from OLT	$HOC_3H_6O_2$	OLTP	91
Peroxy rad. from OLI	$HOC_4H_8O_2$	OLIP	105
Peroxy rad. from TOL	$HOCH_3C_6H_5O_2$	TOLP	141
Peroxy rad. from XYL	$HO(CH_3)_2C_6H_4O_2$	XYLP	155
Peroxy rad. from KET	$R{-}CO{-}R{-}O_2$	KETP	103
	$H(CO)CH{=}CHCO_3$	TCO3	115
NO_3-alkene adduct		OLN	136
additional organic nitrate		XNO2	–
NO-to-NO_2 conversion species		XO2	–

B Chemical Reactions

Photochemical and thermal reactions as they are implemented in REMO$_{\texttt{chem}}$ following Stockwell et al. (1990). Aqueous equilibria after Walcek and Taylor (1986).

Photolysis reactions		
NO2 + $h\nu$	$\longrightarrow$	O3P + NO
O3 + $h\nu$	$\longrightarrow$	O1D + O2
O3 + $h\nu$	$\longrightarrow$	O3P + O2
HONO + $h\nu$	$\longrightarrow$	OH + NO
HNO3 + $h\nu$	$\longrightarrow$	OH + NO2
HNO4 + $h\nu$	$\longrightarrow$	HO2 + NO2
NO3 + $h\nu$	$\longrightarrow$	NO + O2
NO3 + $h\nu$	$\longrightarrow$	NO2 + O3P
H2O2 + $h\nu$	$\longrightarrow$	OH + OH
HCHO + $h\nu$	$\longrightarrow$	H2 + CO
HCHO + $h\nu$	$\longrightarrow$	HO2 + HO2 + CO
ALD + $h\nu$	$\longrightarrow$	MO2 + HO2 + CO
OP1 + $h\nu$	$\longrightarrow$	HCHO + HO2 + OH
OP2 + $h\nu$	$\longrightarrow$	ALD + HO2 + OH
PAA + $h\nu$	$\longrightarrow$	MO2 + CO2 + OH
KET + $h\nu$	$\longrightarrow$	ACO3 + ETHP
GLY + $h\nu$	$\longrightarrow$	0.13 HCHO + 1.87 CO
GLY + $h\nu$	$\longrightarrow$	0.45 HCHO + 1.55 CO + 0.80 HO2
MGLY + $h\nu$	$\longrightarrow$	ACO3 + HO2 + CO
DCB + $h\nu$	$\longrightarrow$	0.98 HO2 + 0.02 ACO3 + TCO3
ONIT + $h\nu$	$\longrightarrow$	0.20 ALD + 0.80 KET + HO2 + NO2

Thermal reactions		
O3P + O2	⟶	O3
O3P + NO2	⟶	NO + O2
O1D + N2	⟶	O3P + O2
O1D + O2	⟶	O3P + O2
O1D + H2O	⟶	OH + OH
O3 + NO	⟶	NO2 + O2
O3 + OH	⟶	HO2 + O2
O3 + HO2	⟶	OH + 2.00 O2
HO2 + NO	⟶	NO2 + OH
HO2 + NO2	⟶	HNO4
HNO4	⟶	HO2 + NO2
HO2 + HO2	⟶	H2O2
HO2 + HO2 + H2O	⟶	H2O2
H2O2 + OH	⟶	HO2 + H2O
NO + OH	⟶	HONO
NO + NO + O2	⟶	NO2 + NO2
O3 + NO2	⟶	NO3
NO3 + NO	⟶	NO2 + NO2
NO3 + NO2	⟶	NO + NO2 + O2
NO3 + HO2	⟶	HNO3 + O2
NO3 + NO2	⟶	N2O5
N2O5	⟶	NO2 + NO3
N2O5 + H2O	⟶	2.00 HNO3
OH + NO2	⟶	HNO3
OH + HNO3	⟶	NO3 + H2O
OH + HNO4	⟶	NO2 + H2O + O2
OH + HO2	⟶	H2O + O2
OH + SO2	⟶	SULF + HO2
CO + OH	⟶	HO2 + CO2
CH4 + OH	⟶	MO2 + H2O
ETH + OH	⟶	ETHP + H2O
HC3 + OH	⟶	0.83 HC3P + 0.17 HO2 + 0.09 HCHO + 0.075 ALD + 0.025 KET + H2O
HC5 + OH	⟶	HC5P + 0.25 XO2 + H20
HC8 + OH	⟶	HC8P + 0.75 XO2 + H20

OL2 + OH ⟶ OL2P
OLT + OH ⟶ OLTP
OLI + OH ⟶ OLIP
TOL + OH ⟶ 0.75 TOLP + 0.25 CSL + 0.25 HO2
XYL + OH ⟶ 0.83 XYLP + 0.17 CSL + 0.17 HO2
CLS + OH ⟶ 0.10 HO2 + 0.90 XO2 + 0.90 TCO3 - 0.90 OH
HCHO + OH ⟶ HO2 + CO + H2O
ALD + OH ⟶ ACO3 + H2O
KET + OH ⟶ KETP + H2O
GLY + OH ⟶ HO2 + 2.00 CO + H2O
MGLY + OH ⟶ ACO3 + CO + H2O
DCB + OH ⟶ TCO3 + H2O
OP1 + OH ⟶ 0.50 MO2 + 0.50 HCHO + 0.50 OH
OP2 + OH ⟶ 0.50 HC3P + 0.50 ALD + 0.50 OH
PAA + OH ⟶ ACO3 + H2O
PAN + OH ⟶ HCHO + NO3 + XO2
ONIT + OH ⟶ HC3P + NO2
ISO + OH ⟶ OLTP
ACO3 + NO2 ⟶ PAN
PAN ⟶ ACO3 + NO2
TCO3 + NO2 ⟶ TPAN
TPAN ⟶ TCO3 + NO2
MO2 + NO ⟶ HCHO + HO2 + NO2
HC3P + NO ⟶ 0.75 ALD + 0.25 KET + 0.09 HCHO
+ 0.36 ONIT + 0.96 NO2 + 0.96 HO2
HC5P + NO ⟶ 0.38 ALD + 0.69 KET + 0.08 ONIT
+ 0.92 NO2 + 0.92 HO2
HC8P + NO ⟶ 0.35 ALD + 1.06 KET + 0.04 HCHO
+ 0.24 ONIT + 0.76 NO2 + 0.76 HO2
OL2P + NO ⟶ 1.60 HCHO + HO2 + NO2
+ 0.20 ALD
OLTP + NO ⟶ ALD + HCHO + HO2 + NO2
OLIP + NO ⟶ HO2 + 1.45 ALD + 0.28 HCHO
+ 0.10 KET + NO2
ACO3 + NO ⟶ NO2 + NO2

TCO3 + NO ⟶ NO2 + 0.92 HO2 + 0.89 GLY + 0.11 MGLY + 0.05 ACO3 + 0.95 CO + 2.00 XO2
TOLP + NO ⟶ NO2 + HO2 + 0.17 MGLY + 0.16 GLY + 0.70 DCB
XYLP + NO ⟶ NO2 + NO2 + 0.45 MGLY + 0.806 DCB
ETHP + NO ⟶ ALD + HO2 + NO2
KETP + NO ⟶ MGLY + NO2 + HO2
OLN + NO ⟶ HCHO + ALD + 2.00 NO2
HCHO + NO3 ⟶ HO2 + HNO3 + CO
ALD + NO3 ⟶ ACO3 + HNO3
GLY + NO3 ⟶ HNO3 + HO2 + 2.00 CO
MGLY + NO3 ⟶ HNO3 + ACO3 + CO
DCB + NO3 ⟶ HNO3 + TCO3
CSL + NO3 ⟶ HNO3 + XNO2 + 0.50 CSL
OL2 + NO3 ⟶ OLN
OLT + NO3 ⟶ OLN
OLI + NO3 ⟶ OLN
ISO + NO3 ⟶ OLN
OL2 + O3 ⟶ HCHO + 0.42 CO + 0.40 ORA1 + 0.12 HO2
OLT + O3 ⟶ 0.53 HCHO + 0.50 ALD + 0.33 CO + 0.20 ORA1 + 0.20 ORA2 + 0.23 HO2 + 0.22 MO2 + 0.10 OH + 0.06 CH4
OLI + O3 ⟶ 0.18 HCHO + 0.72 ALD + 0.10 KET + 0.23 CO + 0.06 ORA1 + 0.29 ORA2 + 0.09 CH4 + 0.26 HO2 + 0.31 MO2 + 0.14 OH
ISO + O3 ⟶ 0.53 HCHO + 0.50 ALD + 0.33 CO + 0.20 ORA1 + 0.20 ORA2 + 0.23 HO2 + 0.22 MO2 + 0.10 OH
HO2 + MO2 ⟶ OP1
HO2 + ETHP ⟶ OP2
HO2 + HC3P ⟶ OP2
HO2 + HC5P ⟶ OP2
HO2 + HC8P ⟶ OP2

HO2 + OL2P ⟶ OP2
HO2 + OLTP ⟶ OP2
HO2 + OLIP ⟶ OP2
HO2 + KETP ⟶ OP2
HO2 + ACO3 ⟶ PAA
HO2 + TOLP ⟶ OP2
HO2 + XYLP ⟶ OP2
HO2 + TCO3 ⟶ OP2
HO2 + OLN ⟶ ONIT
MO2 + MO2 ⟶ 1.50 HCHO + HO2
MO2 + ETHP ⟶ 0.75 HCHO + HO2 + 0.75 ALD
MO2 + HC3P ⟶ 0.84 HCHO + HO2 + 0.77 ALD
0.26 KET
MO2 + HC5P ⟶ 0.77 HCHO + HO2 + 0.41 ALD
0.75 KET
MO2 + HC8P ⟶ 0.80 HCHO + HO2 + 0.46 ALD
1.39 KET
MO2 + OL2P ⟶ 1.55 HCHO + HO2 + 0.35 ALD
MO2 + OLTP ⟶ 1.25 HCHO + HO2 + 0.75 ALD
MO2 + OLIP ⟶ 0.89 HCHO + HO2 + 0.73 ALD
+ 0.55 KET
MO2 + KETP ⟶ 0.75 HCHO + HO2 + 0.75 MGLY
MO2 + ACO3 ⟶ HCHO + 0.50 HO2 + 0.50 MO2
+ 0.50 ORA2
MO2 + TOLP ⟶ HCHO + 2.00 HO2 + 0.17 MGLY
+ 0.16 GLY + 0.70 DCB
MO2 + TCO3 ⟶ HCHO + 2.00 HO2 + 0.45 MGLY
+ 0.806 DCB
MO2 + TCO3 ⟶ 0.50 HCHO + 0.50 ORA2 + O.445 GLY
+ 0.055 MGLY + 0.025 ACO3 + 0.475 CO
+ 0.46 HO2 + XO2
MO2 + OLN ⟶ 1.75 HCHO + 0.50 HO2 + ALD
+ NO2
ETHP + ACO3 ⟶ ALD + 0.50 HO2 + 0.50 MO2
+ 0.50 ORA2
HC3P + ACO3 ⟶ 0.77 ALD + 0.26 KET + 0.50 HO2
+ 0.50 ORA2 + 0.50 MO2

HC5P + ACO3 $\longrightarrow$ 0.41 ALD + 0.75 KET + 0.50 HO2 + 0.50 ORA2 + 0.50 MO2
HC8P + ACO3 $\longrightarrow$ 0.46 ALD + 1.39 KET + 0.50 HO2 + 0.50 ORA2 + 0.50 MO2
OL2P + ACO3 $\longrightarrow$ 0.80 HCHO + 0.60 ALD + 0.50 HO2 + 0.50 ORA2 + 0.50 MO2
OLTP + ACO3 $\longrightarrow$ ALD + 0.50 HCHO + 0.50 HO2 + 0.50 ORA2 + 0.50 MO2
OLIP + ACO3 $\longrightarrow$ 0.725 ALD + 0.55 KET + 0.14 HCHO + 0.50 HO2 + 0.50 ORA2 + 0.50 MO2
KETP + ACO3 $\longrightarrow$ MGLY + 0.50 HO2 + 0.50 ORA2 + 0.50 MO2
ACO3 + ACO3 $\longrightarrow$ 2.00 MO2
ACO3 + TOLP $\longrightarrow$ 0.17 MGLY + 0.16 GLY + 0.70 DCB + HO2 + MO2
ACO3 + XYLP $\longrightarrow$ MO2 + 0.45 MGLY + 0.806 DCB + HO2
ACO3 + TCO3 $\longrightarrow$ MO2 + 0.92 HO2 + 0.89 GLY + 0.11 MGLY + 0.05 ACO3 + 0.95 CO + 2.00 XO2
ACO3 + OLN $\longrightarrow$ HCHO + ALD + 0.50 ORA2 + NO2 + 0.50 MO2
OLN + OLN $\longrightarrow$ 2.00 HCHO + 2.00 ALD + 2.00 NO2
XO2 + HO2 $\longrightarrow$ OP2
XO2 + MO2 $\longrightarrow$ HCHO + HO2
XO2 + ACO3 $\longrightarrow$ MO2
XO2 + XO2 $\longrightarrow$
XO2 + NO $\longrightarrow$ NO2
XNO2 + NO2 $\longrightarrow$ ONIT
XNO2 + HO2 $\longrightarrow$ OP2
XNO2 + MO2 $\longrightarrow$ HCHO + HO2
XNO2 + ACO3 $\longrightarrow$ MO2
XNO2 + XNO2 $\longrightarrow$

aqueous equilibria		
$SO_{2\,(g)}$	$\rightleftharpoons$	$SO_2 \cdot H_2O$
$SO_2 \cdot H_2O$	$\rightleftharpoons$	$HSO_3^- + H^+$
HSO_3^-	$\rightleftharpoons$	$SO_3^{2-} + H^+$
HSO_4^-	$\rightleftharpoons$	$SO_4^{2-} + H^+$
$HNO_{3\,(g)}$	$\rightleftharpoons$	$NO_3^- + H^+$
$NH_{3\,(g)}$	$\rightleftharpoons$	NH_4OH
NH_4OH	$\rightleftharpoons$	$NH_4^+ + OH^-$
$HCOOH_{(g)}$	$\rightleftharpoons$	$HCOOH_{(aq)}$
$HCOOH_{(aq)}$	$\rightleftharpoons$	$HCOO^- + H^+$
$CO_{2\,(g)}$	$\rightleftharpoons$	$CO_2 \cdot H_2O$
$CO_2 \cdot H_2O$	$\rightleftharpoons$	$HCO_3^- + H^+$
HCO_3^-	$\rightleftharpoons$	$CO_3^{2-} + H^+$
H_2O	$\rightleftharpoons$	$OH^- + H^+$
$O_{3\,(g)}$	$\rightleftharpoons$	$O_{3\,(aq)}$
$H_2O_{2\,(g)}$	$\rightleftharpoons$	$H_2O_{2\,(aq)}$
$CH_3(CO)OOH_{(g)}$	$\rightleftharpoons$	$CH_3(CO)OOH_{(aq)}$
$CH_3OOH_{(g)}$	$\rightleftharpoons$	$CH_3OOH_{(aq)}$

C Remo Model Runs

REMO model runs used in this study are listed below together with their general characteristics and simulation time period.

Name	Description	Period
$\mathrm{R}_{\mathrm{ERA\,40}}$	REMO simulation without chemistry and tracer transport using ERA-40 data as meteorological boundary conditions	1959-2000
$\mathrm{R}_{\mathrm{reference}}$	REMO simulation including chemistry and tracer transport	January 2000 to November 2000
$\mathrm{R}_{\mathrm{decreased\,MCs}}$	Similar to $\mathrm{R}_{\mathrm{reference}}$, but with reduced megacity emissions (reduced by 90%)	January 2000 to November 2000
$\mathrm{R}_{\mathrm{no\,fires}}$	Similar to $\mathrm{R}_{\mathrm{reference}}$, but without fire emissions	January 2000 to November 2000
$\mathrm{R}_{\mathrm{increased\,MCs}}$	Similar to $\mathrm{R}_{\mathrm{reference}}$, but with increased emissions from megacities according to their projected population increase from 2000 to 2025	January 2000 to November 2000

D List of Abbreviations and Acronyms

CRU	Climatic Research Unit
CTM	Chemistry Transport Model
DLR	Deutsches Zentrum für Luft- und Raumfahrt
DWD	Deutscher Wetterdienst (German weather service)
EOS	Earth Observing System
GOME	Global Ozone Monitoring Experiment
INCA	Interhemispheric Differences in Cirrus Properties from Anthropogenic Emissions
ITCZ	InterTropical Convergence Zone
MOPITT	Measurements Of Pollution In The Troposphere
MOZART	Model for Ozone and Related Chemical Tracers
NASA	National Aeronautics and Space Administration
NCEP	National Centers for Environmental Prediction
ORCHODEE	Organizing Carbon and Hydrology in Dynamic Ecosystems
QSSA	Quasi-Steady-State Approximation
RADM2	second generation Regional Acid Deposition Model
RCM	Regional Climate Model
REMO	REgional MOdel
RETRO	REanalysis of the TROpospheric chemical composition over the past 40 years
TUV radiation model	Tropospheric Ultraviolet and Visible radiation model
VOCs	Volatile Organic Compounds
WHO	World Health Organization

Acknowledgements

A lot of people supported me during the period of my PhD. In this chapter, I would like to mention some of them.

I would like to express my sincere thanks to my supervisor Dr. Daniela Jacob for her scientific guidance and support during the period of my PhD. I am very grateful to my doctoral advisor Prof. Dr. Guy Brasseur, who introduced me to the interesting topic of atmospheric chemistry and air pollution. I would also like to thank the other members of my advisory panel, Prof. Dr. Hartmut Graßl and Dr. Johann Feichter, for their support and suggestions.

Working in the regional climate modelling group was a great pleasure for me. I would like to thank Susanne Pfeifer, Sebastian Rast and Rita Seiffert for reading parts of my thesis and giving suggestions and comments. The moral support and humor of Kevin Sieck and the former group members Sven Kotlarski and Holger Göttel helped me a lot when scientific inspiration seemed to be lost.

I especially thank Angelika Heil for her scientific advise and the fruitful discussions.

I really appreciated being a member of the International Max Planck Research School on Earth System Modelling (IMPRS-ESM), who also financed most parts of this work. Especially the advise of Antje Weitz and Cornelia Kampmann helped a lot during the whole period of my PhD.

Finally, I would like to thank my family and Ria for their encouragement and patience.

Die gesamten Veröffentlichungen in der Publikationsreihe des MPI-M
„Berichte zur Erdsystemforschung“,
„Reports on Earth System Science“,
ISSN 1614-1199

sind über die Internetseiten des Max-Planck-Instituts für Meteorologie erhältlich:

http://www.mpimet.mpg.de/wissenschaft/publikationen.html

ISSN 1614-1199